

GEOID DETERMINATION IN THE COASTAL AREAS OF THE GULF OF MEXICO

A Dissertation

by

HONGZHI SONG

BS, Texas A&M University-Corpus Christi, 2009

Submitted in Partial Fulfillment of the Requirements for the Degree of

DOCTOR OF PHILOSOPHY

in

COASTAL MARINE SYSTEMS SCIENCE

Texas A&M University-Corpus Christi
Corpus Christi, Texas

August 2013

© Hongzhi Song

All Rights Reserved

August 2013

GEOID DETERMINATION IN THE COASTAL AREAS OF THE GULF OF MEXICO

A Dissertation

by

HONGZHI SONG

This dissertation meets the standards for scope and quality of Texas A&M University-Corpus Christi and is hereby approved.

Alexey Sadovski, PhD
Chair

Gary Jeffress, PhD
Committee Member

Paul Montagna, PhD
Committee Member

Dru Smith, PhD
Committee Member

Diane Denny, PhD
Graduate Faculty Representative

JoAnn Canales, PhD
Dean, College of Graduate Studies

August 2013

ABSTRACT

Coastal areas of the Gulf of Mexico are important for many reasons. This part of the United States provides vital coastal habitats for many marine species; the area has seen ever increasing human settlement along the coast, ever increasing infrastructure for marine transportation of the nation's imports and exports through Gulf ports, and ever increasing recreational users of coastal resources. These important uses associated with the Gulf coast are subject to dynamic environmental and physical changes including: coastal erosion (Gulf-wide rates of 25 square miles per year), tropical storm surges, coastal subsidence, and global sea level rise. Coastal land subsidence is a major component of relative sea level rise along the coast of the Gulf of Mexico. These dynamic coastal changes should be evident in changes to the geoid along the coast. The geoid is the equipotential gravity surface of the earth, which best fits the global mean sea level. The geoid has not only been seen as the most natural shape of the Earth, but also serves as the reference surface for most of the height systems. By using satellites (GRACE mission) scientists have been able to measure the large scale geoid for the Earth. A small scale geoid model is required to monitor local events such as flooding, for example, flooding created by storm surges from hurricanes such as Katrina (2005), Rita (2005), and Ike (2008). The overall purpose of this study was to evaluate the accuracy of the local coastal geoid. The more precise geoid will improve coastal flooding predictions, and will enable more cost effective and accurate measurement of coastal topography using global navigation satellite systems (GNSS).

The main objective of this study was to devise mathematical models and computational methods to achieve the best possible precision for evaluation of the geoid in the coastal areas of

the Gulf of Mexico. More specifically, the numerical objectives of this study were to: 1) obtain a continuous map of gravity anomalies and a continuous map of gravity by using spatial interpolation methods and to evaluate errors; 2) solve the Laplace boundary value problem and evaluate errors; and, 3) evaluate precision of the local geoid by using geospatial statistical tools and numerical techniques.

This dissertation investigates modeling of the geoid, especially the gravimetric equipotential surface that approximates mean sea level, in the coastal areas of the Gulf of Mexico as well as errors in the geoid determination. The document begins with Chapter 1 which introduces the study of this dissertation. Different models of kriging are used to determine the precision of the geoid based on the free-air gravity anomalies data supplied by United States Naval Research Laboratory and the airborne gravity data provided by the U.S. National Geodetic Survey, which can be found in Chapters 2 and 3. Research in Chapters 2 shows that more precise evaluation of errors in gravity anomalies can be achieved by using different models of kriging. Results from Chapters 2 and 3 show that ordinary kriging with the stable semivariogram model provide better predictions. Research results from Chapter 3 provide estimation of maximum possible errors in the calculation of the geoid undulation.

The dissertation also investigates behavior of gravity equipotential surfaces around coastal lines and its impact on the geoid evaluation. Chapters 4 and 5 are about evaluation of errors in the Dirichlet problem for calculation of gravity potential with uncertain boundary and boundary values has been achieved by solving the Laplace equation by means of separation of variables. Research has provided a theoretical model in Chapter 4 to estimate very small changes in gravimetric potential relative to the coast. Maximum possible error in the solution of Dirichlet

problem is determined in Chapter 5. Maximum possible error depends on the errors of boundary values and the precision of the boundary itself.

Chapter 6 describes a novel approach to sea level rise modeling. Factor analysis is used to analyze local and global sea level rise and relationships between changing sea levels, currents, and the shape of the Earth. Results of factor analysis from Chapter 6 show that the elevation of sea level relates to the geoid and ocean circulation. Chapter 7 describes the relationship between the geoid and wetlands modeling. Research in Chapter 7 shows that the predicted continuous elevation map obtained through the ordinary stable kriging was sufficiently precise and fairly reliable. Chapter 7 is an exploratory chapter, and the ideas of this chapter will help the future research. Chapter 8 briefly listed conclusions of previous chapters.

In general, this dissertation provides mathematical and statistical foundation for precise evaluations of errors in geoid determination. This knowledge is needed for creation of high quality environmental, coastal and marine models, such as models for marshes restoration.

DEDICATION

This dissertation is dedicated to my sagacious grandfathers, HongKe Zhang and XianFeng Song. I also dedicate this dissertation to my wonderful parents, GuoZhen Zhang and RenTang Song.

ACKNOWLEDGEMENTS

I wish I can express more my gratitude to all who have supported me, and have contributed to this dissertation.

First and foremost, I am very thankful to Dr. Alexey Sadovski, my chair of committee, for his inspiring guidance, intellectual and creative “environment” of research. This dissertation is the “conclusion” of my four years Ph.D. studies at TAMUCC. Alex led me to CMSS program, and for these years, he has been an excellent mentor to me. I am grateful to him for innumerable discussions, professional advice, useful comments, and helping through the process of developing the idea for this dissertation. Moreover, I also have to thank him for granting me Ruth Campbell fellowship in Coastal and Marine Sciences.

I am indebted to Dr. Gary Jeffress, my committee member, for his time, thoughtful comments and suggestions, and for the financial support of my graduate studies he made through Conrad Blucher Institute. My studies could not be finished without this support. I also grateful to Drs. Paul Montagna, Dru Smith who is from National Geodetic Survey at NOAA, Diane Denny, my other committee members, for their expertise, professional advice, comments, time, and patience. Without their efforts, this dissertation could not be possible. Special thanks to Dr. Scott King for his valuable advice and time. I also have to thank him for the effort he put into reading a draft version of this dissertation.

I would like to thank all members of Conrad Blucher Institute for Surveying and Science (CBI) at Texas A&M University—Corpus Christi (TAMUCC) for their support. Special thanks to Gina Concannon and Bea Blomquist for everything they did, and Charles “Tommy” White for solving IT problems.

Many thanks go to National Geodetic Survey at NOAA for providing GRAV-D airborne gravity data used in this study. I wish I can express more my gratitude to all who sharing or providing data used in this study here.

I also would like to extend my gratitude to TAMUCC, College of Graduate Studies, the Harte Research Institute (HRI) administration and staff, the CMSS faculty, and fellow classmates, too numerous to list here.

Last but not least, I would like to thank my parents and good friends for their patience and encouragement over my Ph. D. studies.

TABLE OF CONTENTS

CONTENTS	PAGE
ABSTRACT	v
DEDICATION	viii
ACKNOWLEDGEMENTS	ix
TABLE OF CONTENTS	xi
LIST OF FIGURES	xiv
LIST OF TABLES	xx
CHAPTER I: Introduction.....	1
1.1 Background and relevance	2
1.2 Gulf of Mexico coasts	4
1.3 Purpose and numerical objectives	6
1.4 Dissertation organization	7
1.5 Notes.....	7
1.6 References	7
CHAPTER II: Using Kriging Methods to Determine Free-air Anomalies Continuous Maps	10
2.1 Kriging of FAA data	15
2.2 Inverse distance weighted (IDW) interpolation	46
2.3 FAA applied to geoid undulation and evaluates errors	50

2.4 Acknowledgements	51
2.5 References	51
CHAPTER III: Kriging of Absolute Gravity Data.....	54
3.1 Data	54
3.2 Kriging of gravity on the geoid.....	62
3.3 Kriging of difference between gravity on the ellipsoid and the geoid.....	71
3.4 Acknowledgements	75
3.5 References	76
CHAPTER IV: Computation of the Geoid Downward Corrections in Coastal Areas	79
References	86
CHAPTER V: Evaluation of Errors of Gravity Potentials under the Conditions of	
Uncertainty in the Boundary Value Problems	88
Remarks.....	96
References	96
CHAPTER VI: Sea Level Rise and the Geoid: A Factor Analysis Approach	98
6.1 Introduction	98
6.2 Background	99
6.3 Data	103
6.4 Method	106
6.5 Results	108

6.6 Discussion	110
6.7 Acknowledgements	112
6.8 References	113
CHAPTER VII: The Geoid and Wetland Modeling: The Impact of the Geoid Precision on Wetlands Modeling.....	116
7.1 Background	116
7.2 Data	118
7.3 Method	120
7.4 Result of the ordinary kriging method	122
7.5 Discussion	125
7.6 Acknowledgements	128
7.7 References	129
CHAPTER VIII: Conclusions	131
Appendix 1 Historical Review	133
References	139
Appendix 2 Theoretical Review	141
References	146
Appendix 3 Notes of Universal Kriging with Constant Trend Removed.....	147
Appendix 4 How to Read Semivariogram in ArcGIS 10 and 10.1	151

LIST OF FIGURES

FIGURES	PAGE
Figure 1.1 Illustration depicting the ellipsoid, geoid, and topographic surface (Li and Götze, 2001).	3
Figure 1.2 Gulf of Mexico (NOAA's state of the coast, 2011).	5
Figure 2.1 Regions map of the Gulf of Mexico coasts with the area of data observation in black grid. U.S. National Atlas Water Feature Areas (in light blue) represents the water feature areas (e.g., bays, glaciers, lakes, and swamps) of the United States.	11
Figure 2.2 Frequency histogram with descriptive statistics for FAA data (unit in mgal).	12
Figure 2.3 Normal QQ plot of FAA data (unit in mgal).	12
Figure 2.4 Normal QQ plot of FAA data (unit in mgal). The main departure points from the reference line are selected (in Tourmaline Green).....	13
Figure 2.5 Normal QQ plot of FAA data (unit in mgal). Another main departure points from the reference line are selected (in Tourmaline Green).....	14
Figure 2.6 The anatomy of a typical semivariogram (ESRI).....	16
Figure 2.7 Semivariogram model of the ordinary stable kriging.....	17
Figure 2.8 Semivariogram with all lines (green lines) that fit binned semivariogram values.....	18
Figure 2.9 Semivariogram showing search direction..	19
Figure 2.10 Semivariogram model of the ordinary Gaussian kriging.	19
Figure 2.11 Semivariogram with all lines (green lines) which fit binned semivariogram values.	20
Figure 2.12 Semivariogram showing search direction.	20

Figure 2.13 A semivariogram map..	20
Figure 2.14 A semivariogram map with an example search direction transects (unit in mgal ²).	21
Figure 2.15 Cross validation of the ordinary stable kriging (unit in mgal)	23
Figure 2.16 Cross validation of the ordinary Gaussian kriging (unit in mgal).	24
Figure 2.17 The ordinary stable kriging predictions map (unit in mgal).	26
Figure 2.18 The ordinary stable kriging prediction standard error map (unit in mgal).	27
Figure 2.19 The ordinary Gaussian kriging predictions map (unit in mgal).	28
Figure 2.20 The ordinary Gaussian kriging prediction standard error map (unit in mgal).....	29
Figure 2.21 Trend analysis of FAA.	32
Figure 2.22 De-trend. The order of removal trend is constant (unit in mgal).....	33
Figure 2.23 De-trend. The order of removal trend is first order (unit in mgal).	34
Figure 2.24 Semivariogram of the universal stable kriging with removal of 1st order of trend.	35
Figure 2.25 Semivariogram with all lines (green lines) which fit binned semivariogram values.	35
Figure 2.26 Semivariogram with showing search direction..	36
Figure 2.27 Semivariogram of the universal Gaussian kriging with removal of 1st order of trend.	36
Figure 2.28 Semivariogram with all lines (green lines) which fit binned semivariogram values.	37
Figure 2.29 Semivariogram with showing search direction..	37

Figure 2.30 A semivariogram map. The color band shows semivariogram values with weights (unit in mgal ²).	37
Figure 2.31 A semivariogram map with an example search direction transects (unit in mgal ²).	38
Figure 2.32 An example of searching neighborhood by using the Geostatistical Analyst Tool in ArcGIS 10. Legend is FAA intervals in color band (unit in mgal).	38
Figure 2.33 Cross validation of the universal stable kriging with 1st order of trend removed (unit in mgal).	40
Figure 2.34 Cross validation of the universal Gaussian kriging with 1st order of trend removed (unit in mgal).	41
Figure 2.35 The universal stable kriging predictions map (unit in mgal).	42
Figure 2.36 The universal stable kriging prediction standard error map (unit in mgal).	43
Figure 2.37 The universal Gaussian kriging prediction map (unit in mgal).	44
Figure 2.38 The universal Gaussian kriging prediction standard error map (unit in mgal).	45
Figure 2.39 An example of IDW searching neighborhood by using the Geostatistical Analyst Tool in ArcGIS 10. Legend is FAA intervals in color band (unit in mgal).	46
Figure 2.40 Cross validation of IDW (unit in mgal).	48
Figure 2.41 The IDW prediction map (unit in mgal).	49
Figure 3.1 Tracks and locations of data of airborne gravity. Gravity data plotted by individual block from CS01 to CS04.	56
Figure 3.2 Tracks and locations of data of airborne gravity. Gravity data plotted by four blocks as a group.	57

Figure 3.3 Frequency histogram with descriptive statistics for airborne gravity data (unit in mgal).	57
Figure 3.4 Normal QQ plot of airborne gravity data (unit in mgal).	58
Figure 3.5 The airborne gravity reduced onto the geoid by free-air correction (unit in mgal)....	59
Figure 3.6 Frequency histogram with descriptive statistics for data of gravity on the geoid (unit in mgal).....	60
Figure 3.7 Normal QQ plot of gravity on the geoid data (unit in mgal).....	60
Figure 3.8 Frequency histogram with descriptive statistics for data of gravity on the ellipsoid (unit in mgal).....	61
Figure 3.9 Normal QQ plot of gravity on the ellipsoid data (unit in mgal).....	61
Figure 3.10 Semivariogram model of the ordinary kriging.....	63
Figure 3.11 Semivariogram with all lines (green lines) which fit binned semivariogram values.	63
Figure 3.12 Semivariogram with showing search direction..	63
Figure 3.13 A semivariogram map. The color band shows semivariogram values with weights (unit in mgal ²).	64
Figure 3.14 Cross validation of the ordinary kriging (unit in mgal).....	65
Figure 3.15 The ordinary stable kriging predictions map (unit in mgal).....	66
Figure 3.16 The ordinary stable kriging prediction standard error map (unit in mgal).....	67
Figure 3.17 The ordinary Gaussian kriging predictions map (unit in mgal).	68
Figure 3.18 The ordinary Gaussian kriging prediction standard error map (unit in mgal).....	69
Figure 3.19 Trend analysis of gravity on the geoid.	70

Figure 3.20 Semivariogram model of the ordinary kriging...	71
Figure 3.21 Semivariogram with all lines (green lines) which fit binned semivariogram values..	72
Figure 3.22 Semivariogram with showing search direction.	72
Figure 3.23 A semivariogram map. The color band shows semivariogram values with weights (unit in mgal^2).	72
Figure 3.24 Cross validation of the ordinary kriging (unit in mgal).	73
Figure 3.25 The ordinary kriging predictions map (unit in mgal).	75
Figure 4.1 Matlab code for triple integral.	81
Figure 4.2 Equipotential levels.	82
Figure 4.3 Gravitational potential.	83
Figure 4.4 3D graph of equipotential surfaces of the vertical cut through the point (0,0,0)...	84
Figure 4.5 Geometrical straight line (blue) and plumb line (red) after rotation.	85
Figure 5.1 Spherical and rectangular coordinates (Hofmann-Wellenhof & Moritz, 2006)....	88
Figure 5.2 Legendre's polynomials as function of $t=\cos\theta$. Top: n is even; Bottom: n is odd....	93
Figure 6.1 Past and projected global average sea level.	100
Figure 6.2 Perspective view of inundation of the Corpus Christi Bay area by sea level rise.....	102
Figure 6.3 Data from each region represented in the world map.....	103
Figure 6.4 Mean sea level dataset from 1992 to 2011.	104
Figure 6.5 Sea level variations: 2 years running averages.	105
Figure 6.6 Sea level variations: 5 years running averages.	106

Figure 6.7 Scree plot	108
Figure 7.1 Illustration of Key Parameters for Wetland Migration Modeling	116
Figure 7.2 Nueces Delta Elevation Control data displaced as each site.	119
Figure 7.3 Nueces Delta Elevation Control locations in Site 1.	120
Figure 7.4 Semivariogram Model of the Ordinary Kriging.	121
Figure 7.5 A semivariogram map. The color band shows semivariogram values with weights (unit in meter ²).	121
Figure 7.6 The predicted graph.	122
Figure 7.7 The error graph. The blue line represents the error equation (unit in meter).	123
Figure 7.8 The standardized error graph.	123
Figure 7.9 The normal QQ plot of the standardized error.	124
Figure 7.10 The ordinary kriging prediction elevation map with color symbol ranged within elevation values (unit in meter).	125
Figure 7.11 Map of Nueces Marsh (Rasser, 2009).	126
Figure 7.12 A conceptual model.	128

LIST OF TABLES

TABLES	PAGE
Table 2.1 Cross validation statistics compared between the stable and the Gaussian techniques (unit in mgal).	22
Table 2.2 Comparison of the components of stable and Gaussian semivariogram (unit of nugget, partial sill and sill are mgal^2 ; unit of range is degree).	35
Table 2.3 Cross validation statistics compared between the stable and the Gaussian techniques (unit in mgal).	39
Table 3.1 Nominal block and survey characteristics (GRAV-D Science Team, 2012).	55
Table 3.2 Comparison of the components of stable and Gaussian semivariogram (unit of nugget, partial sill and sill are mgal^2 ; unit of range is degree).	62
Table 3.3 Statistics (unit in mgal).	71
Table 3.4 Statistics (unit in mgal).	74
Table 6.1 Communalities of mean sea level.	107
Table 6.2 Table of total variance for three components solution.	108
Table 6.3 Factor loadings for rotated component matrix.....	110
Table 6.4 Table of total variance explained (Sadovski, A. et al., 2010).	111
Table 6.5 Factor loading for rotated component matrix (Sadovski, A. et al., 2010).	111

Chapter 1: Introduction

Coastal areas have been shaped by the rise and fall at seas, and have also been shaped by river flows in some regions of coasts. Sea level change is globally considered as a consequence of climate change, but sea level change in coastal areas is also associated with vertical movements of the land. Coastal areas are situated at the interface between the land and water. Hence, coastal areas are influenced by both terrestrial and oceanic processes and events. Storms and floods are among the heaviest threats to the habitation of coastal areas. The increasing vulnerability of coastlines to environmental change needs for accurate elevations, which requires the need of precision of the geoid. However, precision of the large scale geoid model is not sufficient to monitor local events such as flooding, for example, flooding created by storm surges from hurricanes such as Katrina (2005), Rita (2005), and Ike (2008). Thus, the overall purpose of this research is to evaluate the accuracy of the local coastal geoid.

Geodesists and cartographers who study the measurement of the size and shape of the Earth are interested in sea level as an elevation datum. This datum is known as the geoid. The geoid is defined as the equipotential gravity surface of the Earth, and theoretically best fits global mean sea level (Hofmann-Wellenhof & Moritz, 2006). The shape of the geoid reflects the information of the interior of the Earth's material structure, density and distribution, which has a significant effect on research and applications in oceanography, seismology, geophysics, geological prospecting, oil exploration, and other related Earth science. The geoid is not only considered as the most natural shape of the Earth, but also it serves as the reference surface for most of the height systems. Therefore, it is essential to understand the determination of the geoid in the coastal areas. With enhanced understanding of the geoid, the methods applied for the geoid

determination are diverse. The demand for precise evaluation of the geoid is keeping pace with the rapid development of accurate gravity measurements.

1.1 Background and relevance

In classical geodesy, the earth's gravity fields to geodesy play a supporting role in relative positioning. It is mainly used in defining the reference ellipsoid and its orientation, and in determining the ground observation data (distance, direction, etc.) attributed to the reference ellipsoid surface. The approach of modern geodesy is to apply spatial techniques that are three-dimensional geocentric global Earth measurements. The precise definition of gravity fields plays a critical role in spatial geodesy:

- 1) The geoid is the elevation datum from which to obtain geographical spatial information;
- 2) High-precision GPS technology combined with a high-resolution geoid model to replace the traditional standard of measurement in determination of heights or normal height, which truly achieves GPS technology in the geometric and physical meaning of three-dimensional positioning function;
- 3) Precise time-varying information of the gravity fields helps research and understanding of such geodynamic phenomena, so as to support important scientific studies in monitoring environmental resources, reducing or preventing damage and devastation caused by weather events.

Determining the geoid combines geometric geodesy and geodetic science not only to assist in determining the geometric spatial location, but also to acquire the relationship between altitude and the Earth's gravitational field.

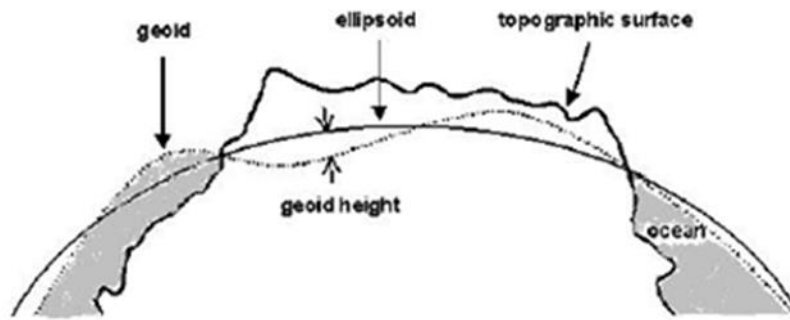


Figure 1.1 Illustration depicting the ellipsoid, geoid, and topographic surface (Li and Götze, 2001).

There are three different surfaces that fit the requirement of global geodetic applications (Li & Götze, 2001). They are the topographic surface, the reference ellipsoid and the geoid (Figure 1.1). The topographic surface, which is the landmass topography as well as the ocean bathymetry, is highly irregular. The ellipsoid is a geometric or mathematical reference surface, and the geoid is the equipotential of the Earth's gravity field which best fits the global mean sea level (Hofmann-Wellenhof & Moritz, 2006; www.ngs.noaa.gov/GEOID/). In other words, the geoid means that at any point it is perpendicular to the direction of gravity. In today's satellite age, the modern approach for satellite positioning is the Navigation System using Time and Ranging (NAVSTAR), which is known as the global positioning system (GPS) (Smith, 1997). The ellipsoid height can be geometrically determined within only a few centimeters of accuracy by the global navigation satellite system (GNSS) (Sadovski et al., 2009). Compared with using GPS, a faster and more economical approach, is to use geoid models with the same accuracy as GPS, or produce orthometric heights with better accuracy. Additionally, the geoid models can be established almost everywhere (Sadovski et al., 2009). The geoid modeling has been based on

Stokes (Heiskanen & Moritz, 1967) and Molodensky's (Telford et al., 1990) theories. In both theories, including the theories of gravity and topography reductions, which are of fundamental importance for determination of the precise geoid, a lot of assumptions have to be made to achieve desired results. As mentioned in Sadovski et al.'s paper (2009) "...Due to the massive and still improving knowledge of the Earth's surface, fixed-boundary value problems seem more adequate and theoretical and numerical studies along this line are not only important in practice, but also may lead to a fundamental change in physical geodesy...".

By using satellites, scientists discovered the long wave (large scale) geoid for the Earth (Seeber, 2003; Drinkwater et al., 2003), but its resolution is not sufficient for orthometric height determination from GPS when it comes to relatively small scale and/or local events such as flooding. This was the case after flooding created by storm surges from hurricanes Katrina (2005), Rita (2005), and Ike (2008) in the coastal areas of the Gulf of Mexico. So, there is a need to develop methods of the geoid evaluation at the local level, based on local gravity observations, and complemented by gravity observations from air and space.

1.2 Gulf of Mexico coasts

The Gulf of Mexico is the ninth largest water body in the world. It is bordered by three countries: the United States, Mexico, and Cuba (Figure 1.2). Along the U.S. coastline of the Gulf of Mexico, there are five states: Florida, Alabama, Mississippi, Louisiana, and Texas. This coastline extends from the western Florida Keys to the southern tip of Texas. The area of the Mexico Gulf is approximately 1.5022×10^{12} square meters (580,000 square miles). The Gulf of Mexico is also the largest semi-enclosed coastal water of the Western Atlantic (Heileman and

Rabalais). Gulf water is around 2.4342×10^{15} cubic meters (584,000 cubic miles), and the average depth is 1615.14 meters (5,299 feet) (NOAA's state of the coast, 2011).



Figure 1.2 Gulf of Mexico (NOAA's state of the coast, 2011).

The Gulf of Mexico has had an accelerated loss of coastal lands over the last 50 years. Coastal wetlands are lost at rate of 25 square miles per year (NOAA's Oil Spill Response, 2010). Loss of wetlands and shoreline erosion are considered a challenge and consequence of climate change and, especially, sea level rise now and in the future. The impact of sea level changes on coastal sedimentary environments can be expected (Davis, 1987). As sea levels rise, shorelines will respond by flooding or eroding. Erosion explains most of the net shoreline recession on beaches and barrier islands, such as the east coast of the U.S., while flooding accounts for most of the loss in wetlands and subsiding deltas, such as along the Mississippi (Eisma, 1995). Although shoreline recession can be divided into those two different categories, the processes of

erosion and flooding are closely related. Shorelines may initially be submerged, then erosion begins when embayment and shallow bodies of open water become large enough to adapt to storm waves (Wells & Coleman, 1987). For example, this appears to have happened during the widespread internal fragmentation of some wetlands in the Gulf of Mexico.

1.3 Purpose and numerical objectives

The purpose of this research is to find contributing errors to the accuracy evaluation of the coastal geoid in the Gulf of Mexico and to determine effect of these contributing errors on the estimation of water levels in coastal wetlands in the events of tropical storms, floods, tsunamis, and other natural catastrophes.

Smith and Milbert (1999) suggested that the greatest errors in the Geoid determination only happen in two kinds of situations. One is in the mountain terrain due to sharp variations; the other is in the coastal areas when water and the lands quite different in nature and density are brought together. Therefore, the main objective of this research is to devise mathematical models and computational methods to achieve the best possible precision (depending on the quality and quantity of data) for evaluation of the geoid in the coastal areas of the Gulf of Mexico. In other words, evaluate errors uses different metric spaces of functions in this study. In such a way, the worst case scenario can be evaluated, meaning the “largest possible” errors. However, generally in geosciences field, errors are measured by finding differences between predicted values and measured values. More specifically, the numerical objectives of the research include:

- To obtain a continuous map of gravity anomalies and a continuous map of gravity using spatial interpolation methods.
- To evaluate errors of absolute gravity and maximum possible errors in geoid undulation.
- To solve the Laplace boundary value problem.

- Evaluate errors of the gravity potential under the conditions of uncertainty in the boundary and boundary values.
- To evaluate precision of the local geoid by using geospatial statistical tools and numerical techniques.

Another objective of the research is using quantitative measures of sea level rise to investigate the relationship between sea level rise and the shape of the Earth.

1.4 Dissertation organization

This dissertation is organized into seven chapters. Chapter 1: Introduction includes introduction of the research, background and relevance, Gulf of Mexico coasts, purpose and numerical objectives, dissertation organization, and references. Chapter 2: Finding continuous map of free-air anomalies by kriging methods; and Chapter 3: Kriging of absolute gravity data. Chapter 4: Computation of the geoid downward corrections in coastal areas. Chapter 5: Evaluation of errors of gravity potentials under the conditions of uncertainty in the boundary value problems. Chapter 6 and Chapter 7 are applications. Chapter 6: Sea level rise and the geoid: A factor analysis approach; and, Chapter 7: The Geoid and wetland modeling: The impact of the geoid precision on wetlands modeling. Chapter 8: Conclusions which includes the major findings of the dissertation.

1.5 Notes

For more information on historical and theoretical reviews, please see Appendices 1 and 2.

1.6 References

Davis Jr., R. A., & Clifton, H. E. (1987). Sea-level change and the preservation potential of wave-dominated and tide-dominated coastal sequences. *Sea-Level Fluctuation and Coastal Evolution*. 166-178.

- Day, J. W., Christian, R. R., Boesch, D. M., Yáñez-Arancibia, A., Morris, J., Twilley, R. R., Naylor, L., & Schaffner, L. (2008). Consequences of climate change on the ecogeomorphology of coastal wetlands. *Estuaries and Coasts*, 31 (3), 477-491.
- Drinkwater, M. R., Floberghagen, R., Haagmans, R., Muzi, D., & Popescu, A. (2003). VII: CLOSING SESSION: GOCE: ESA's First Earth Explorer Core Mission. *Space Science Reviews*, 108 (1-2), 419-432.
- Eisma, D. (Ed.) (1995). *Climate change: Impact on coastal habitation*. Boca Raton, Ann Arbor, London, Tokyo: Lewis Publishers.
- Heileman, S., & Rabalais, N. XV-50 Gulf of Mexico: LME # 5. Available from:
http://www.lme.noaa.gov/LMEWeb/LME_Report/lme_5.pdf.
- Heiskanen, W. A., & Moritz, H. (1967). *Physical geodesy*. San Francisco, London: Freeman.
- Hofmann-Wellenhof, B., & Moritz, H. (2006). *Physical geodesy* (2nd ed.). New York: Springer Wien.
- Li, X., & Götze, H. J. (2001). Tutorial ellipsoid, geoid, gravity, geodesy, and geophysics. *Geophysics*, 66, 1660-1668.
- National Oceanic and Atmospheric Administration and U. S. Department of Commerce. (2010). *NOAA's oil spill response. Shorelines and coastal habitats in the Gulf of Mexico*. Available from: <http://response.restoration.noaa.gov/deepwaterhorizon>.
- NOAA's state of the coast. (2011). *The Gulf of Mexico at a glance: a second glance*. Explore coastal communities, economy, and ecosystems.

- Sadovski, A., Jeffress, G., Song, H. Z., & Warner, N. (2009). Some mathematical problems of the geoid determination in the coastal areas of the Gulf of Mexico. *Recent advances in Applied Mathematics and Computational and Information Sciences, 1*, 177-182.
- Seeber, G. (2003). *Satellite geodesy* (2nd ed.). Berlin, New York: Walter de Gruyter.
- Smith, D. A., & Milbert, D. G. (1999). The GEOID96 high-resolution geoid height model for the United States. *Journal of Geodesy, 73*(5), 219-236.
- Smith, J. R. (1997). *Introduction of geodesy: The history and concepts of modern geodesy*. New York, Chichester, Weinheim, Brisbane, Singapore, Toronto: John Wiley & Sons, Inc.
- Telford, W. M., Geldart, A. P., & Sheriff, R. E. (1990). *Applied Geophysics* (2nd ed.). Cambridge, New York, Port Chester, Melbourne, Sydney: Cambridge University Press.
- The Official NGS GEOID Page. Available from: www.ngs.noaa.gov/GEOID/.
- Wells, J. T. & Coleman, J. M. (1987). Wetland loss and the subdelta life cycle. *Estuarine Coastal Shelf Sciences, 25* (1), 111-125.

Chapter 2: Using Kriging Methods to Determine Free-air Anomalies Continuous Maps

In today's satellite age, the modern approach of using satellite based positioning techniques, especially global positioning systems (GPS), is very popular during geodetic and surveying work. Using GPS can be quicker and easier than using leveling in determining positions; however, there is a faster and more economical approach, which is to use geoid models associated with modern technology. Therefore, geodesists and surveyors are focusing greater attention on deriving more precise geoid models. This chapter focuses on the theory of geoid modeling and evaluates the level of precision when geoid approximation is obtained by using Free Air Anomaly (FAA) data.

There are two common interpolation techniques used to produce a prediction of a random field (Reguzzoni *et al.*, 2005). One is least-square collocation, which is mainly used in geodesy; the other technique that is mainly used in geology and hydrology is called kriging. Besides these two techniques, other spatial interpolations, such as inverse distance weighting (IDW) and splines are also utilized to conduct a comparison. A comparison of the different interpolation techniques is important to minimize errors.

Data sample (Figure 2.1) used in this chapter is free-air gravity anomaly (FAA) data, which was supplied by United States Naval Research Laboratory (USNRL) along meridians and parallels (A. Sadowski, personal communication, September 17, 2009). The total sample size is 21095, and the FAA values range between -23.22 mgal¹ and 26.21 mgal. Normality of sampling distribution is tested for determining kriging methods. Therefore, skewness and kurtosis are examined within the FAA data (Figure 2.2). The skewness is 0.23, which is a slightly right

¹ Gravity is measured in gal (1 gal = 1 cm/s²). The unit is being named in honor of Galileo Galilei. For convenient use, the milligal, abbreviated mgal (1 mgal = 10⁻³ gal).

skewed distribution. The values are more concentrated on the left of mean 0.20 mgal. The kurtosis is 2.36, which is more flattened than a normal distribution with a wide peak (platykurtic). Points on the Normal QQ Plot (Figures 2.3 to 2.5) also deviate from the reference line represented in black line. In Figure 2.3, FAA values of the standard normal distribution are plotted on the x-axis in the Normal QQ Plot, and the corresponding FAA values of the dataset are plotted on the y-axis. The main departure points from the reference line are selected and the locations of these selected points are highlighted in Tourmaline Green in Figures 2.4 and 2.5.

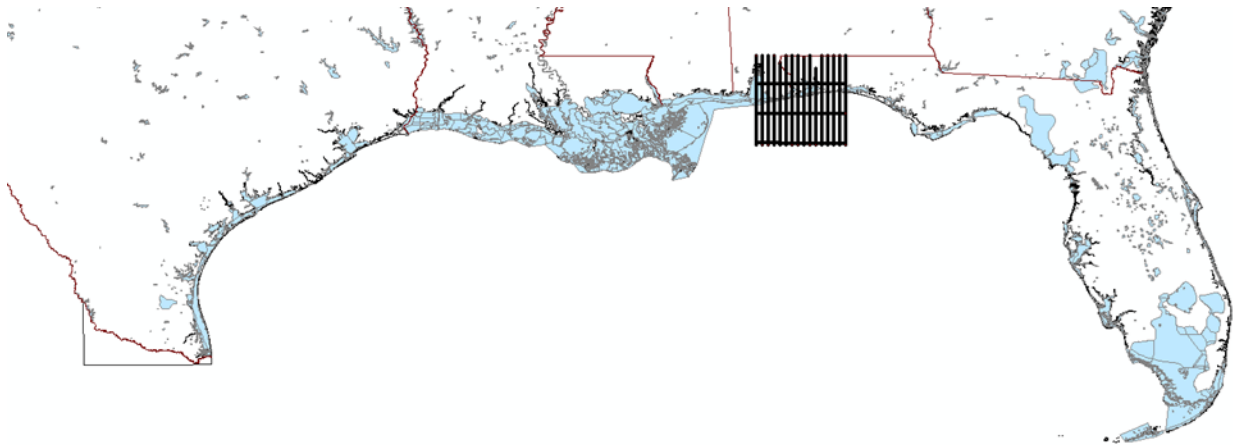


Figure 2.1 Regions map of the Gulf of Mexico coasts with the area of data observation in black grid. U.S. National Atlas Water Feature Areas (in light blue) represents the water feature areas (e.g., bays, glaciers, lakes, and swamps) of the United States.

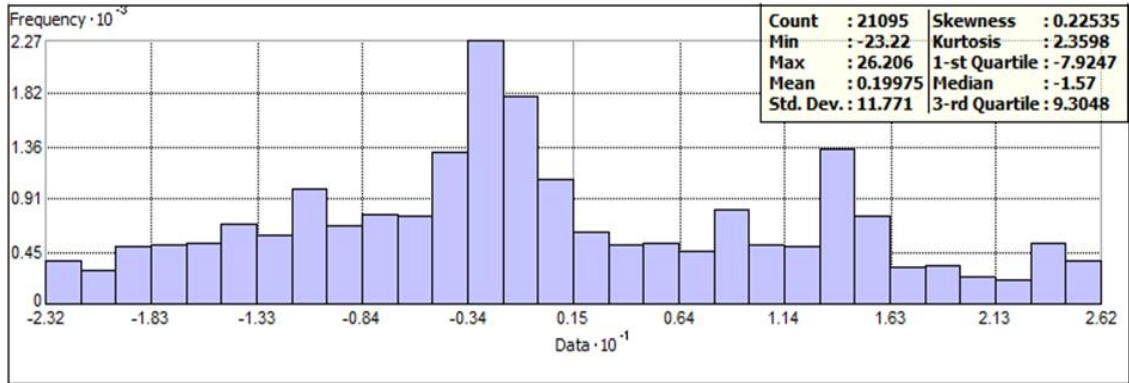


Figure 2.2 Frequency histogram with descriptive statistics for FAA data (unit in mgal).

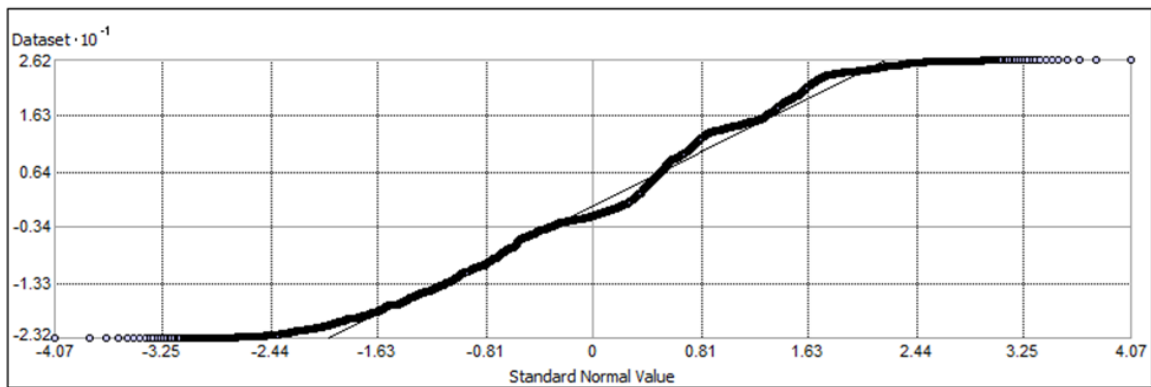


Figure 2.3 Normal QQ plot of FAA data (unit in mgal).

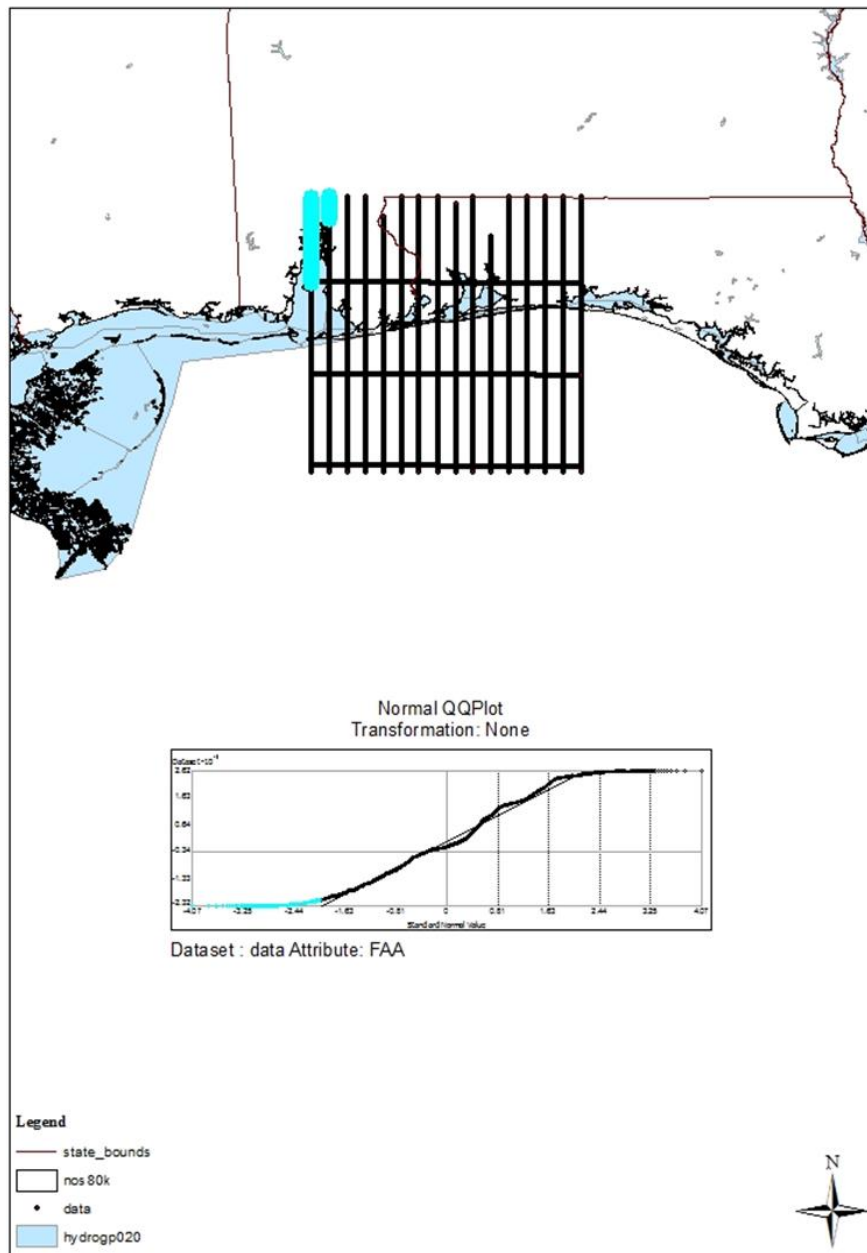


Figure 2.4 Normal QQ plot of FAA data (unit in mgal). The main departure points from the reference line are selected (in Tourmaline Green). The corresponding locations of these selected points are highlighted in Tourmaline Green in the area of data observation (in black grid).

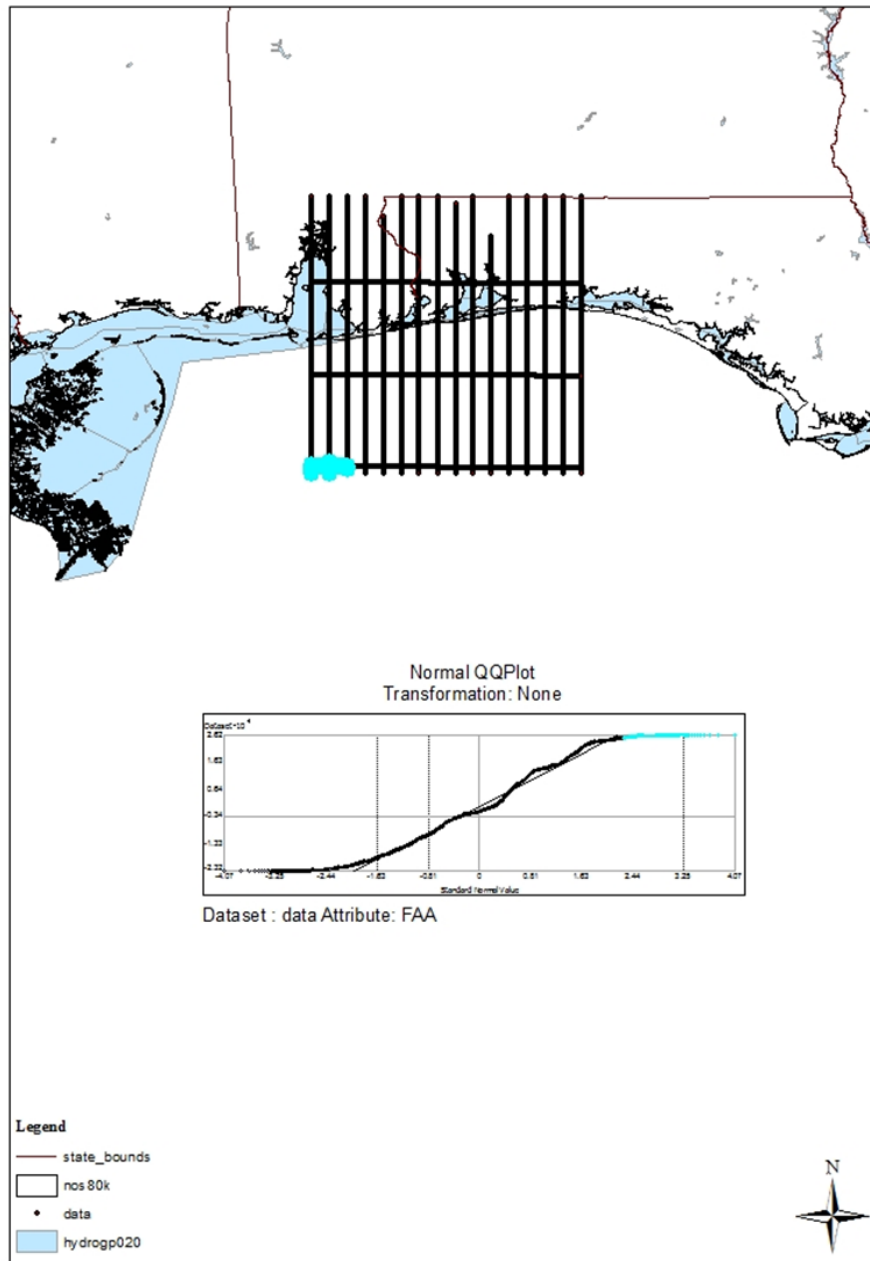


Figure 2.5 Normal QQ plot of FAA data (unit in mgal). Another main departure points from the reference line are selected (in Tourmaline Green). The corresponding locations of these selected points are highlighted in Tourmaline Green in the area of data observation (in black grid).

2.1 Kriging of FAA data

Gravity anomalies are variations in gravity over a given areas. FAA is given by:

$$\Delta g_{FAA} = g_o - g_n + g_{FAC} \quad (2.1)$$

where g_o is the value of the observed gravity; g_n is the normal gravity; g_{FAC} is the free-air correction which is given in Equation 2.2, and h is the elevation depends on latitude.

$$g_{FAC} = 0.3086 \times h \quad (2.2)$$

To make a global free-air gravity anomaly map, we want to have FAA measurements at every point of the Earth's surface; however, this is an impossible task to be performed in the real world. Using the kriging method to predict values of a random unsampled area from a set of observations is an approach to meet this need. As a prediction, errors do exist during the process of kriging method. Thus, in addition to creating a continuous surface of gravity anomalies, evaluating errors is also needed in this chapter. Fortunately, the kriging method can also estimate the prediction error to assess the quality of a prediction.

The kriging method here was conducted by using ArcGIS 10—Spatial Analyst and Geostatistical Analyst. There are six types of kriging in Geostatistical Analyst tools. The most common types are ordinary kriging and universal kriging, which were chosen to be used in this study. The simple kriging method is also quite common, but it requires the data should have a normal distribution. Thus, the simple kriging method was not applied in this study. There are three major components—the spatial autocorrelation component (known as semivariogram), a trend, and a random error term. These three components are the key to lead to different types of the kriging methods. The simple equation represents the kriging method is:

$$z_s = \sum_{i=1}^n z_i w_i, \quad (2.3)$$

where z_s is the estimated value for an unsampled location s ; z_i is the known value at the control point i ; w_i represents the weight applied to sample values associated with the control point i ; n is the number of sample points used in the estimation.

2.1.1 Ordinary kriging

Ordinary kriging is the original formulation of kriging (Cressie, 1990). The ordinary kriging method is based on unknown trends, and focuses on spatial autocorrelation. A semivariogram (Figure 2.6) can be used to explore spatial autocorrelation. The semivariance is computed by,

$$\gamma(h) = \frac{1}{2} [z(x_i) - z(x_j)]^2, \quad (2.4)$$

where $\gamma(h)$ is the semivariance between known points x_i and x_j separated by the distance h ; and z stands for the value at a known point.

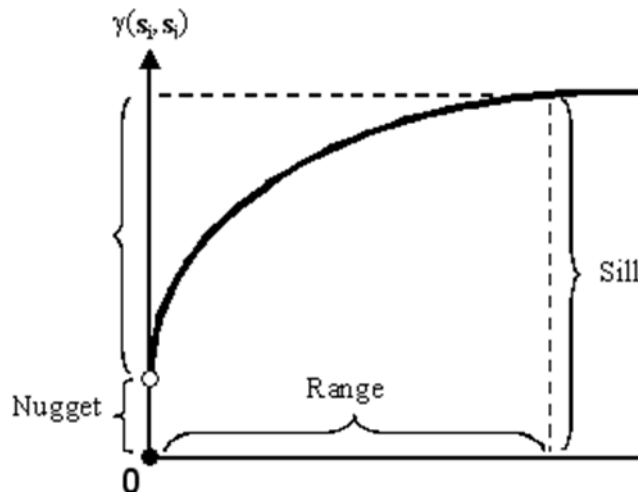


Figure 2.6 The anatomy of a typical semivariogram (ESRI).

Namely, in ArcGIS 10, the graph (Figure 2.7) of the empirical semivariogram is computed as,

$$\text{Semivariogram (distance } h) =$$

$$\frac{1}{2} \times \text{average} [(value\ at\ location\ i - value\ at\ location\ j)^2] \quad (2.5)$$

for all pairs of locations separated by distance h .

In other words, semivariogram can be defined as,

$$\gamma(h) = \frac{1}{2} \text{var}[z(x_i) - z(x_j)], \quad (2.6)$$

where var means variance.

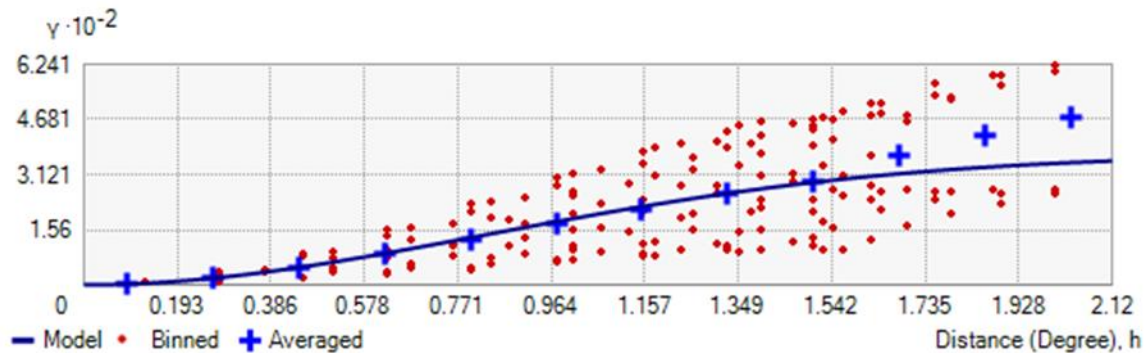


Figure 2.7 Semivariogram model of the ordinary stable kriging. The averaged semivariogram values on the y-axis (in mgal^2), and distance (or lag) on the x-axis (in degree). Binned values are shown as red dots, which are sorted the relative values between points based on their distances and directions and computed a value by square of the difference between the original values of points; Average values are shown as blue crosses, which are generated by binning semivariogram points; The model is shown as blue curve, which is fitted to average values. Model: $0.24582 \times \text{Nugget} + 369.12 \times \text{Stable}(2.1204, 1.9385)$.

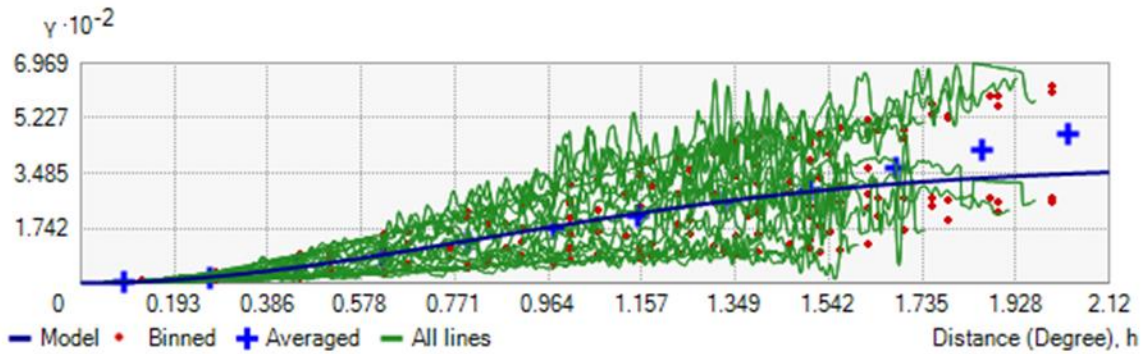


Figure 2.8 Semivariogram with all lines (green lines) that fit binned semivariogram values. The averaged semivariogram values on the y-axis (in mgal^2), and distance (or lag) on the x-axis (in degree).

According to the First Law of Geography (Tobler, 1970), points nearby should be more similar in value than points further away. The plots of each pair of the location were binned to average semivariance data by distance and direction, and the model fit through the averaged binned values at the distance (Figures 2.5 to 2.14). Spatial statistics techniques assume that spatial autocorrelation exists in range. The range is approximately 2.1204 degree of the stable model (Figures 2.7 to 2.9), and it is approximately 2.0244 degree of the Gaussian model (Figures 2.10 to 2.12). Namely, values behind this range start to flatten out (are approximately constant), and the spatial autocorrelation does not exist anymore or little. Another important parameter of the semivariogram model is called the nugget. The nugget represents independent error, measurement error, or microscale variation. The nugget in semivariogram model with the stable technique is 0.2458 mgal^2 , and with the Gaussian technique is 0.7551 mgal^2 . The independent error in semivariogram model with the stable technique is quite smaller than it is with the Gaussian technique. The last parameter is the sill, which represents the value of the semivariogram at the distance. Only variables become uncorrelated behind the range, the sill of the semivariogram will be equivalent to the variance of the random variable. The sill, which is comprised of the nugget and partial sill, shows the variation between the data values. The partial

sill of the semivariogram in Figures 2.7 to 2.9 is 369.1191 mgal^2 and in Figures 2.10 to 2.12 is 360.2210 mgal^2 . The variation between FAA data values is smaller by using the Gaussian technique than using the stable technique.

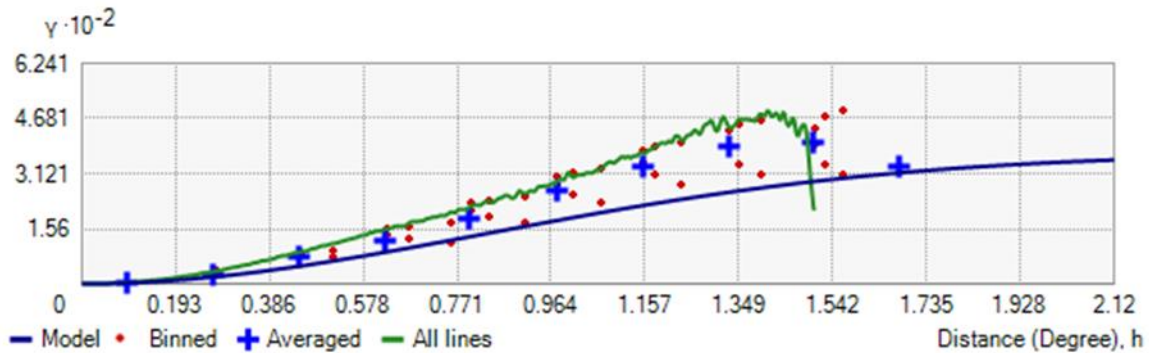


Figure 2.9 Semivariogram showing search direction. The tolerance is 45 and the bandwidth (lags) is 3. The local polynomial shown as a green line fits the semivariogram surface in this case. The averaged semivariogram values on the y-axis (in mgal^2), and distance (or lag) on the x-axis (in degree).

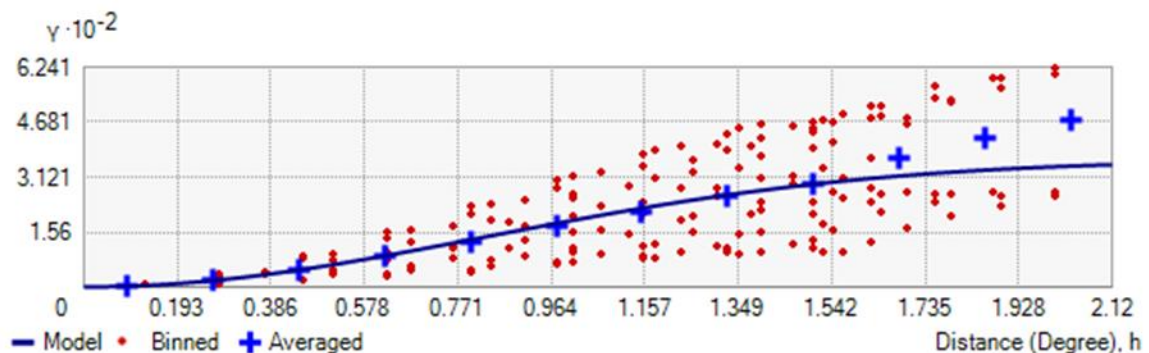


Figure 2.10 Semivariogram model of the ordinary Gaussian kriging. The averaged semivariogram values on the y-axis (in mgal^2), and distance (or lag) on the x-axis (in degree). Binned values are shown as red dots, which are sorted the relative values between points based on their distances and directions and computed a value by square of the difference between the original values of points; Average values are shown as blue crosses, which are generated by binning semivariogram points; The model is shown as blue curve, which is fitted to average values. Model: $0.75508 \cdot \text{Nugget} + 360.22 \cdot \text{Gaussian}(2.0244)$.

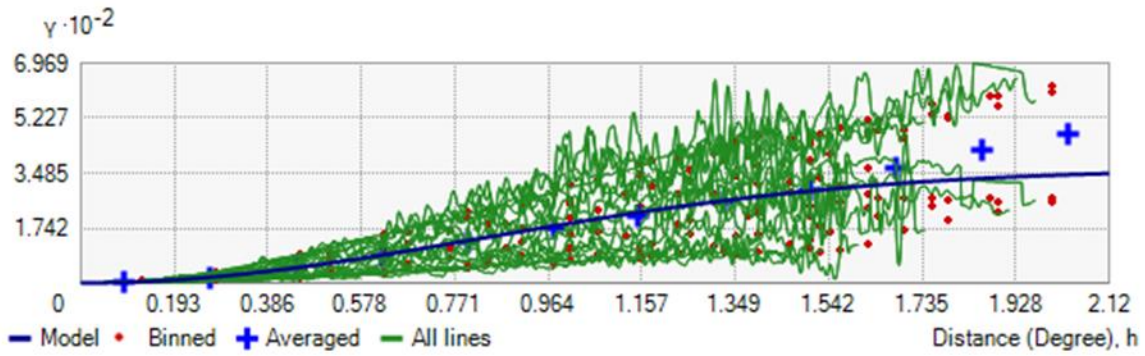


Figure 2.11 Semivariogram with all lines (green lines) which fit binned semivariogram values. The averaged semivariogram values on the y-axis (in mgal^2), and distance (or lag) on the x-axis (in degree).

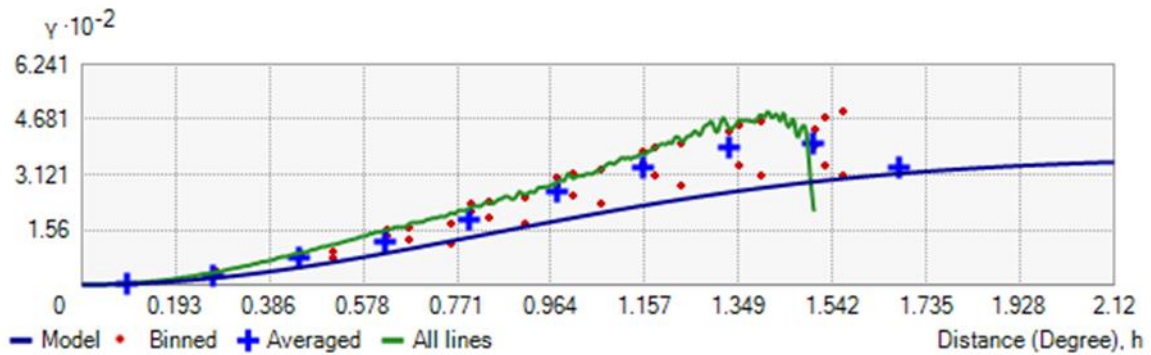


Figure 2.12 Semivariogram showing search direction. The tolerance is 45 and the bandwidth (lags) is 3. The local polynomial shown as a green line fits the semivariogram surface in this case. The averaged semivariogram values on the y-axis (in mgal^2), and distance (or lag) on the x-axis (in degree).

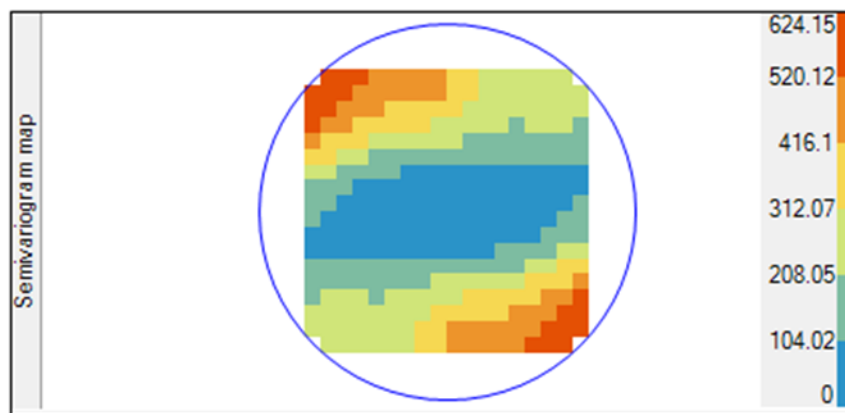


Figure 2.13 A semivariogram map. The color band shows semivariogram values with weights (unit in mgal^2).

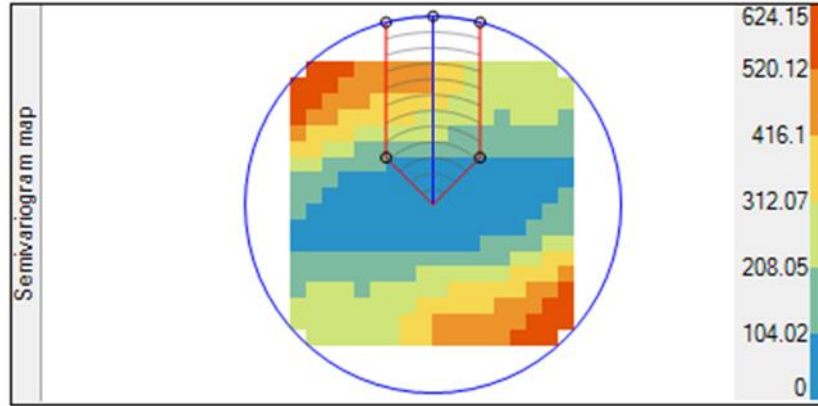


Figure 2.14 A semivariogram map with an example search direction transects (unit in mgal^2).

The techniques used to determine which type of the ordinary kriging method gave a better predicted continuous FAA surface are:

1. Cross validation;
2. Direct visual comparisons of the graphs.

The cross validation is a common statistical technique to compare interpolation methods (Elhomme, 1978). This estimate aims to calculate the model error. The two common statistics are the root mean square (RMS) and standardized RMS:

$$RMS = \sqrt{\frac{1}{n} \sum_{i=1}^n (z_{i,obs} - z_{i,est})^2} \quad (2.7)$$

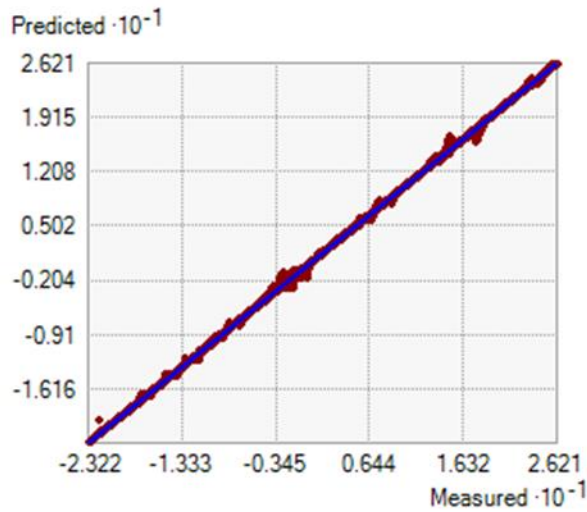
$$Standardized\ RMS = \sqrt{\frac{1}{n} \sum_{i=1}^n \frac{(z_{i,obs} - z_{i,est})^2}{s^2}} = \frac{RMS}{s} \quad (2.8)$$

where n is the number of sample points; $z_{i,obs}$ is the known value of point i ; $z_{i,est}$ is the estimated value of point i ; s^2 is the variance.

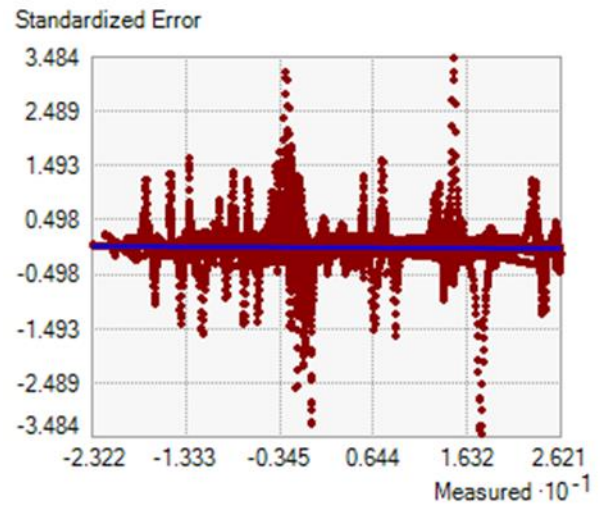
Cross-validation statistics	Prediction Model 1	Prediction Model 2
	O.K.- Stable	O.K.-Gaussian
RMS Standardized	0.2556	0.3275
Mean Standardized	-0.0006	-0.0067
Average Standard Error (ASE)	0.5187	0.9003
Root Mean Square (RMS)	0.1309	0.2935
Difference between RMS and ASE	0.3878	0.6068
Difference in Percentage	74.76%	67.40%

Table 2.1 Cross validation statistics compared between the stable and the Gaussian techniques (unit in mgal).

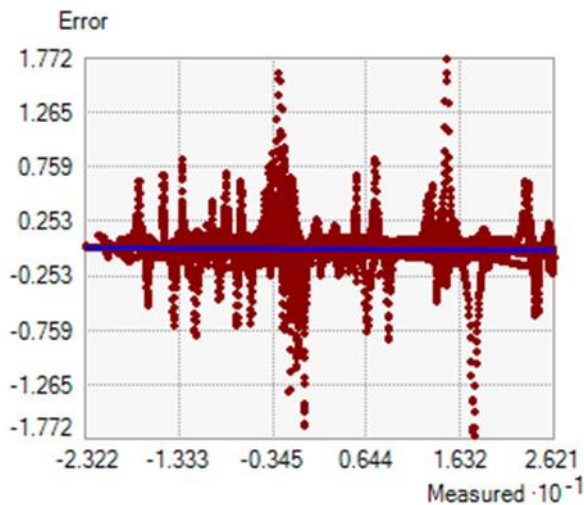
The standardized RMS should approach to one, and the standardized mean should be close enough to zero. The average standard error (ASE) and RMS should be as small as possible. The ordinary kriging method using the stable technique meets most criteria (Table 2.1). However, the ordinary kriging method using the Gaussian technique has slightly better standardized RMS.



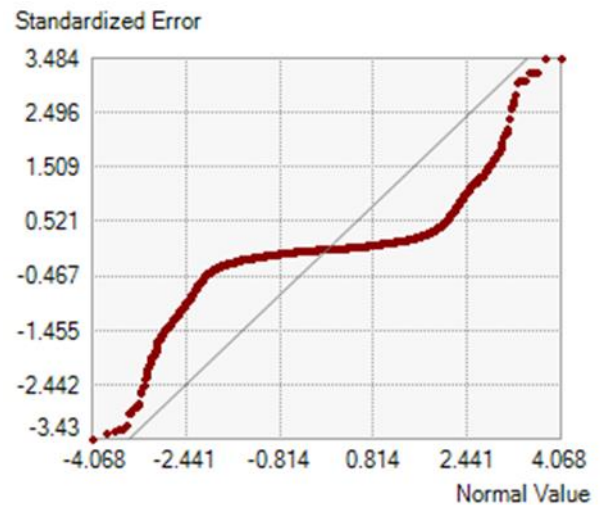
A.



C.



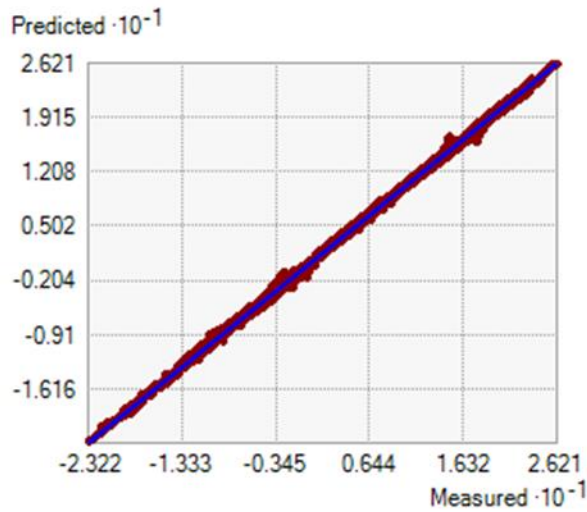
B.



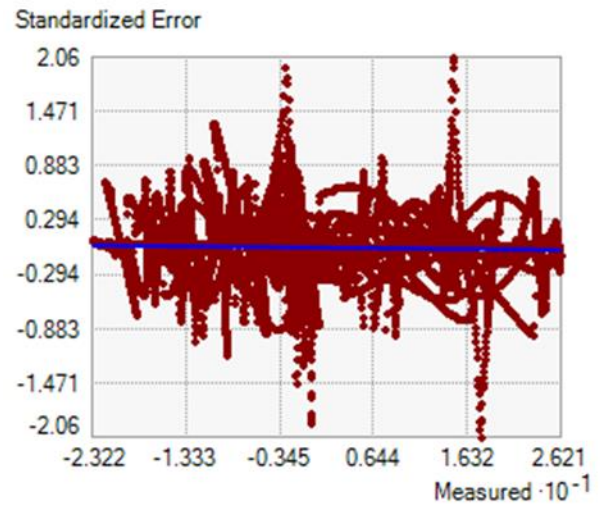
D.

Figure 2.15 Cross validation of the ordinary stable kriging (unit in mgal).

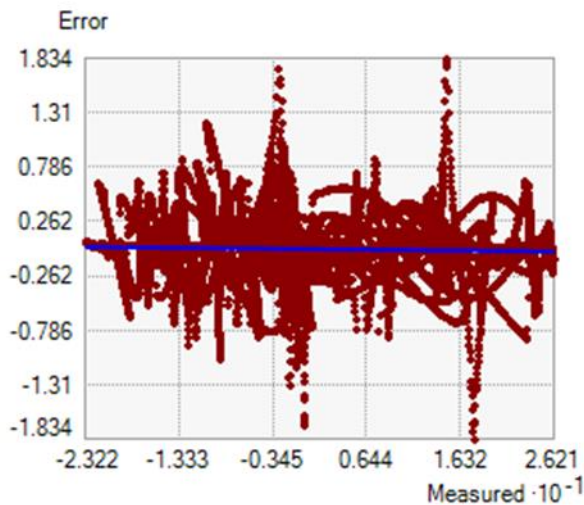
- A. The predicted graph. The blue line represents the regression function, and the black line represents the reference line;
- B. The error graph. The blue line represents the error equation;
- C. The standardized error graph. The blue line represents the standardized error equation;
- D. The normal QQ plot of the standardized error. The reference line is represented by the black line.



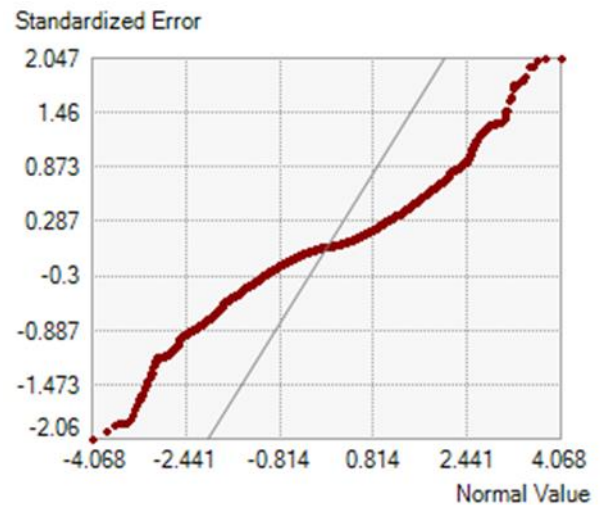
A.



C.



B.



D.

Figure 2.16 Cross validation of the ordinary Gaussian kriging (unit in mgal).

- A. The predicted graph. The blue line represents the regression function, and the black line represents the reference line;
- B. The error graph. The blue line represents the error equation;
- C. The standardized error graph. The blue line represents the standardized error equation;
- D. The normal QQ plot of the standardized error. The reference line is represented by the black line.

The Predicted, error, standard error, and normal QQ plot graphs are plotted respectively in Figures 2.15 and 2.16. The predicted graph shows how well the known sample value was predicted compared to its actual value. The regression function in Figure 2.15A is $f(x)_S = 0.9996x - 0.008$ and in Figure 2.16A is $f(x)_G = 0.9991x - 0.0029$. By visually analyzed the graphs, both regression function are closely aligned with the reference line. Therefore, both of them are good models, but the ordinary kriging method with the stable technique looks better than the one with the Gaussian technique because it looks much closer aligned on.

The error graph shows the difference between known values and predictions for these values. The error equation in Figure 2.15B is $y_S = -0.0004x - 0.0008$, and in Figure 2.16B is $y_G = -0.0009x - 0.0029$. The standardized error graph shows the error divided by the estimated kriging errors. The standardized error equation in Figure 2.15C is $y_S = -0.0008x - 0.0017$, and in Figure 2.16C is $y_G = -0.0010x - 0.0033$. The normal QQ plot of the standardized error shows how closely the difference between the errors of predicted and actual values align with the standard normal distribution (the reference line). Figures 2.17 to 2.20 display the prediction and standard error map by using the ordinary kriging with stable and Gaussian techniques. The standard error displayed in Figure 2.18 is smaller than in Figure 2.20.

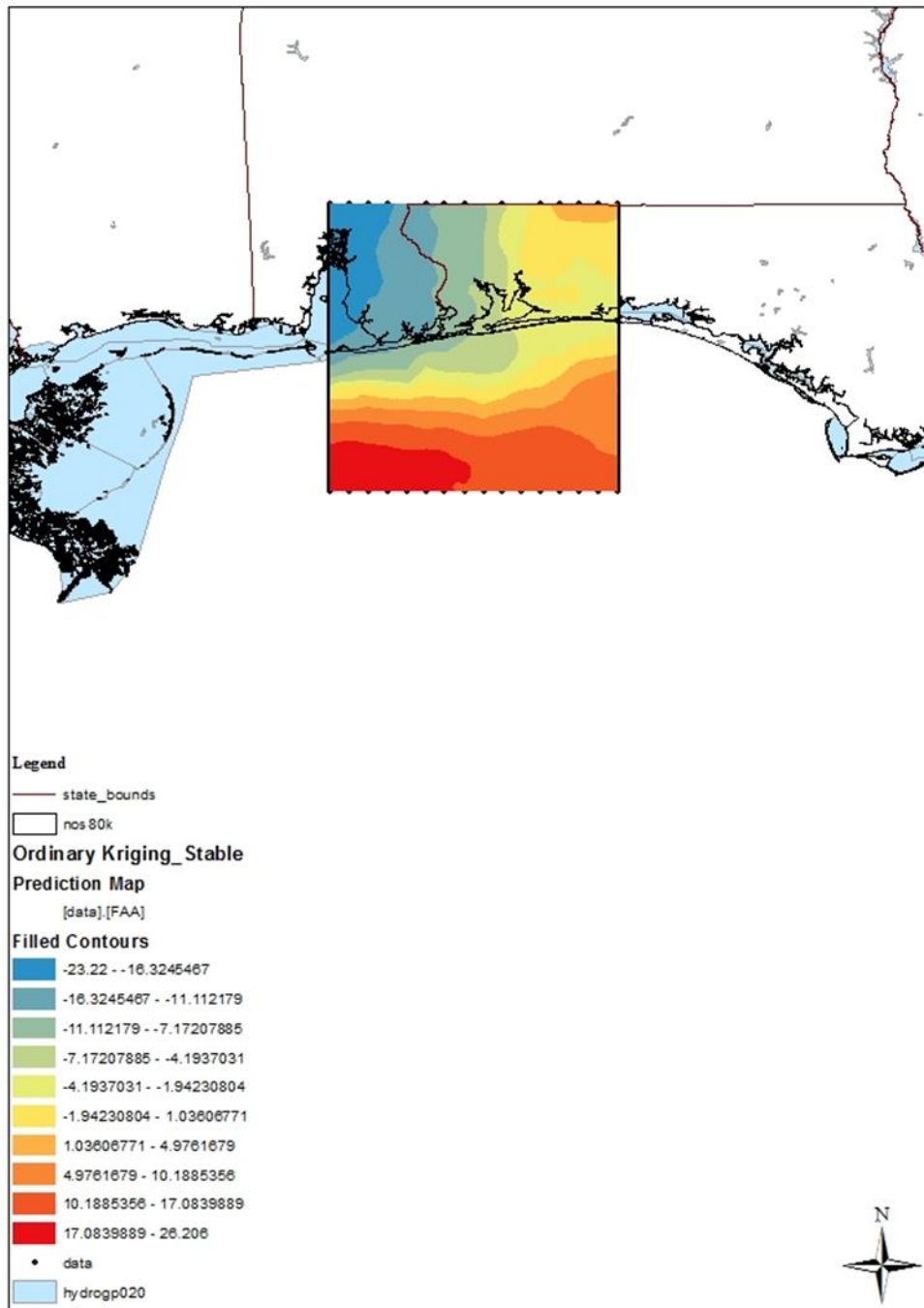


Figure 2.17 The ordinary stable kriging predictions map (unit in mgal).

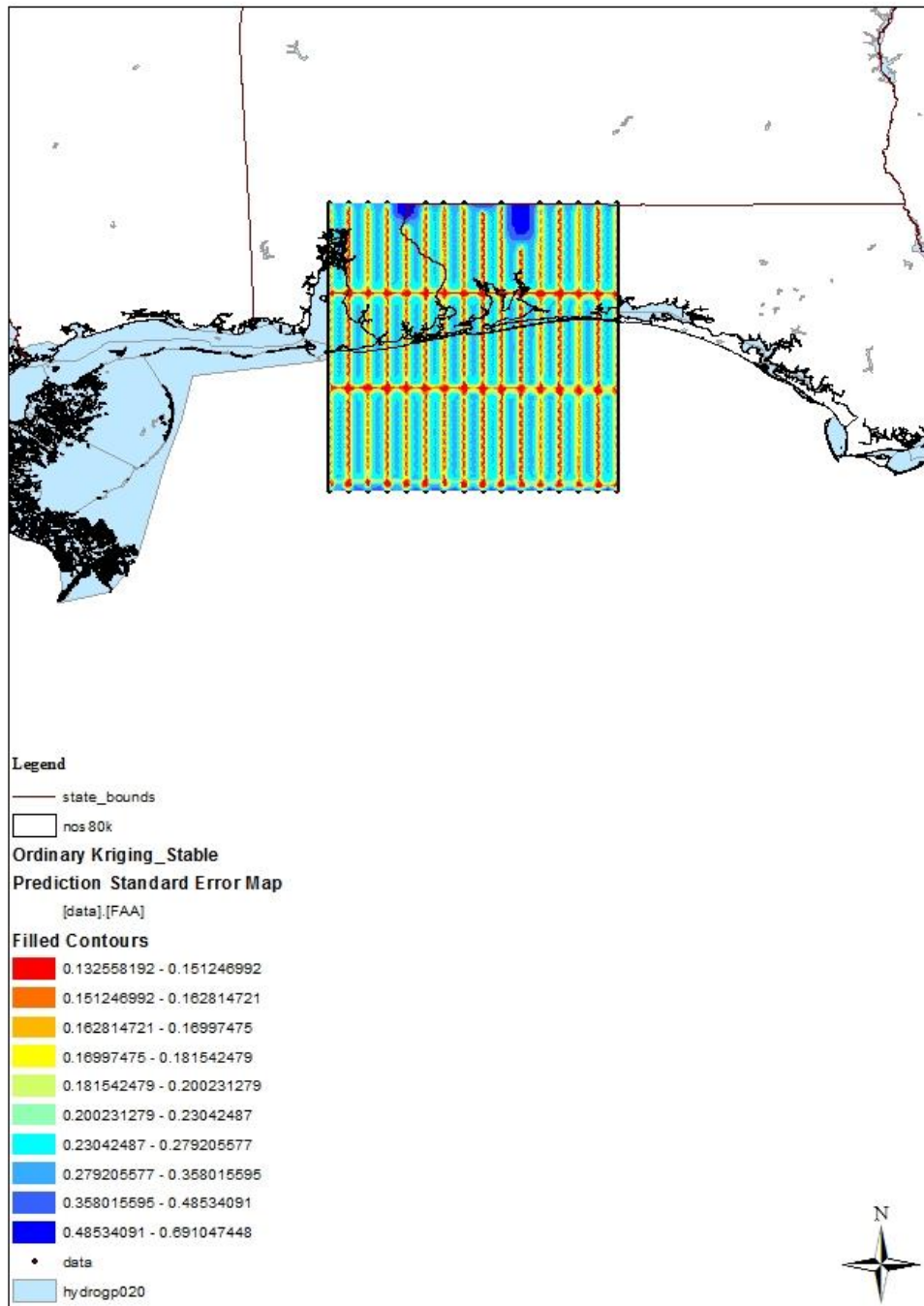


Figure 2.18 The ordinary stable kriging prediction standard error map (unit in mgal).

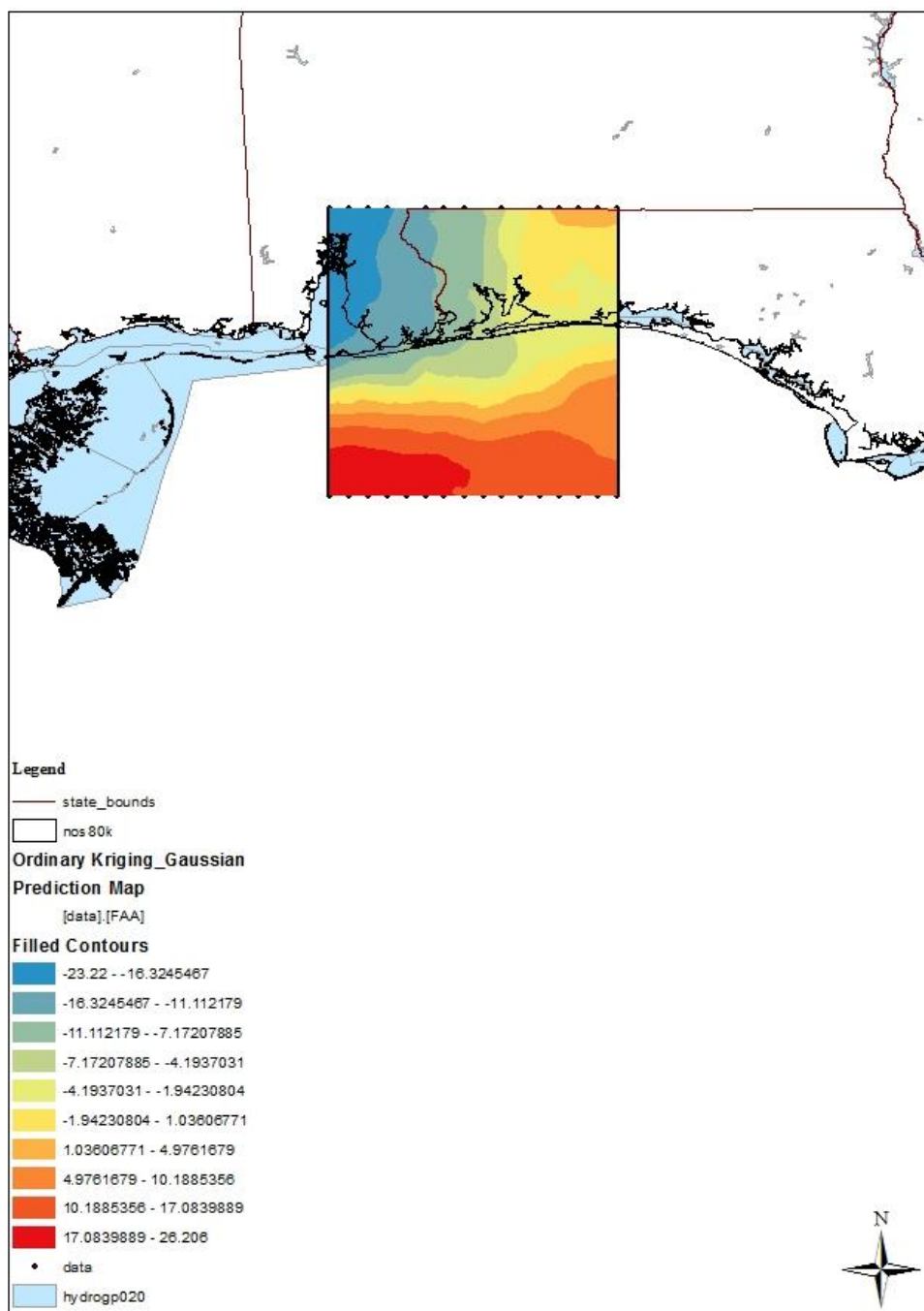


Figure 2.19 The ordinary Gaussian kriging predictions map (unit in mgal).

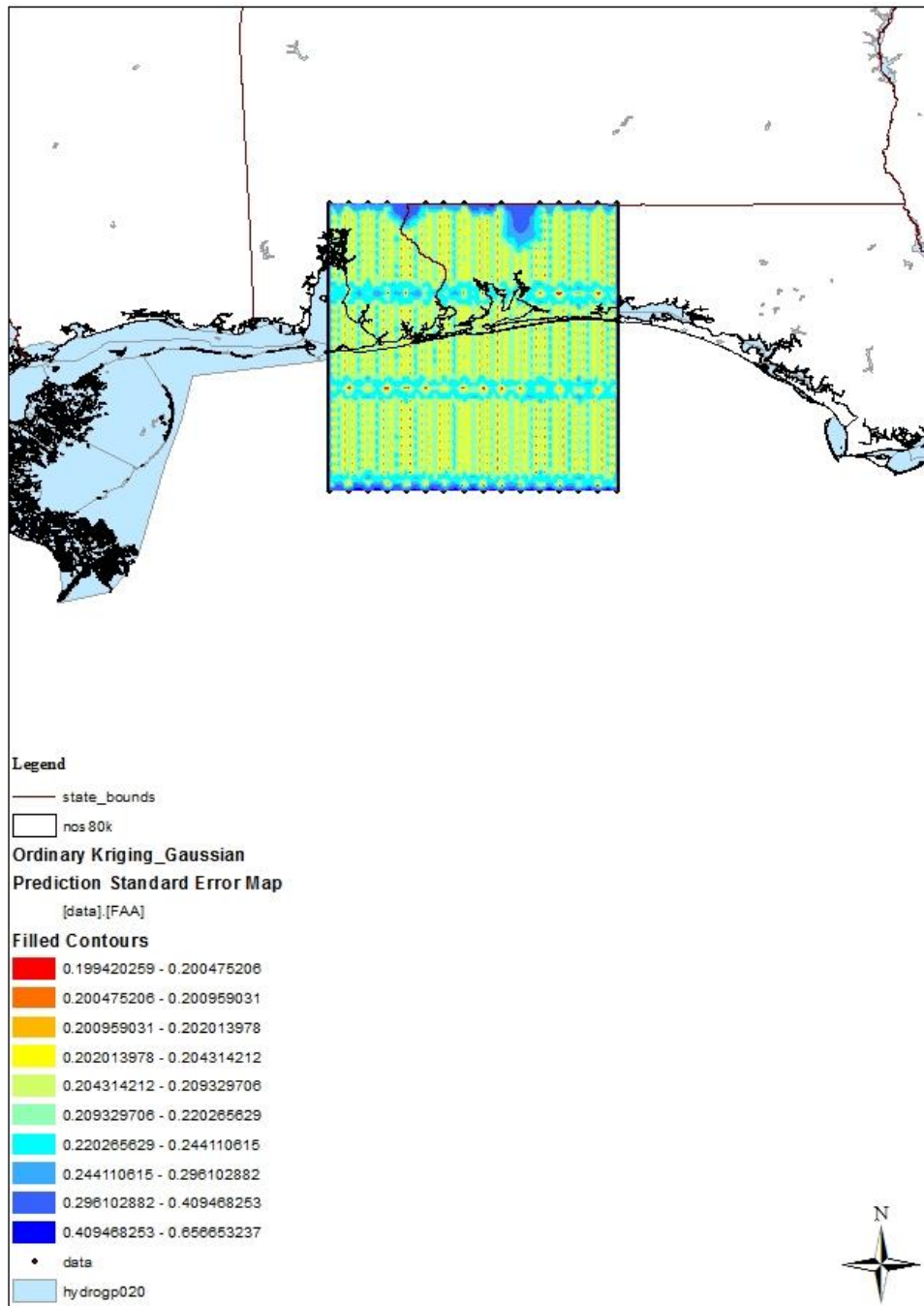


Figure 2.20 The ordinary Gaussian kriging prediction standard error map (unit in mgal).

2.1.2 Universal kriging

Unlike the ordinary kriging method, the universal kriging method assumes that the variation in z value has a trend.

$$z(s) = \mu(s) + \varepsilon(s) \quad (2.9)$$

$$\mu(s) = \beta_1 x_i + \beta_2 y_i \quad \text{or}$$

$$\mu(s) = \beta_0 + \beta_1 x_i + \beta_2 y_i + \beta_3 x_i^2 + \beta_4 x_i y_i + \beta_5 y_i^2 \quad (2.10)$$

In the equation (2.9 & 2.10) shown above, $z(s)$ represents the variable of interest, which is the prediction; the $\mu(s)$ is the deterministic trend; and $\varepsilon(s)$ represents a random error form. s indicates the location. The trend can be a linear function in spatial coordinates, or a 2nd order polynomial trend surface. In the trend equation, $\beta_0, \beta_1, \beta_2, \beta_3, \beta_4,$ and β_5 are coefficients which are unknown; x represents longitude and y indicates latitude.

To find out if there is a global trend in FAA data, trend analysis graph is needed. A global trend describes pattern of variation. Assumption of a constant average across the surface is applied for kriging models. There is no trend exists because the curve through the projected points is flat (as shown by the red line in the Figure 2.21). An upward curve as shown by the light blue line in Figure 2.21 is through the projected points on YZ plane, which indicates that there is a trend in FAA data. Therefore, de-trending is conducted before the universal kriging process in order to prevent biased the analysis. According to the trend analysis, two de-trending approaches were conducted. One approach is to remove the trend order as constant, and the other is to remove the trend as first order. The Kernel function chose to be exponential, which allows a selection of the kernel used to fit the surface (Figures 2.22 and 2.23). The goodness of fit in

removal of constant trend is 11.5802 (Figure 2.22). With removal of first order of the trend (Figure 2.23), the goodness of fit is 5.9941. Therefore, de-trend by removing first order of the trend is much better than removing constant trend. Results in this section will only be provided by removing first order of the trend universal kriging. If interested in results from the universal kriging by using constant trend removed (prediction models 3 and 4), please see Appendix 3.

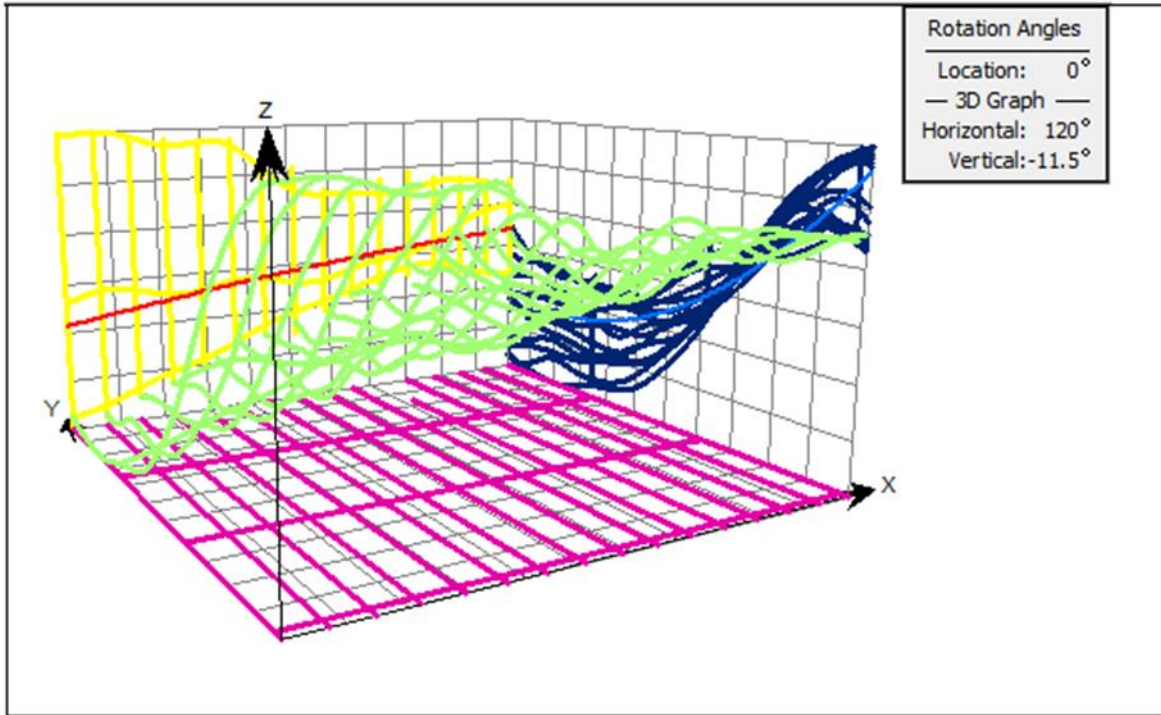


Figure 2.21 Trend analysis of FAA.

Legend: Grid (XYZ): Number of Grid Lines 11×11×6; Projected Data: YZ plane (Dark Blue), ZY plane (Yellow), XY plane (Peony Pink); Trend on Projections: YZ plane (Light Blue), XZ plane (Red); Axes (Black); Input Data Points_FAA (Green).

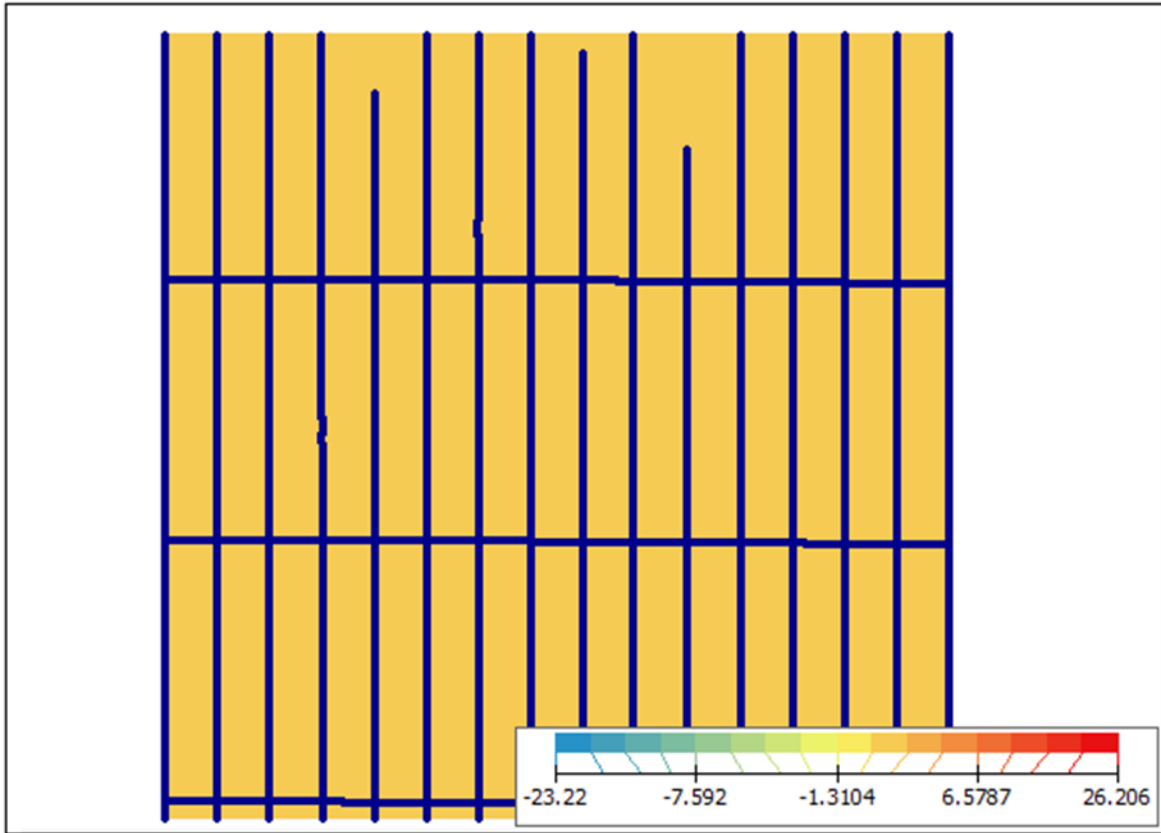


Figure 2.22 De-trend. The order of removal trend is constant (unit in mgal).

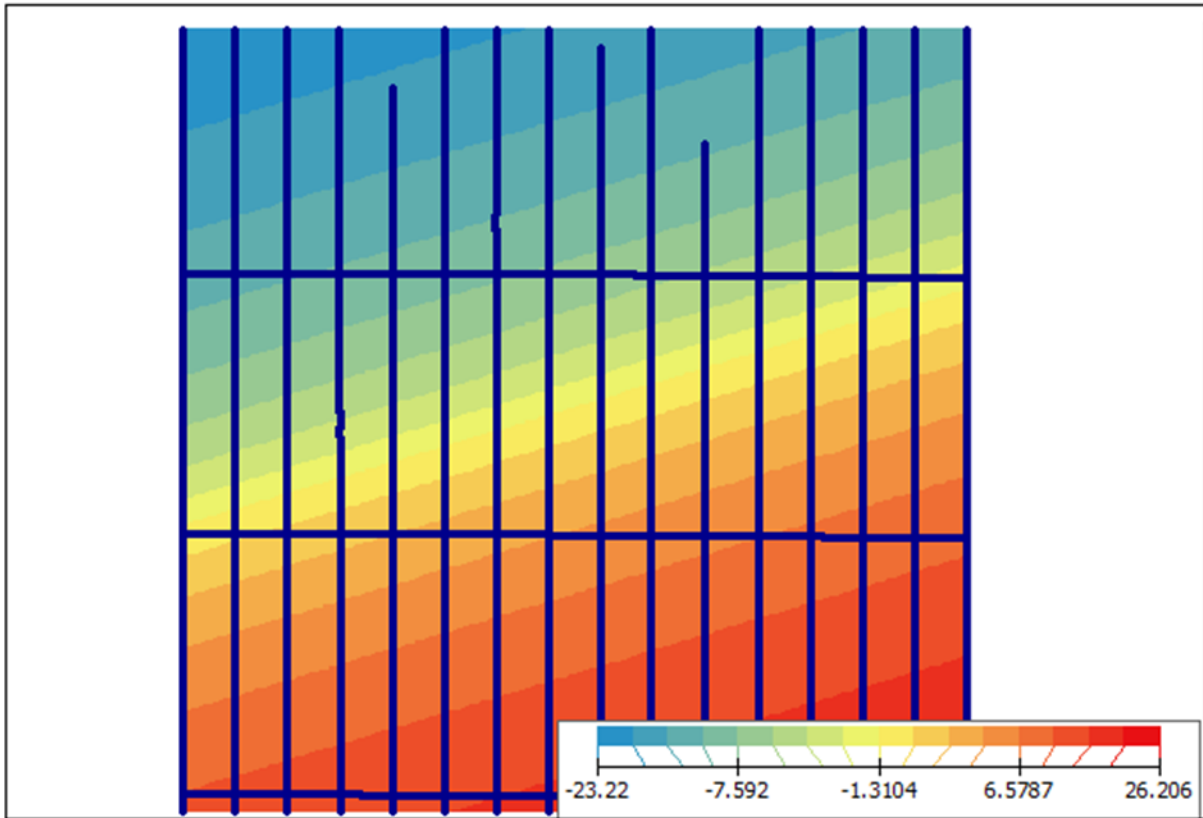


Figure 2.23 De-trend. The order of removal trend is first order (unit in mgal).

Similar processes as the ordinary kriging method is conducted in ArcGIS 10, which are semivariogram modeling, searching neighborhood, and cross validation. The nugget, the range and the partial sill of the semivariogram were compared between the stable technique and the Gaussian technique of the universal kriging with first order of trend removed (see Table 2.2 and Figures 2.24 to 2.31). The semivariogram by using the stable model has smaller independent error than by using the Gaussian model; however, the variation in the semivariogram by using the stable model is a little bit bigger than by using the Gaussian model. By direct visual comparison of graphs (Figures 2.24 to 2.29), the model “perfect” fit through the averaged binned values at the distance h .

Type	Nugget	Range	Partial Sill	Sill
Stable	0.2341	0.9575	49.9359	50.1700
Gaussian	0.3788	0.9059	48.9174	49.2962

Table 2.2 Comparison of the components of stable and Gaussian semivariogram (units of nugget, partial sill and sill are mgal^2 ; unit of range is degree).

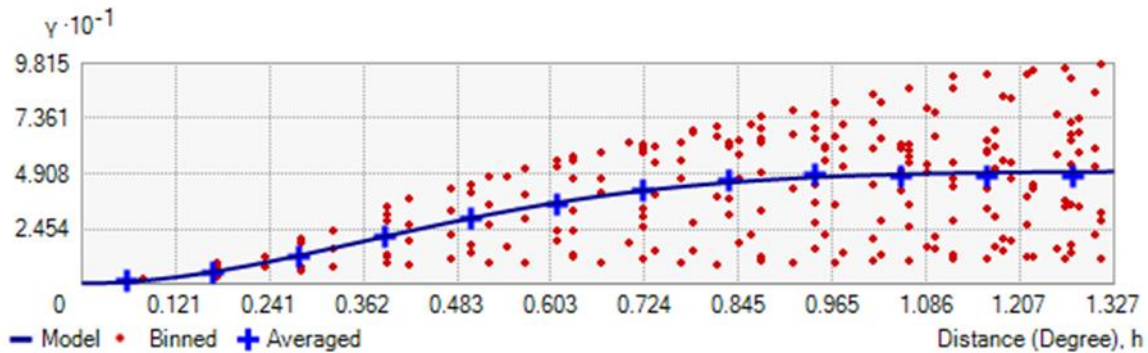


Figure 2.24 Semivariogram of the universal stable kriging with removal of 1st order of trend. The averaged semivariogram values on the y-axis (in mgal^2), and distance (or lag) on the x-axis (in degree). Binned values are shown as red dots, which are sorted the relative values between points based on their distances and directions and computed a value by square of the difference between the original values of points; Average values are shown as blue crosses, which are generated by binning semivariogram points; The model is shown as blue curve, which is fitted to average values. Model: $0.23412 \cdot \text{Nugget} + 49.936 \cdot \text{Stable}(0.95752, 1.9033)$.

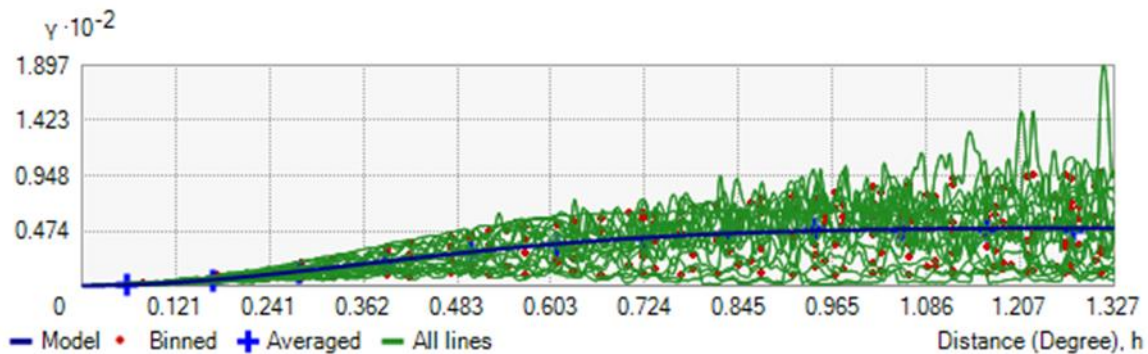


Figure 2.25 Semivariogram with all lines (green lines) which fit binned semivariogram values. The averaged semivariogram values on the y-axis (in mgal^2), and distance (or lag) on the x-axis (in degree).

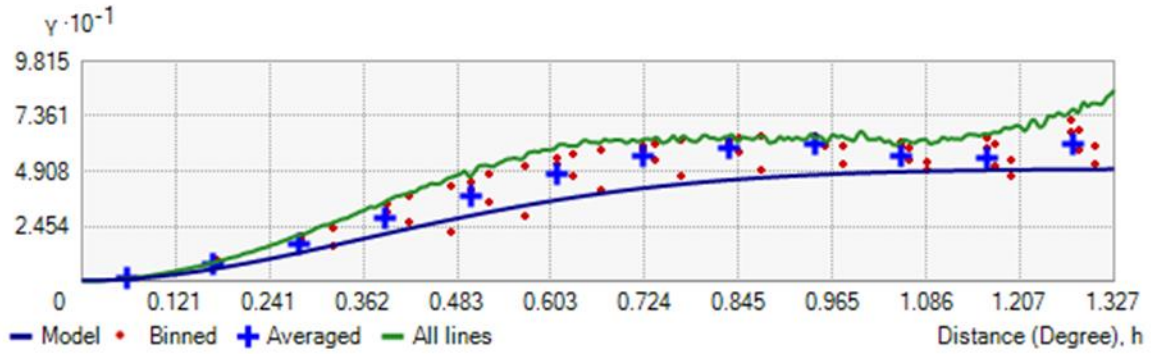


Figure 2.26 Semivariogram with showing search direction. The tolerance is 45 and the bandwidth (lags) is 3. The local polynomial shown as a green line fits the semivariogram surface in this case. The averaged semivariogram values on the y-axis (in mgal^2), and distance (or lag) on the x-axis (in degree).

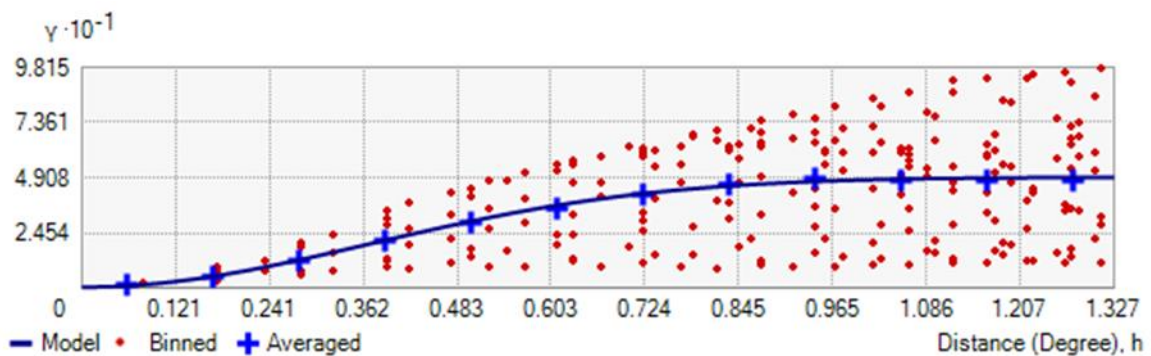


Figure 2.27 Semivariogram of the universal Gaussian kriging with removal of 1st order of trend. The averaged semivariogram values on the y-axis (in mgal^2), and distance (or lag) on the x-axis (in degree). Binned values are shown as red dots, which are sorted the relative values between points based on their distances and directions and computed a value by square of the difference between the original values of points; Average values are shown as blue crosses, which are generated by binning semivariogram points; The model is shown as blue curve, which is fitted to average values. Model: $0.37882 \cdot \text{Nugget} + 48.917 \cdot \text{Gaussian}(0.90587)$.

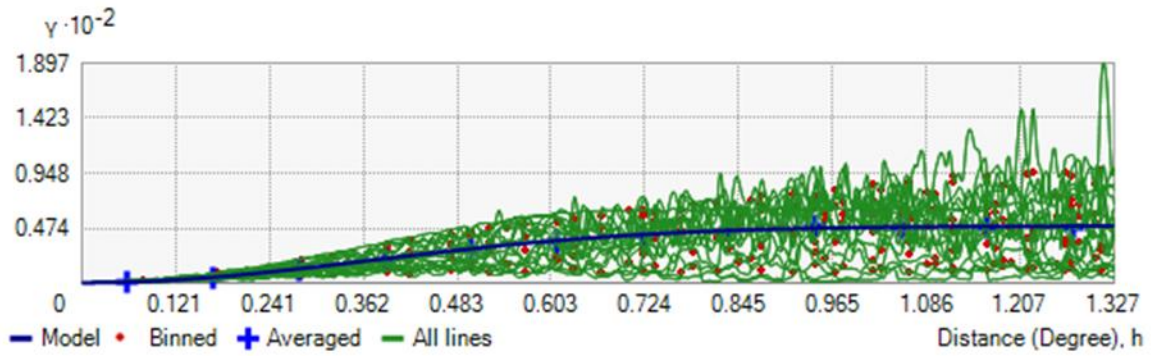


Figure 2.28 Semivariogram with all lines (green lines) which fit binned semivariogram values. The averaged semivariogram values on the y-axis (in mgal^2), and distance (or lag) on the x-axis (in degree).

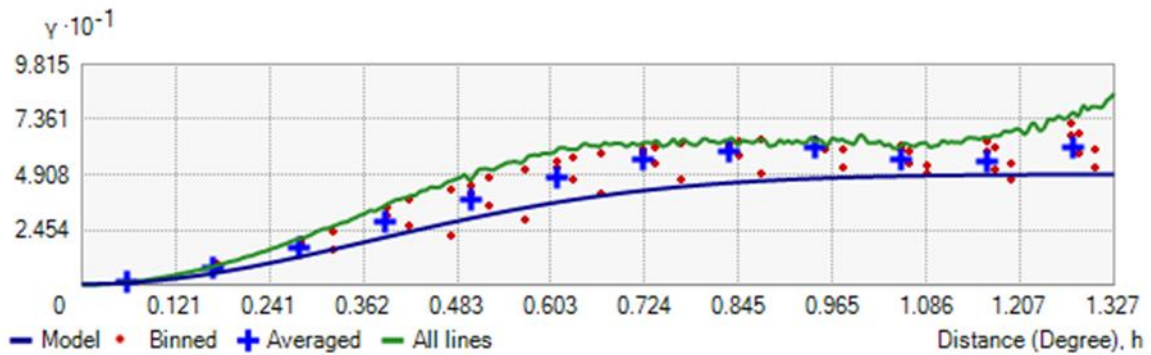


Figure 2.29 Semivariogram with showing search direction. The tolerance is 45 and the bandwidth (lags) is 3. The local polynomial shown as a green line fits the semivariogram surface in this case. The averaged semivariogram values on the y-axis (in mgal^2), and distance (or lag) on the x-axis (in degree).

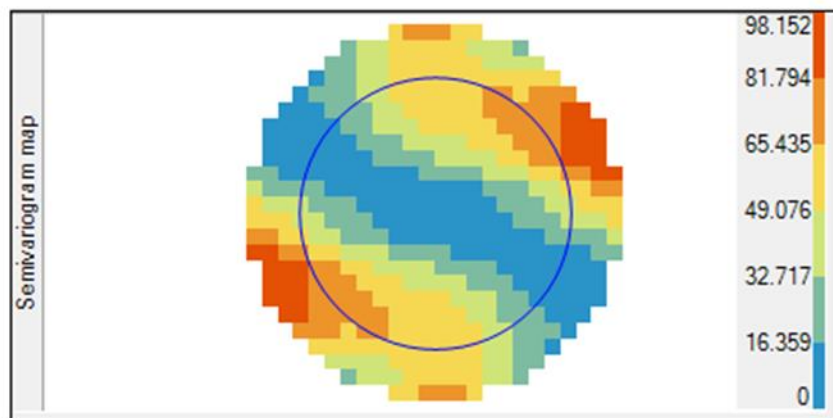


Figure 2.30 A semivariogram map. The color band shows semivariogram values with weights (unit in mgal^2).

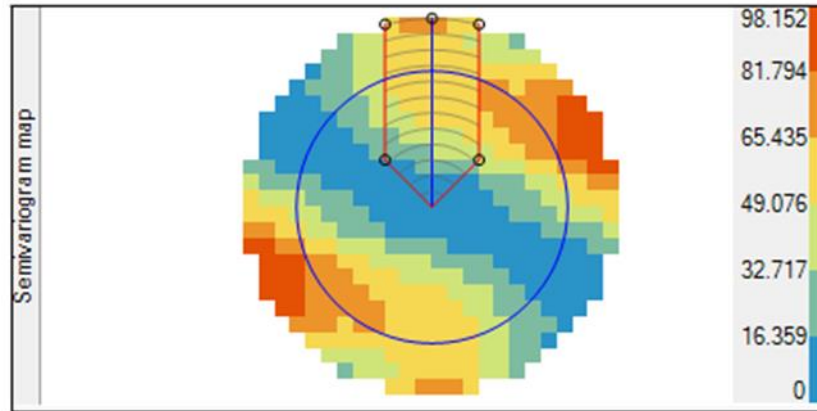


Figure 2.31 A semivariogram map with an example search direction transects (unit in mgal^2).

Searching neighborhood made use of the Geostatistical Analyst tool in ArcGIS 10 software. The default of searching neighborhood was chosen, which is by using standard neighborhood searching type, neighbors range from 2 to 5, and the search sector type is 4 sectors with 45° offset. The example of searching neighborhood displayed in Figure 2.32.

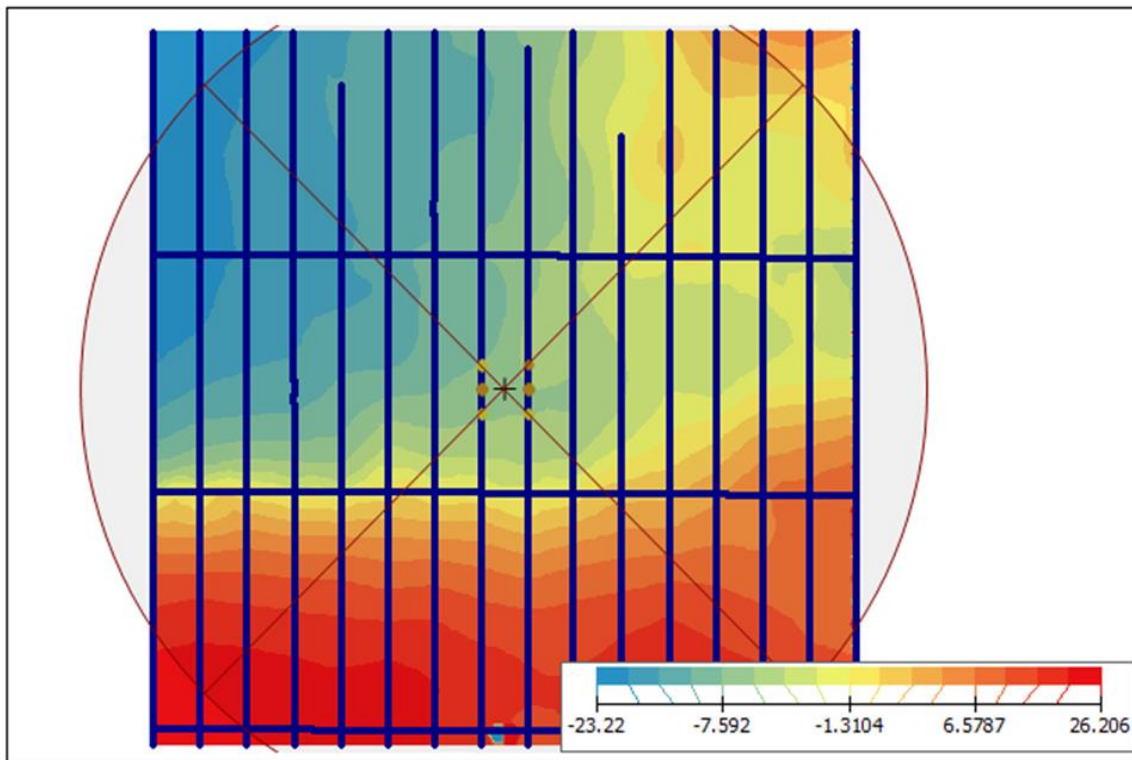
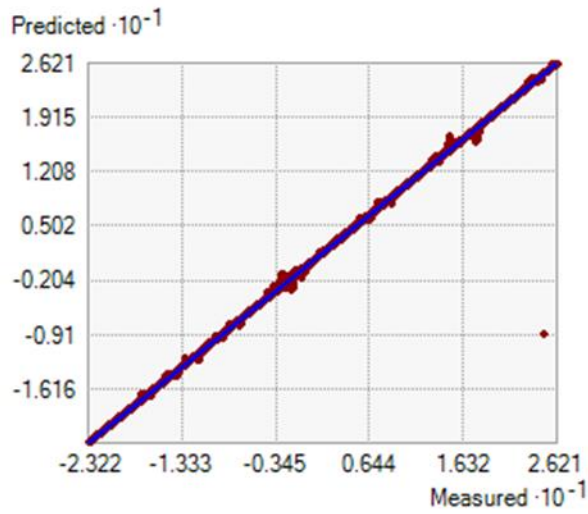


Figure 2.32 An example of searching neighborhood by using the Geostatistical Analyst Tool in ArcGIS 10. Legend is FAA intervals in color band (unit in mgal).

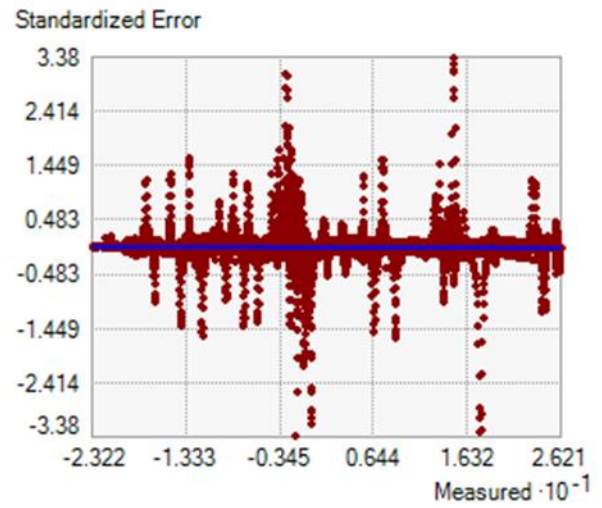
The cross validation statistics of the universal kriging method with first order of trend removed shows in Table 2.3, below. The prediction model using the stable technique is better than the prediction using the Gaussian technique.

Cross-validation statistics	Prediction Model 5	Prediction Model 6
	U.K. 1st-Stable	U.K. 1st-Gaussian
RMS Standardized	0.2058	0.2214
Mean Standardized	-0.0025	-0.0061
Average Standard Error (ASE)	0.5070	0.6426
Root Mean Square (RMS)	0.1028	0.1412
Difference between RMS and ASE	0.4042	0.5014
Difference in Percentage	79.72%	78.03%

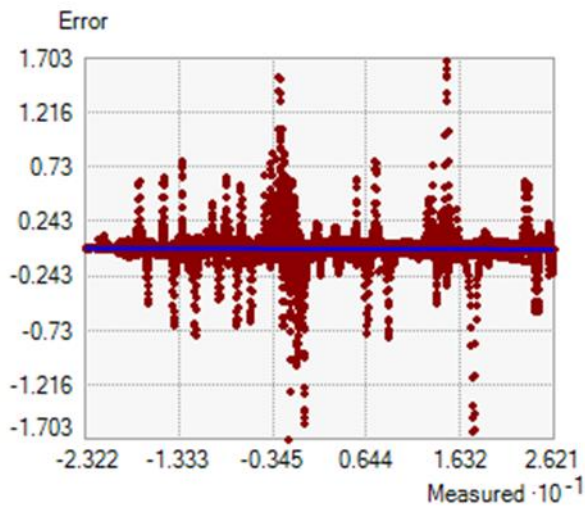
Table 2.3 Cross validation statistics compared between the stable and the Gaussian techniques (unit in mgal).



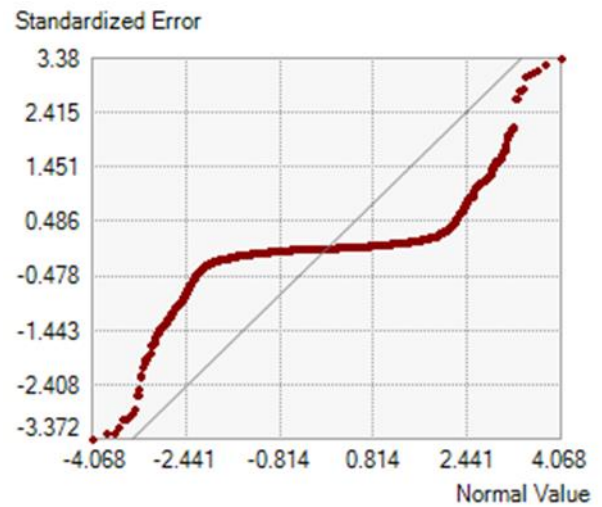
A.



C.

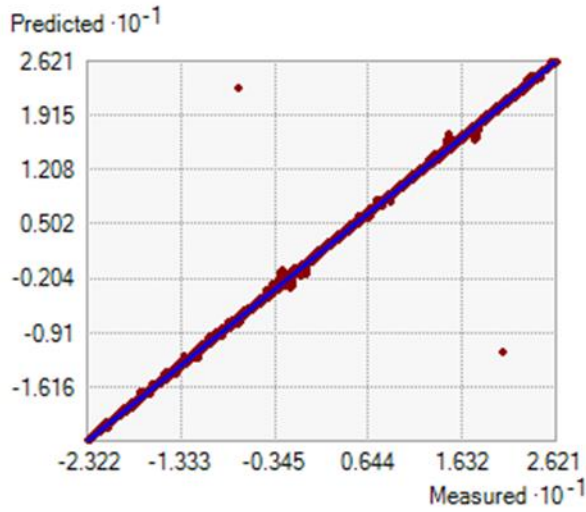


B.

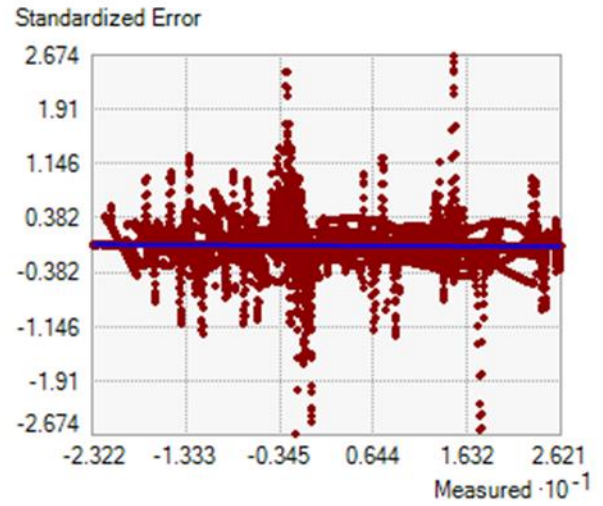


D.

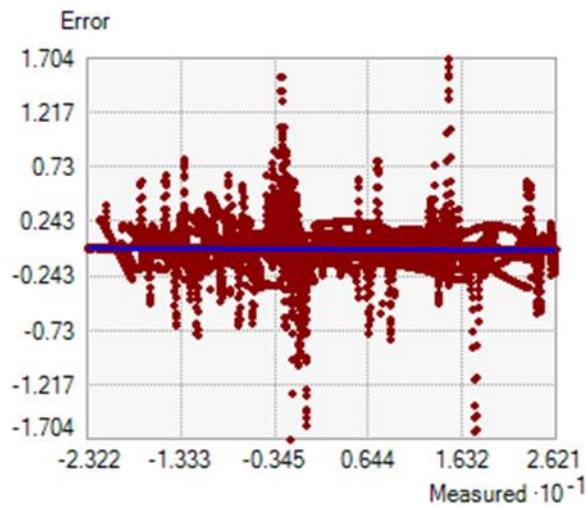
Figure 2.33 Cross validation of the universal stable kriging with 1st order of trend removed (unit in mgal).



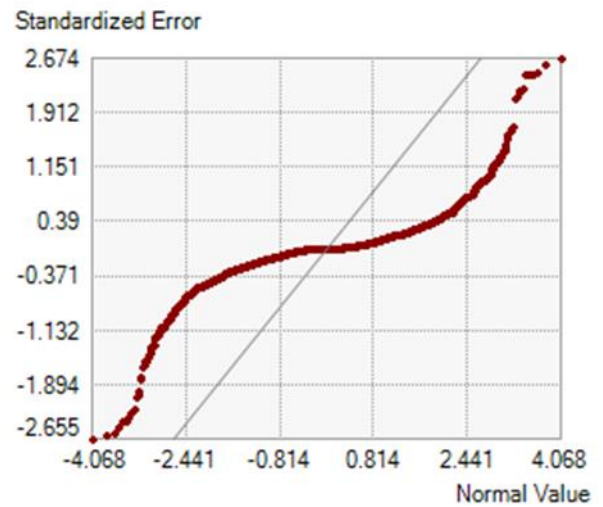
A.



C.



B.



D.

Figure 2.34 Cross validation of the universal Gaussian kriging with 1st order of trend removed (unit in mgal).

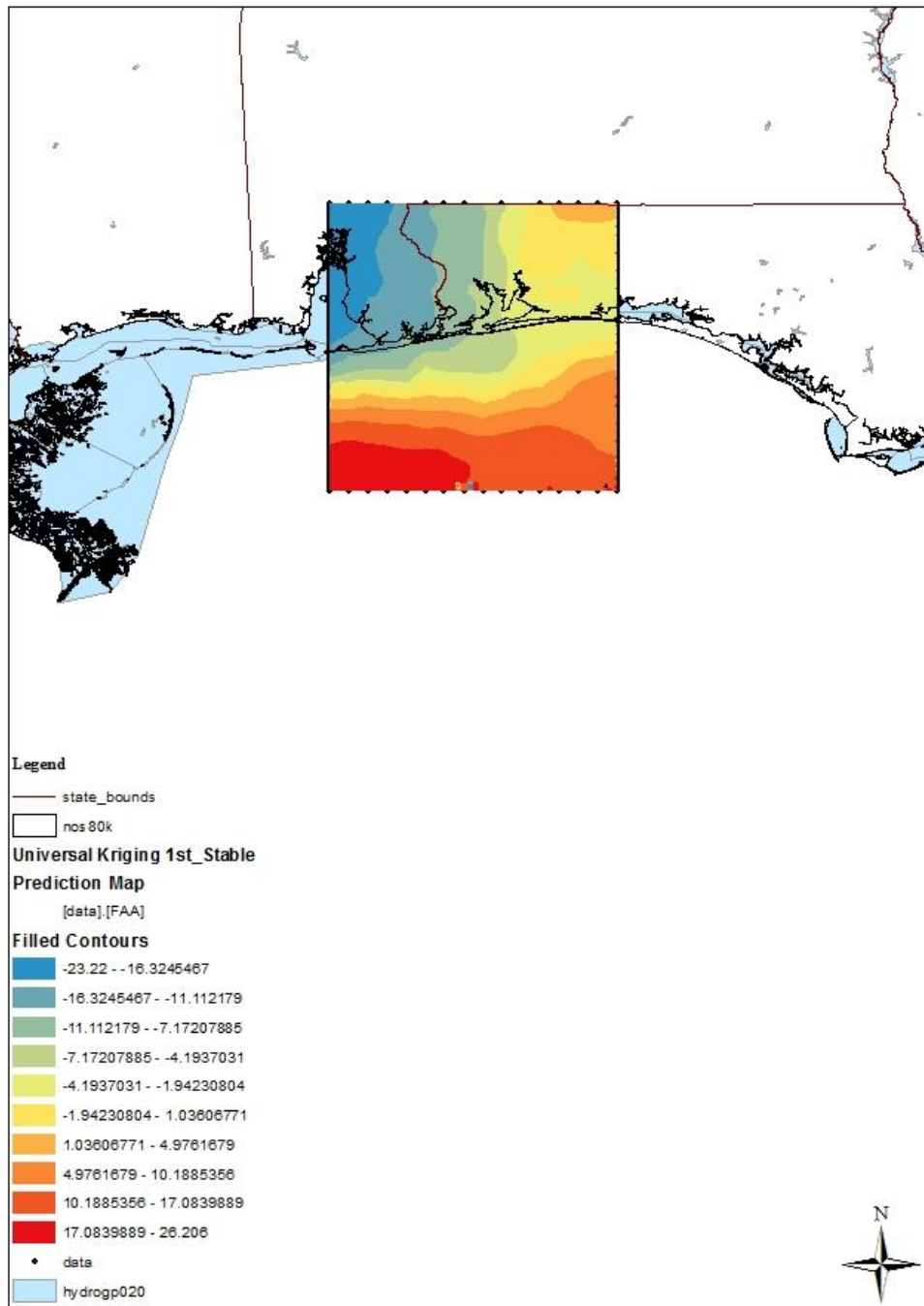


Figure 2.35 The universal stable kriging predictions map (unit in mgal).

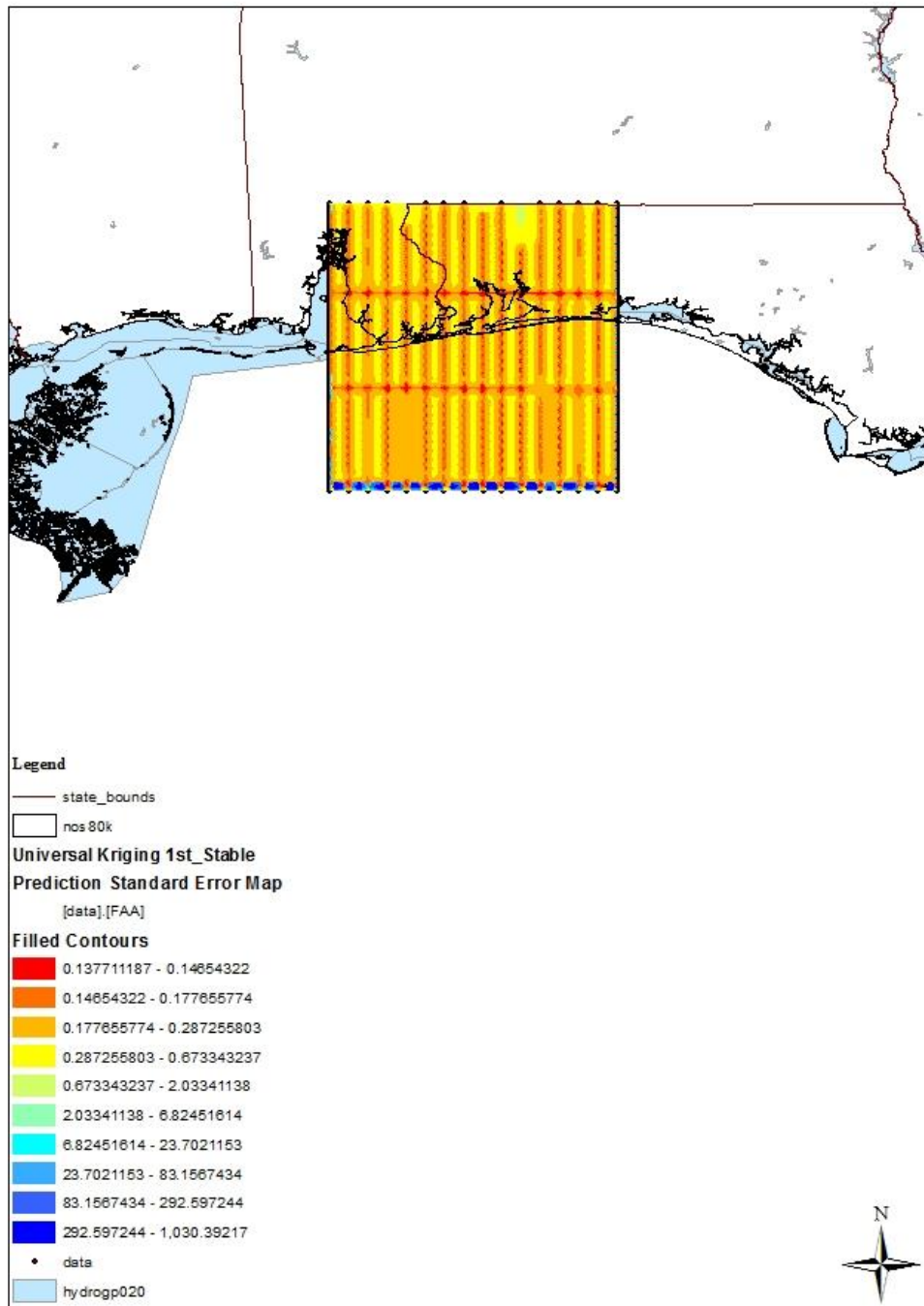


Figure 2.36 The universal stable kriging prediction standard error map (unit in mgal).

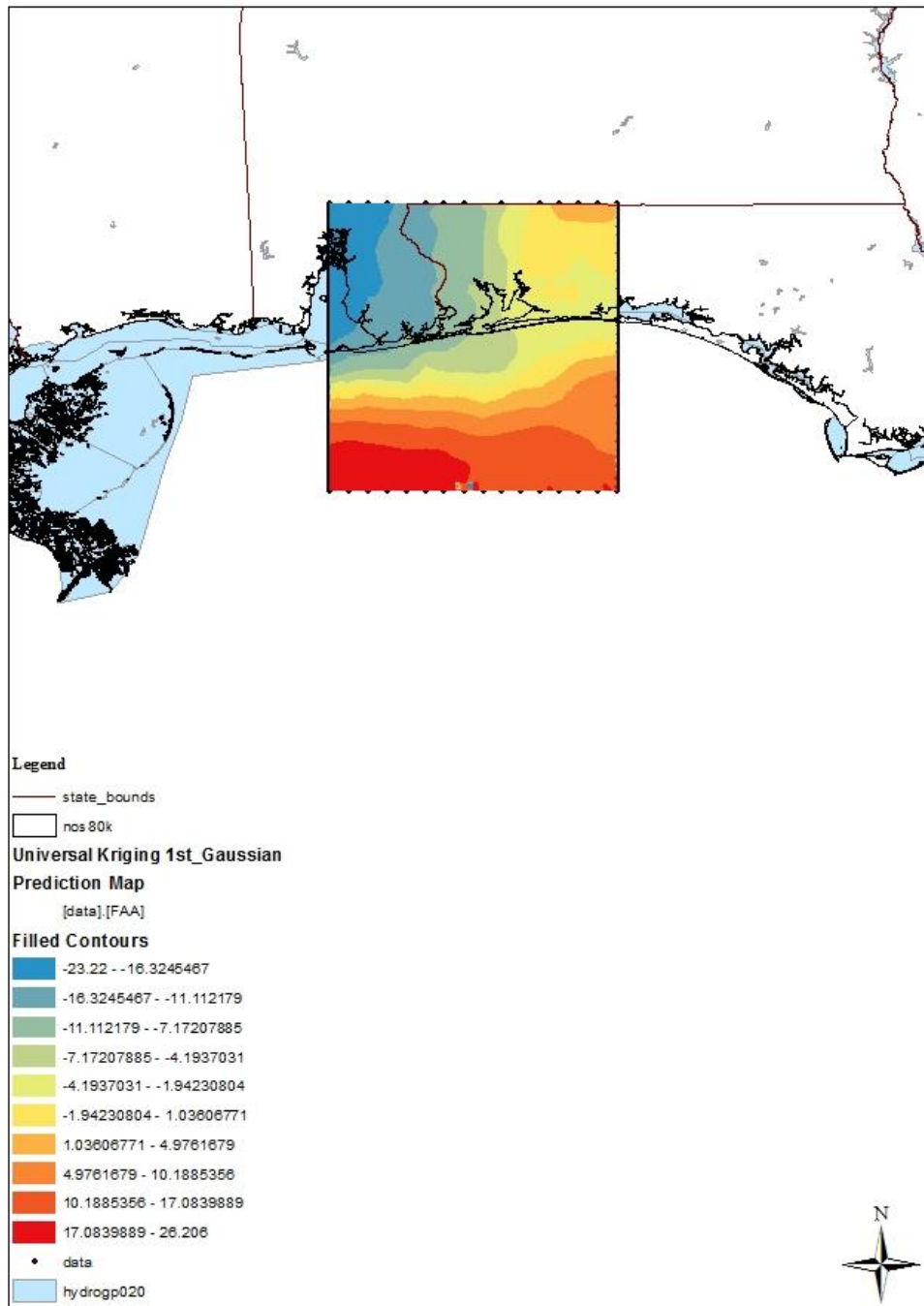


Figure 2.37 The universal Gaussian kriging prediction map (unit in mgal).

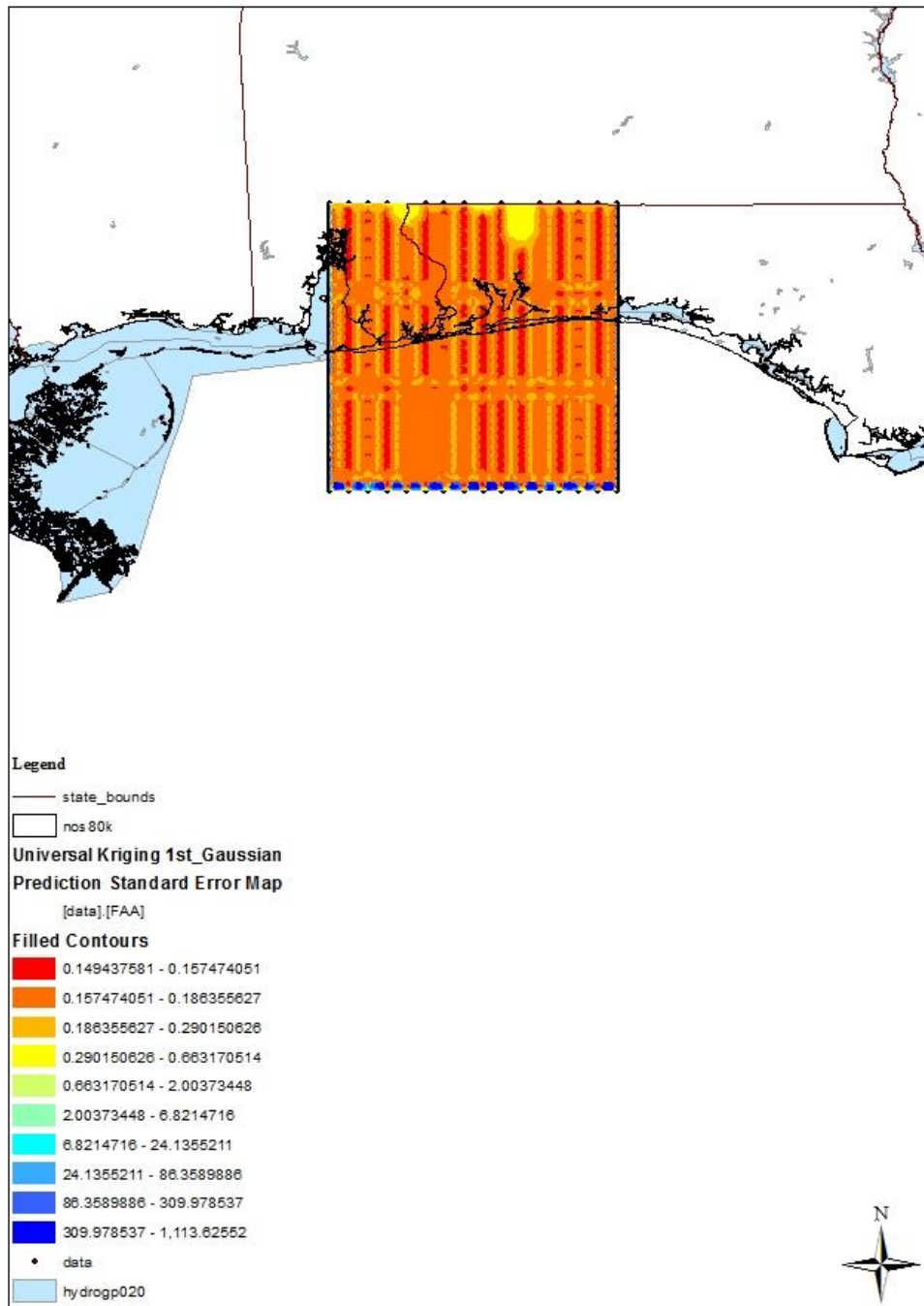


Figure 2.38 The universal Gaussian kriging prediction standard error map (unit in mgal).

2.2 Inverse distance weighted (IDW) interpolation

The assumption of IDW interpolation is also based on the First Law of Geography (Tobler 1970), and there is no assumption required of the data. The IDW interpolation estimates a value of a point by using a linear weighted combination of the sample points. The general formula for IDW interpolation is:

$$z_s = \frac{\sum_{i=1}^n z_i \frac{1}{d_i^p}}{\sum_{i=1}^n \frac{1}{d_i^p}} \quad (2.11)$$

where z_s is the estimated value at point s ; z_i is the known value at the control point i ; n is the number of known sample points used in the estimation; d_i is the distance between point s and point i ; p is the specified power which controls the degree of the local influence.

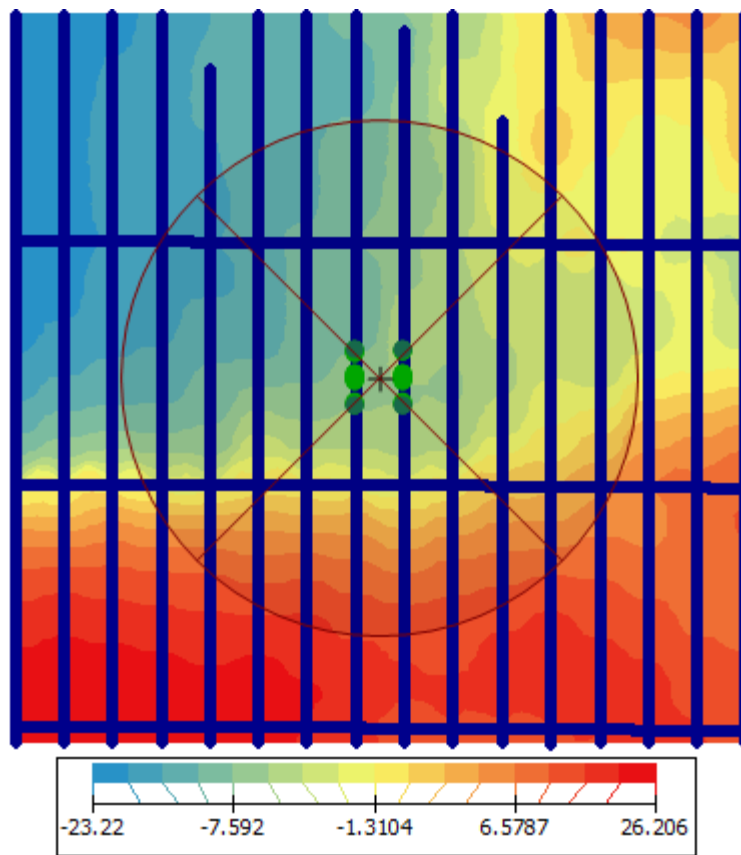
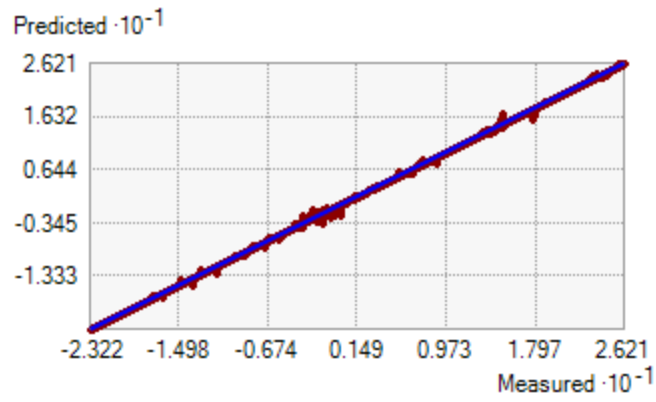
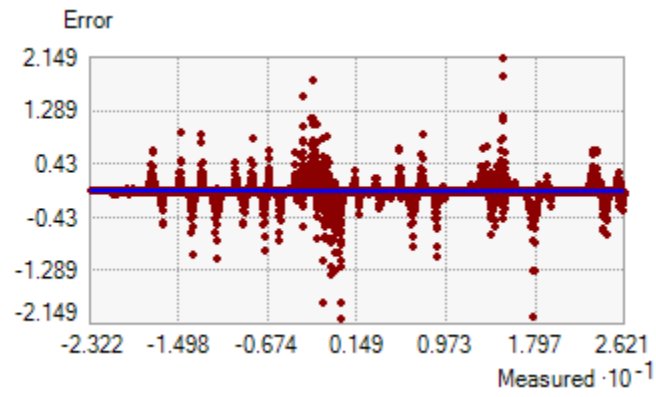


Figure 2.39 An example of IDW searching neighborhood by using the Geostatistical Analyst Tool in ArcGIS 10. Legend is FAA intervals in color band (unit in mgal).

IDW interpolation was conducted by the Geostatistical Analyst tool in ArcGIS 10 software. The power set as 2, which suggests that the rate of change in values is influenced by distance (a higher value near a known point). By using standard searching neighborhood type, search by a 4 sectors with 45° offset. The neighbors range from 10 to 15. An example provided in Figure 2.39. The RMS is 0.0817, which is lower than the kriging method. The regression function in predicted graph (Figure 2.40A) is $f(x) = 0.9999x + 0.00004$; the error in this regression is too small to even ignore it. The regression function in error graph (Figure 2.40B) is $f(x) = 0.0001x + 0.00004$. So far, IDW interpolation is better than either the ordinary kriging method or the universal kriging method. But unfortunately, IDW interpolation has no evaluation of predicted standard error, which may be tricky to demonstrate the use of the model. The predicted continuous map of FAA by using IDW interpolation is shown in Figure 2.41.



A.



B.

Figure 2.40 Cross validation of IDW (unit in mgal).

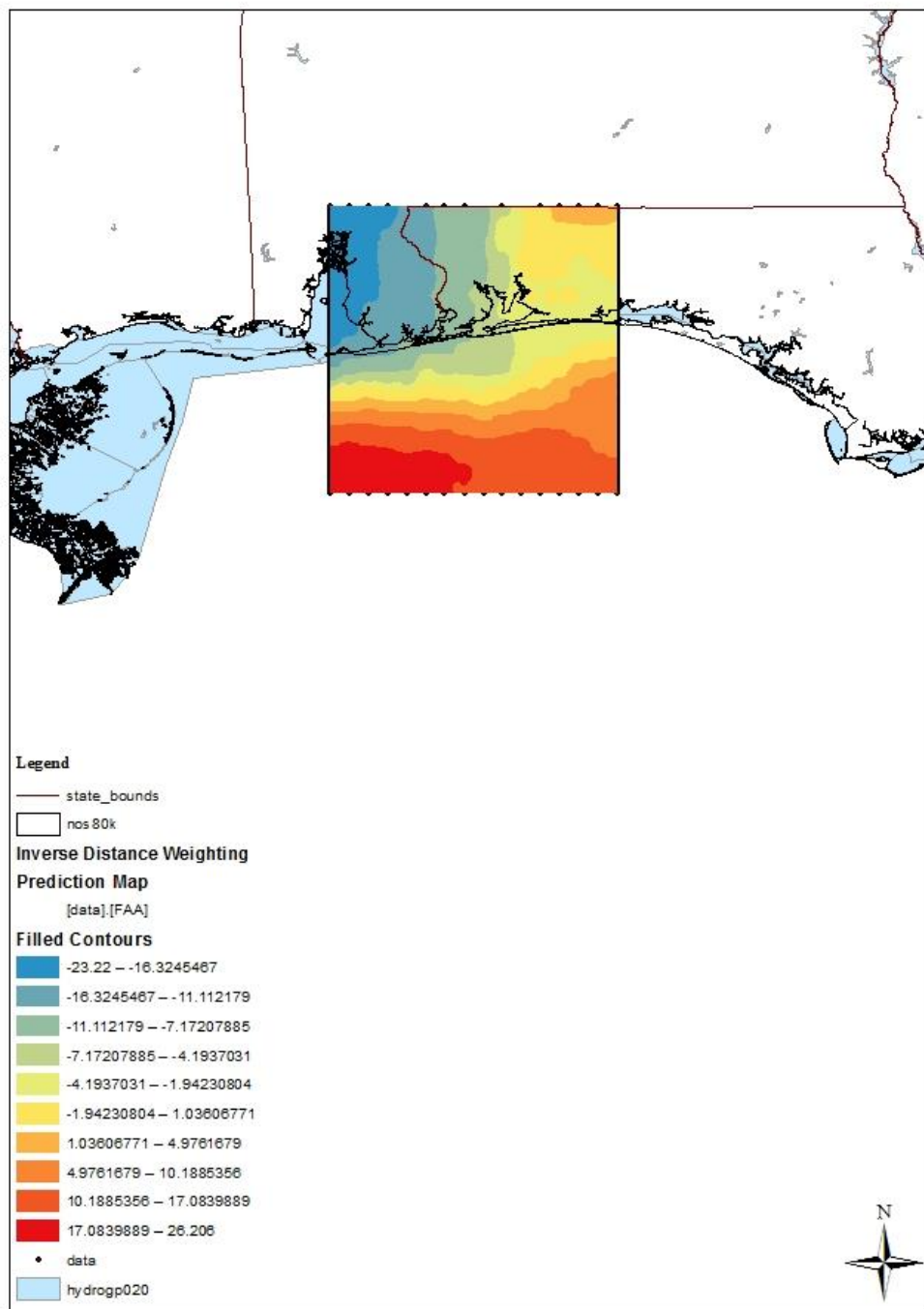


Figure 2.41 The IDW prediction map (unit in mgal).

2.3 FAA applied to geoid undulation and evaluates errors

It is well known that free air anomalies are not correlated with heights in flat regions, and therefore we can determine Geoid undulations $N(x, y)$ at measured points (x, y) in the area A by using FFT (Fast Fourier Transform) to Kearsley two-dimensional convolution integral

$$N(x_p, y_p) = \frac{1}{2\pi\gamma} \iint_A \frac{\Delta g(x, y)}{\sqrt{(x_p - x)^2 + (y_p - y)^2}} dx dy$$

In discrete case we use $K \times L$ gridded point gravity anomalies with spacing Δx and Δy then the Geoid undulation at the point (x_k, y_l) could be found by using the following discrete convolution of Kearsley integral:

$$N(x_k, y_l) = \frac{1}{2\pi\gamma} \sum_{i=0}^{K-1} \sum_{j=0}^{L-1} \Delta g(x_i, y_j) I_N(x_k - x_i, y_l - y_j) \Delta x \Delta y$$

where

$$I_N(x_k - x_i, y_l - y_j) = \begin{cases} \frac{1}{\sqrt{(x_k - x_i)^2 + (y_l - y_j)^2}} & , x_k \neq x_i \text{ or } y_l \neq y_j \\ 0 & x_k = x_i \text{ and } y_l = y_j \end{cases}$$

And the contribution at the computation point (x_k, y_l) should be evaluated as follows:

$$\delta N(x_k, y_l) = \frac{\sqrt{\Delta x \Delta y}}{\gamma \sqrt{\pi}} \Delta g(x_k, y_l)$$

Now we can estimate errors corresponding this way of finding geoid undulations. If we assume that $\Delta x = \Delta y = 1$, and that the maximum absolute errors cannot exceed some $\varepsilon > 0$ then for any point (x_k, y_l) maximum absolute error E of undulation $N(x_k, y_l)$ will be less than

$$E < \varepsilon + \varepsilon \sum_{i=1}^K \sum_{j=1}^L \frac{1}{i} \frac{1}{j} < \varepsilon + \varepsilon \ln K \ln L$$

The last inequality can be obtained through evaluation of double sum by the way of double integration over the rectangle region of the plane between 1 and K for x and 1 and L with respect to y .

2.4 Acknowledgements

FAA data was shared by Dr. Alexey Sadovski on September 17, 2009, and he received this data from Daniel B. Prouty at Conrad Blucher Institute at TAMUCC on March 2, 2007. Other file data used in the map (named as nos80k, state_bounds, hydrogp020) was download from USGS.

2.5 References

- Cressie, N. (1990). The origins of kriging. *Mathematical Geology*, 22 (3), 239-252.
- Delhomme, J. P. (1978). Kriging in the hydrosiences. *Advances in water resources*, 1 (5), 251-266.
- ESRI. *3D analysis of surfaces and features using ArcGIS 10*. Accessed November 29, 2012, from: <http://training.esri.com>.
- ESRI. *Performing spatial interpolation using ArcGIS 10*. Accessed March 26, 2012, from: <http://training.esri.com>.
- ESRI. *Fitting a model to the empirical semivariogram*. Accessed January 28, 2013, from ArcGIS 10 Help Library.

ESRI. *Semivariogram and covariance functions*. Accessed January 28, 2013, from ArcGIS 10 Help Library.

ESRI. *Understanding transformations and trends*. Accessed February 25, 2013, from ArcGIS 10 Help Library.

HYDROGP020 - U.S. National Atlas Water Feature Areas: bays, glaciers, lakes and swamps.

(2003). *U.S. Geological Survey*. Accessed January 19, 2012. Available from:

<http://coastalmap.marine.usgs.gov/GISdata/basemaps/usa/water/hydrogp020.zip>.

Journel, A. G., & Rossi, M. E. (1989). When do we need a trend model in kriging?.

Mathematical Geology, 21 (7), 715-739.

NOS80K - Medium Resolution Digital Vector U.S. Shoreline shapefile for the contiguous United

States. (1994). *National Oceanic and Atmospheric Administration (NOAA), National*

Ocean Service (NOS), Office of Coast Survey, and the Strategic Environmental

Assessments (SEA) Division of the Office of Ocean Resources Conservation and

Assessment (ORCA). Accessed January 19, 2012. Available from:

<http://coastalmap.marine.usgs.gov/GISdata/basemaps/coastlines/nos80k/nos80k.zip>.

Reguzzoni, M., Sanso, F., & Venuti, G. (2005). The theory of general kriging, with applications

to the determination of a local geoid. *Geophysical Journal International*, 162 (2), 303-

314.

Sakata, S., & Ashida, F. (2011). Integral estimation with the ordinary kriging method using the

Gaussian semivariogram function. *International journal for Numerical Methods in*

Biomedical Engineering, 27 (8), 1235-1251.

Schmitz, G. H., Kiefer, E. M., & Vauclin, M. (1990). Modern kriging and classical Gaussian techniques—Do they necessarily yield identical results. *Advances in water resources*, 13 (2), 90-97.

STATE_BOUNDS: internal US state boundaries. *Valerie Paskevich*. Accessed January 19, 2012.

Available from:

[http://coastalmap.marine.usgs.gov/GISdata/basemaps/boundaries/state_bounds/state_bou
nds.zip](http://coastalmap.marine.usgs.gov/GISdata/basemaps/boundaries/state_bounds/state_bou
nds.zip).

Tobler, W. R. (1970). A computer movie simulating urban growth in the Detroit region.

Economic geography, 46, 234-240.

Webster, R., & Burgess, T. M. (1983). Spatial variation in soil and the role of kriging.

Agricultural water management, 6 (2-3), 111-122.

Wong, D. W., Yuan, L., & Perlin, S. A. (2004). Comparison of spatial interpolation methods for

the estimation of air quality data. *Journal of Exposure Science and Environmental*

Epidemiology, 14 (5), 404-415.

Zhang, K., & Featherstone, W. E. (2004). Investigation of the roughness of the Australian

gravity field using statistical, graphical, fractal and Fourier power spectrum techniques.

Survey Review, 37 (293), 520-530.

Chapter 3: Kriging of Absolute Gravity Data

By using satellites, scientists discovered the long wave (large scale) geoid for the Earth (Seeber, 2003; Drinkwater et al., 2003), but its resolution is not sufficient for orthometric height determination from GPS when it comes to the relatively small scale and/or local events such as flooding. So, there is a need to develop method(s) and model(s) of the geoid determination at the local level, based on local observations of gravity, and complemented by observations of gravity from the air and space.

In principle, there is a need for gravity g at every point of the Earth's surface. Gravity is continuously changing, and it reflects the results of Earth's phenomena, such as tropic storm, hurricane, earthquake, early tides, variation in the atmosphere density, etc. Gravity also alters when only a small change happened in the constructions and the density of materials beneath the constructions. But having gravity data provided everywhere on the Earth is totally impossible in reality. To predict values of a random unsampled area from a set of observations is needed. As chapter 2 mentioned, the kriging method is not the best approach to predict free-air gravity anomalies, but in this chapter, I assumed that the kriging method is a better approach than other methods for prediction of gravity based on the airborne data provided by National Geodetic Survey (NGS). The reason I still have a confidence on the kriging method is that the kriging method can estimate the prediction error to assess the quality of a prediction, which other methods do not have.

3.1 Data

Data used in this chapter is airborne gravity data of the Gravity for the Redefinition of the American Vertical Datum (GRAV-D) project which was released by NGS

(<http://www.ngs.noaa.gov/GRAV-D>). Table 3.1 lists the nominal block characteristics, and details can be found in *GRAV-D General Airborne Gravity Data User Manual*. Four blocks (Block CS01, CS02, CS03 and CS04) data (Figures 3.1 and 3.2) were chosen to be interpolated (GRAV-D Science Team, 2012).

Characteristic	Nominal Value
Altitude	20, 000 ft (~ 6.3 km)
Ground speed	250 knots (250 nautical miles/hr)
Along-track gravimeter sampling	1 sample per second = 128.6 m (at nominal ground speed)
Data Line Spacing	10 km
Data Line length	400 km
Cross Line Spacing	40-80 km
Cross Line Length	500 km
Data Minimum Resolution	20 km

Table 3.1 Nominal block and survey characteristics (GRAV-D Science Team, 2012).

The total sample size (four blocks together) is 389578, and the gravity values range between 975480 mgal and 977490 mgal. Keep in mind, the standard gravity is 980665 mgal. The descriptive statistics of airborne gravity data is listed in upper right corner of Figure 3.3. Figure 3.4 shows the normal QQ plot of airborne gravity data. The airborne gravity data was fixed by using free-air reduction and by the international gravity formula (Li and Götze, 2001).

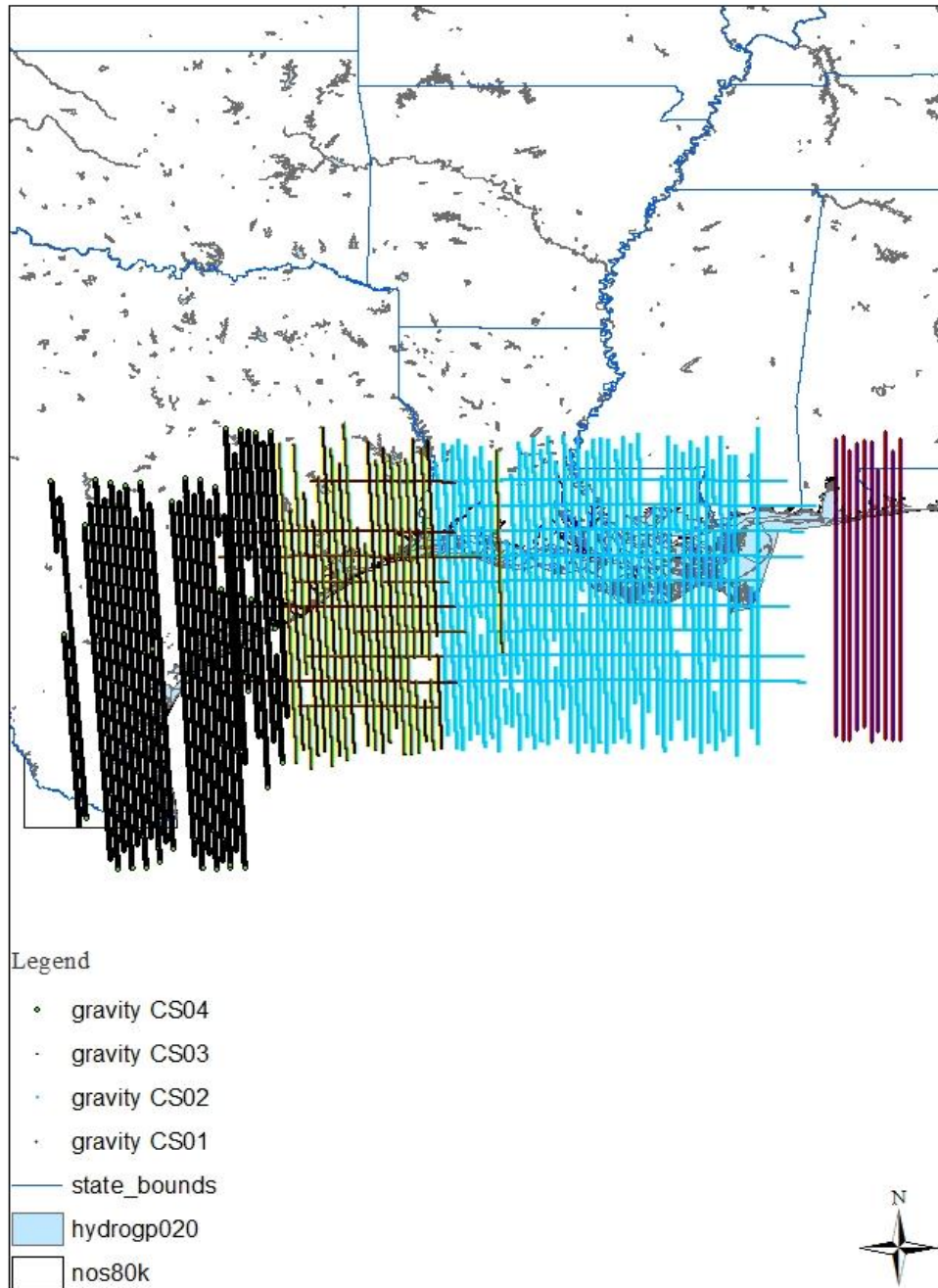


Figure 3.1 Tracks and locations of data of airborne gravity. Gravity data plotted by individual block from CS01 to CS04.

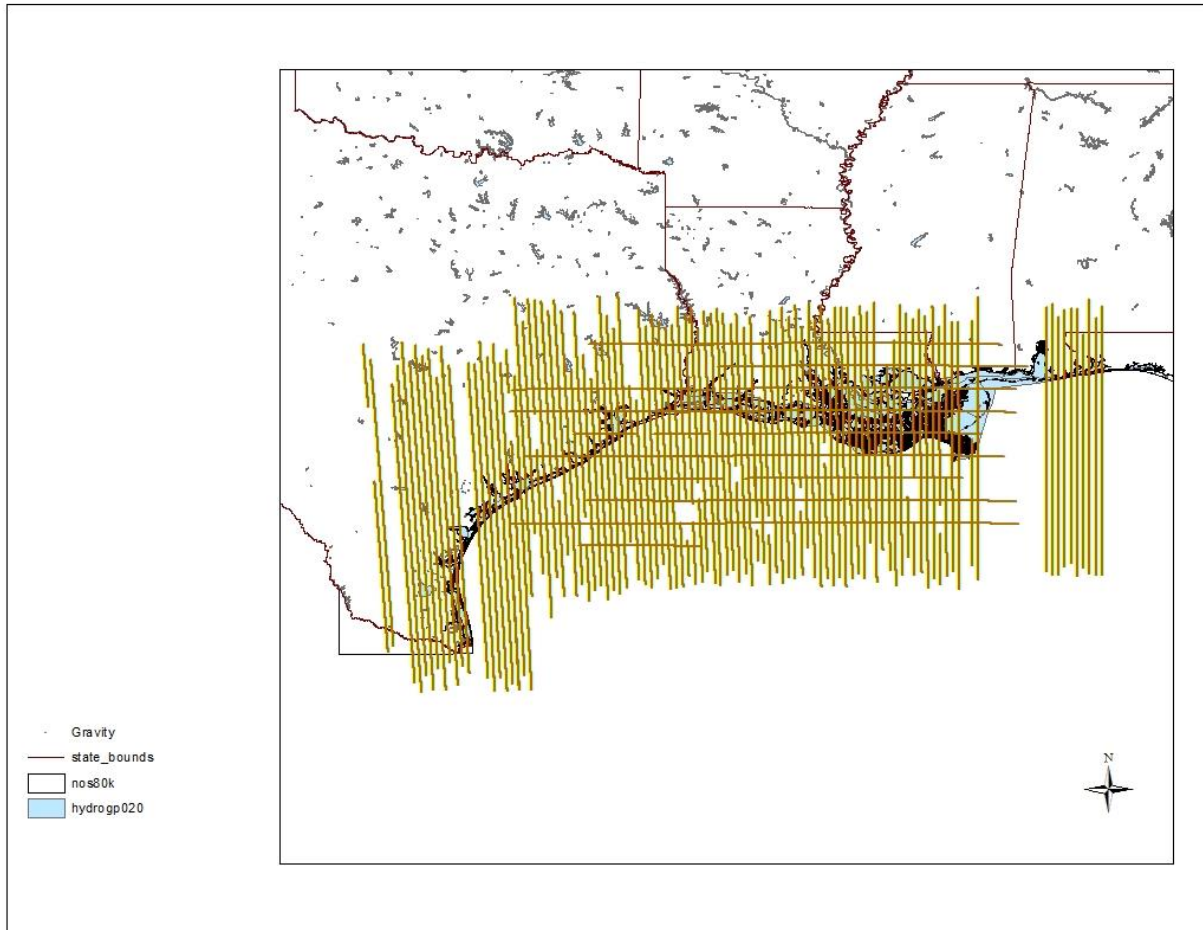


Figure 3.2 Tracks and locations of data of airborne gravity. Gravity data plotted by four blocks as a group.

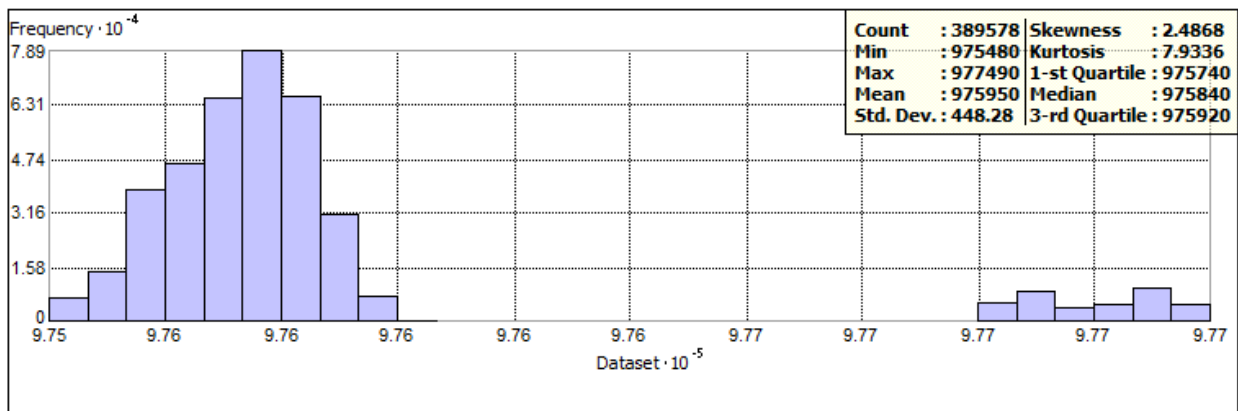


Figure 3.3 Frequency histogram with descriptive statistics for airborne gravity data (unit in mgal).

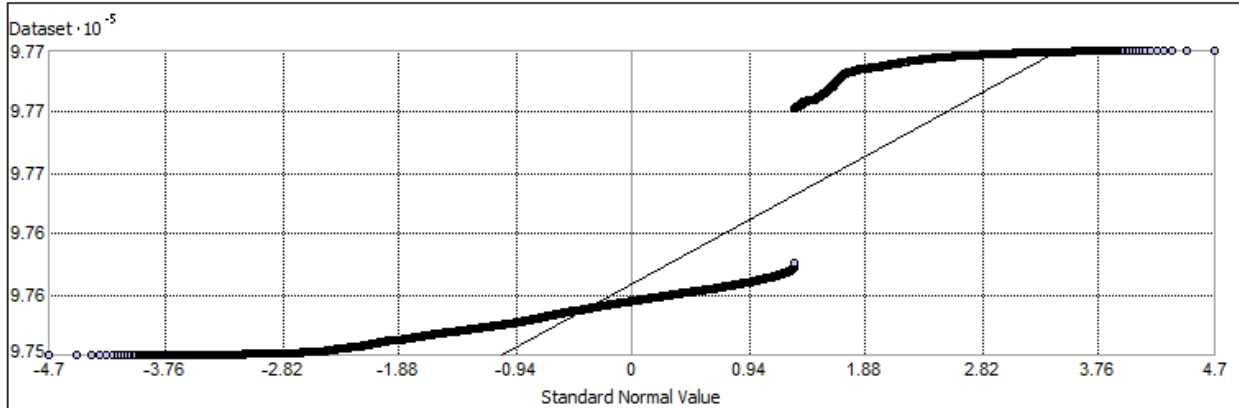


Figure 3.4 Normal QQ plot of airborne gravity data (unit in mgal).

3.1.1 Free-air correction (FAC)

The masses of outside the geoid need to be removed by using different gravity corrections in aim to determine the geoid. Gravity need to be reduced refer to the geoid. As a Taylor series (Li and Götze, 2001; Hofmann-Wellenhof & Moritz, 2006), the gravity reduced onto the geoid g_g may be calculated by

$$g_g = g_o - \frac{\partial g}{\partial H} H \quad (3.1)$$

where g_o is the observed gravity, and H is the elevation. $\frac{\partial g}{\partial H}$ is considered as free-air correction factor which is 0.3086 mgal/m. g_g presented on Figure 3.5, and the values ranged from 978960 mgal to 979470 mgal with a mean of 979230 mgal and standard deviation 105.79 mgal.

Normality of sampling distribution is tested for determining kriging methods. In order to do so, skewness and kurtosis are tested within data of gravity on the geoid (Figure 3.6). The skewness is -0.29, which is slight left skewed distribution. The values are more concentrated on the right of mean. The kurtosis is 2.28, which is flattened than a normal distribution with a wide peak

(platykurtic). Points on the Normal QQ plot (Figure 3.7) also deviate from the reference line represented in black line.

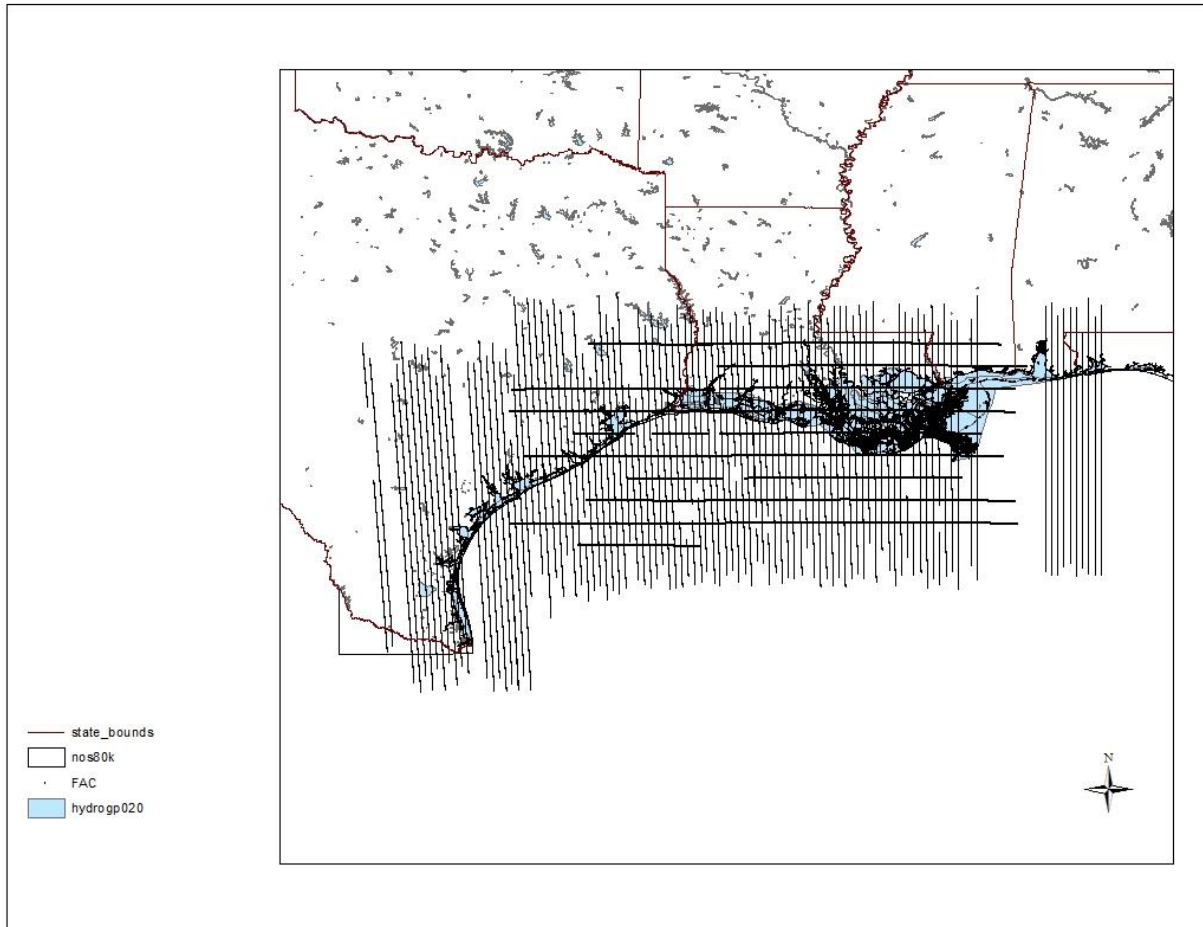


Figure 3.5 The airborne gravity reduced onto the geoid by free-air correction.

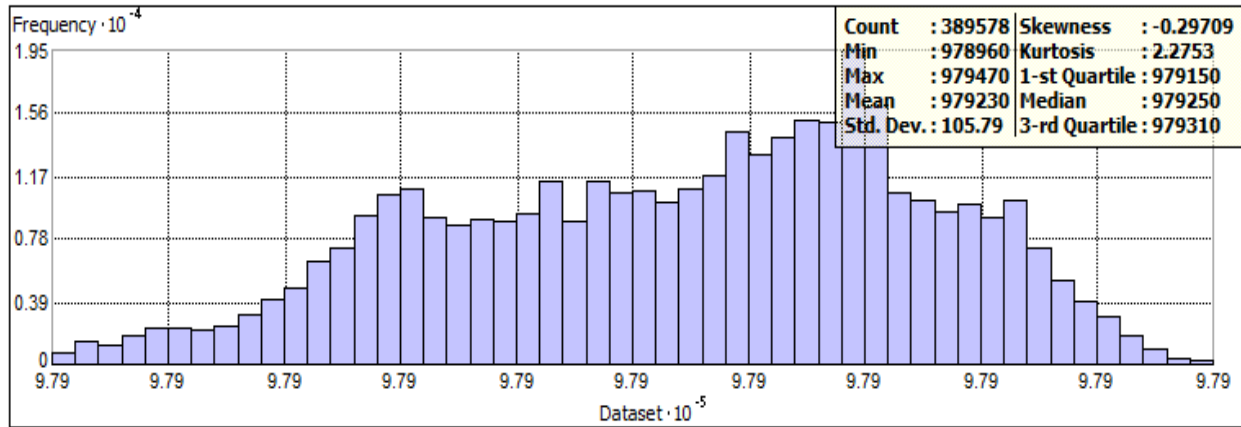


Figure 3.6 Frequency histogram with descriptive statistics for data of gravity on the geoid (unit in mgal).

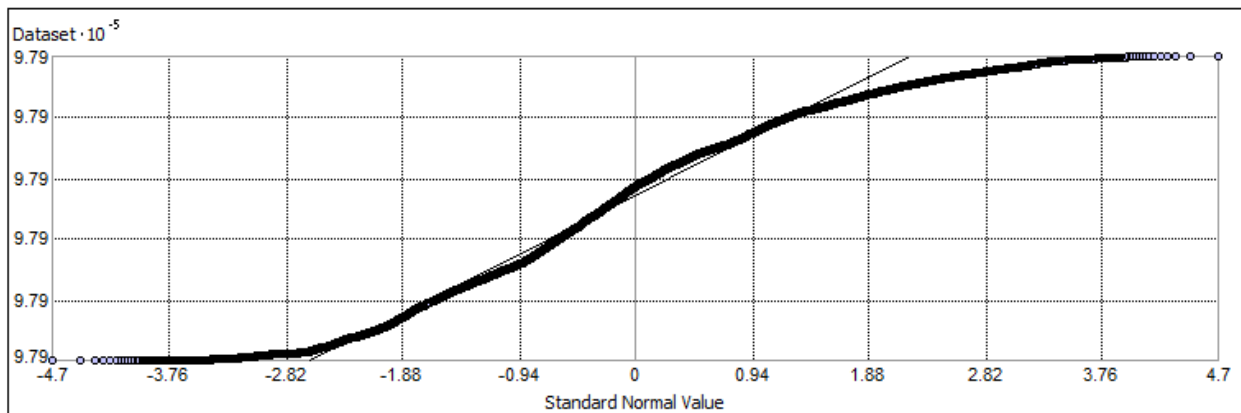


Figure 3.7 Normal QQ plot of gravity on the geoid data (unit in mgal).

3.1.2 The international gravity formula (IGF)

The international gravity formula estimates theoretical gravity change with latitude on the ellipsoid surface. Based on the Helmert theorem, there are several international gravity formulas. The difference of these IGFs is explained in Li and Götze (2001). IGF 1980 (Moritz, 1980; Li and Götze, 2001) is used in this study:

$$\gamma = 978032.7(1 + 0.0053024\sin^2\phi - 0.0000058\sin^22\phi) \quad (3.2)$$

where ϕ is the latitude; the unit of γ is mgal.

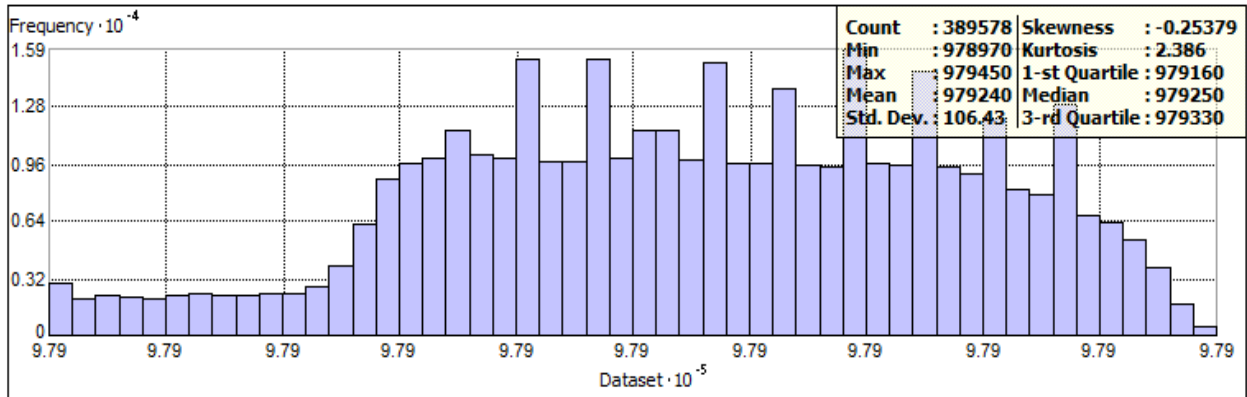


Figure 3.8 Frequency histogram with descriptive statistics for data of gravity on the ellipsoid (unit in mgal).

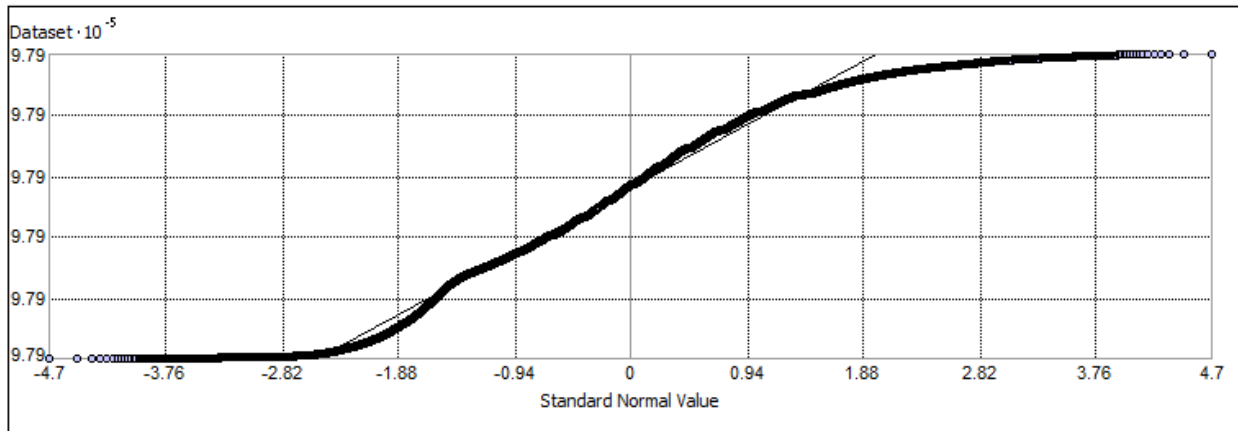


Figure 3.9 Normal QQ plot of gravity on the ellipsoid data (unit in mgal).

The values of gravity on the ellipsoid ranged from 978970 mgal to 979450 mgal with a mean of 979240 mgal and standard deviation 106.43 mgal. More details about descriptive statistics are listed in upper right corner of Figure 3.8. Points on the Normal QQ plot (Figure 3.9) deviate from the reference line represented in black line.

3.2 Kriging of gravity on the geoid

3.2.1 Ordinary kriging of gravity on the geoid

The Methodology will not be explained again, and similar explanation can be found in chapter 2 of this dissertation. Similar processes as the ordinary kriging method is conducted in ArcGIS 10.1, which are semivariogram modeling, searching neighborhood, and cross validation. The nugget, the range and the partial sill of the semivariogram were compared between the stable technique and the Gaussian technique of the ordinary kriging. There is no difference between the stable technique and the Gaussian technique of the ordinary kriging of gravity on the geoid (Table 3.2). In this case, the semivariogram displaced in Figures 3.10 to 3.13 stands for both stable and Gaussian techniques, and the model “perfect” fit through the averaged binned values at the distance h .

Type	Nugget	Range	Partial Sill	Sill
Stable	28.12	5.52	16437.37	16465.49
Gaussian	28.12	5.52	16437.37	16465.49

Table 3.2 Comparison of the components of stable and Gaussian semivariogram (units of nugget, partial sill and sill are mgal^2 ; unit of range is degree).

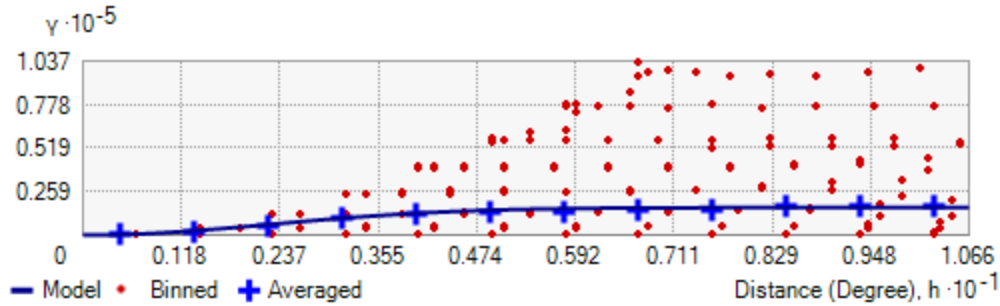


Figure 3.10 Semivariogram model of the ordinary kriging. The averaged semivariogram values on the y-axis (in mgal^2), and distance (or lag) on the x-axis (in degree). Binned values are shown as red dots, which are sorted the relative values between points based on their distances and directions and computed a value by square of the difference between the original values of points; Average values are shown as blue crosses, which are generated by binning semivariogram points; The model is shown as blue curve, which is fitted to average values. Model: $28.118 \cdot \text{Nugget} + 16437 \cdot \text{Stable}(5.53, 2)$; Model: $28.118 \cdot \text{Nugget} + 16437 \cdot \text{Gaussian}(5.53)$.

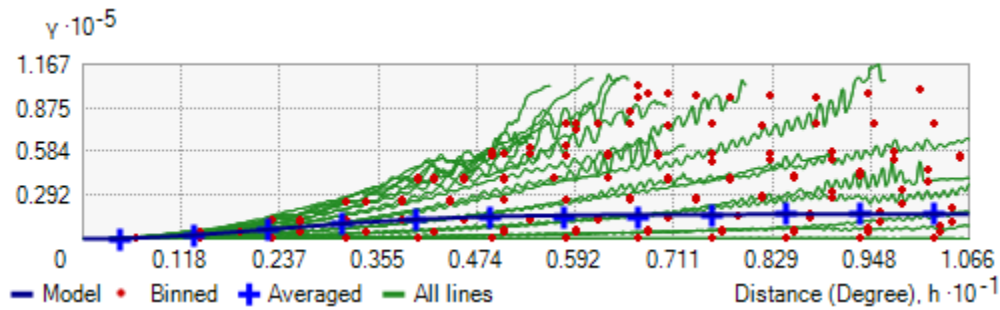


Figure 3.11 Semivariogram with all lines (green lines) which fit binned semivariogram values. The averaged semivariogram values on the y-axis (in mgal^2), and distance (or lag) on the x-axis (in degree).

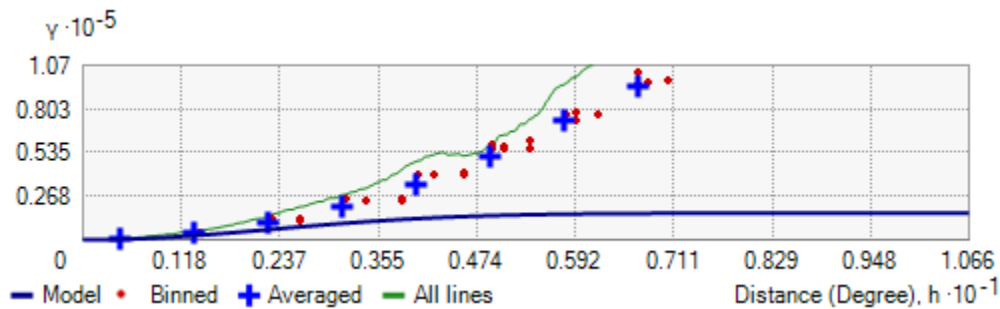


Figure 3.12 Semivariogram with showing search direction. The tolerance is 45 and the bandwidth (lags) is 3. The local polynomial shown as a green line fits the semivariogram surface in this case. The averaged semivariogram values on the y-axis (in mgal^2), and distance (or lag) on the x-axis (in degree).

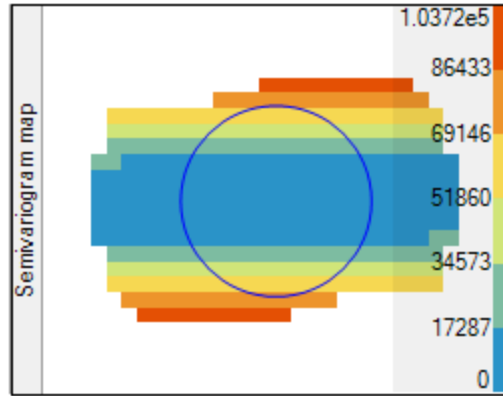
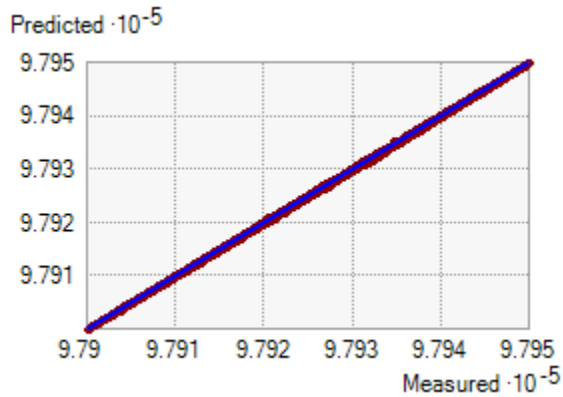


Figure 3.13 A semivariogram map. The color band shows semivariogram values with weights (unit in mgal^2).

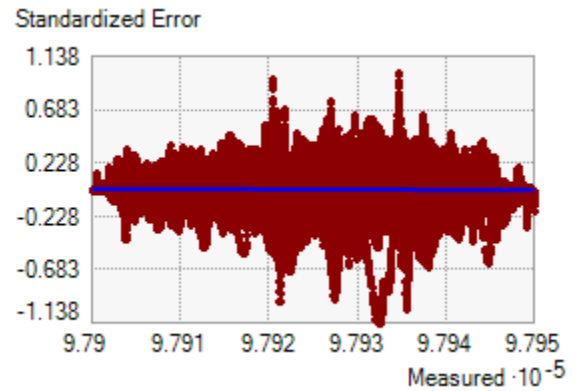
The Predicted, error, standard error, and normal QQ plot graphs are plotted respectively in Figure 3.14 (A to D). The predicted graph shows how well the known sample value was predicted compared to its actual value. The regression function in Figure 3.14A is $f(x) = 0.9999x + 125.1751$. By visually analyzed the graph, the regression function is closely aligned with the reference line. Therefore, it is well predicted.

The error graph shows the difference between known values and predictions for these values. The error equation in Figure 3.14B is $y = -0.0001x + 125.1751$. The standardized error graph shows the error divided by the estimated kriging errors. The standardized error equation in Figure 3.14C is $y = -0.00002x + 22.9974$. The normal QQ plot of the standardized error (Figure 3.14D) shows how closely the difference between the errors of predicted and actual values align with the standard normal distribution (the reference line).

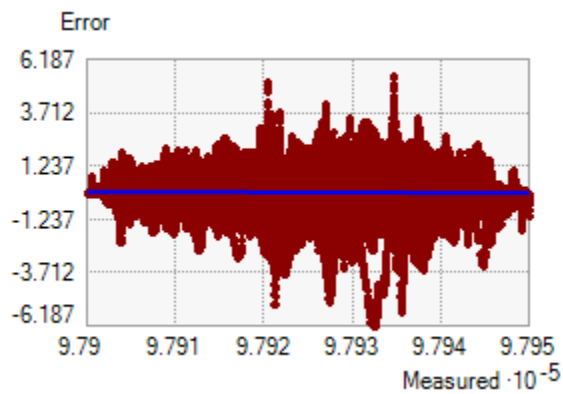
Figure 3.15 to Figure 3.18 displace the prediction and standard error map by using the ordinary kriging with stable and Gaussian techniques.



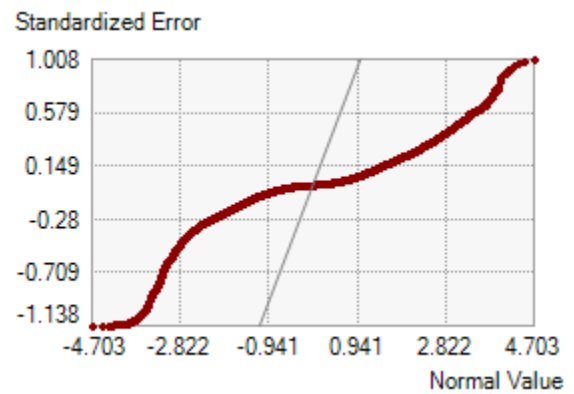
A.



C.



B.



D.

Figure 3.14 Cross validation of the ordinary kriging (unit in mgal).

- A. The predicted graph. The blue line represents the regression function, and the black line represents the reference line;
- B. The error graph. The blue line represents the error equation;
- C. The standardized error graph. The blue line represents the standardized error equation;
- D. The normal QQ plot of the standardized error. The reference line is represented by the black line.

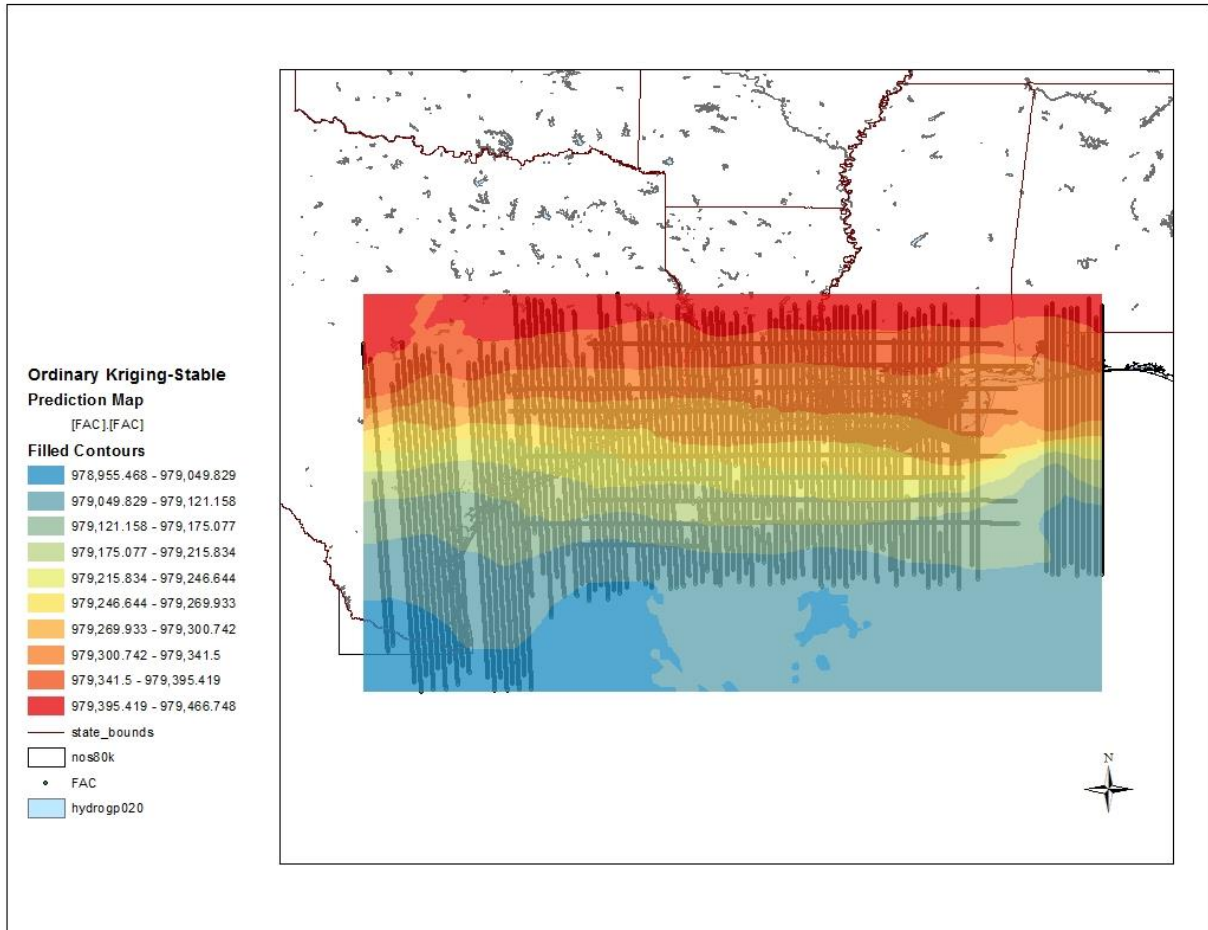


Figure 3.15 The ordinary stable kriging predictions map (unit in mgal).

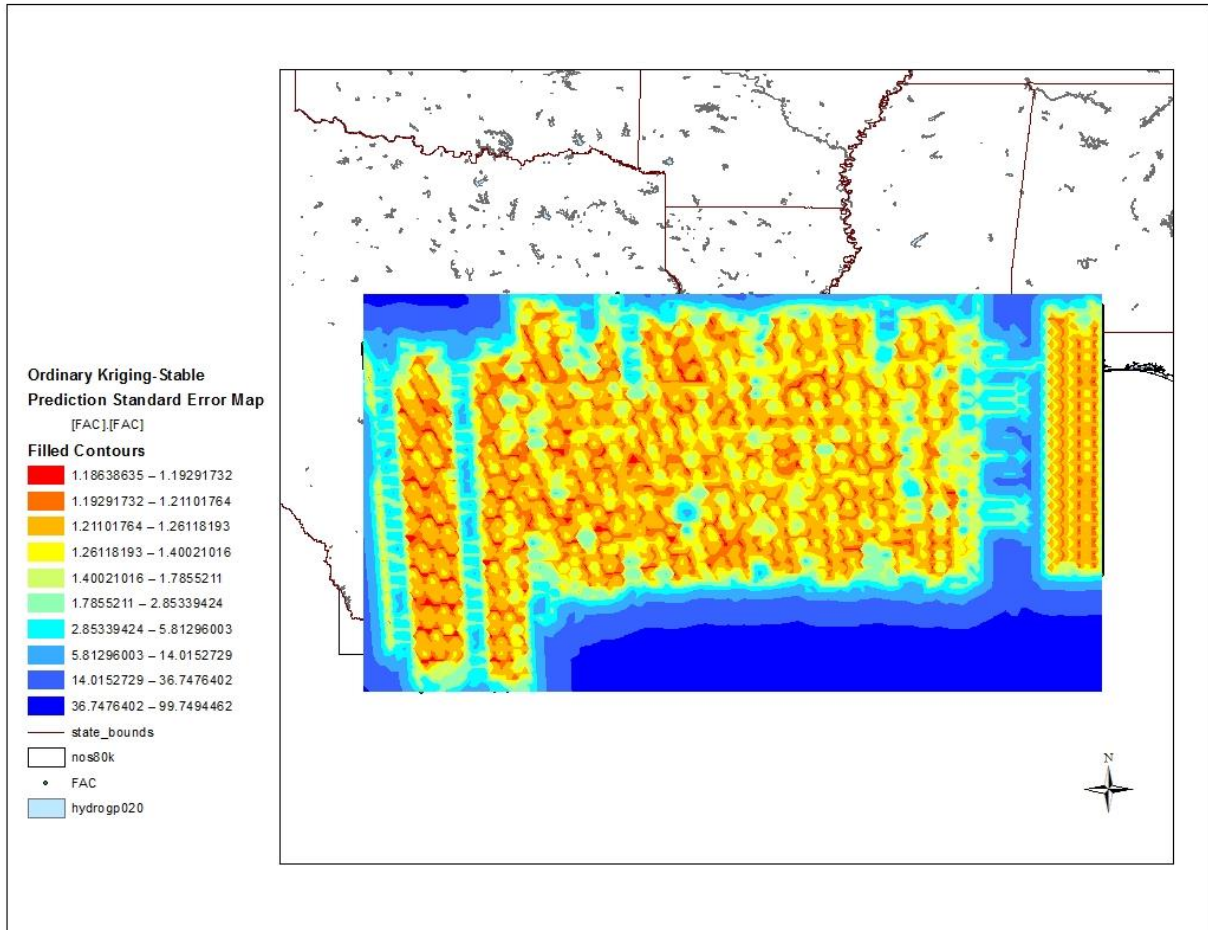


Figure 3.16 The ordinary stable kriging prediction standard error map (unit in mgal).

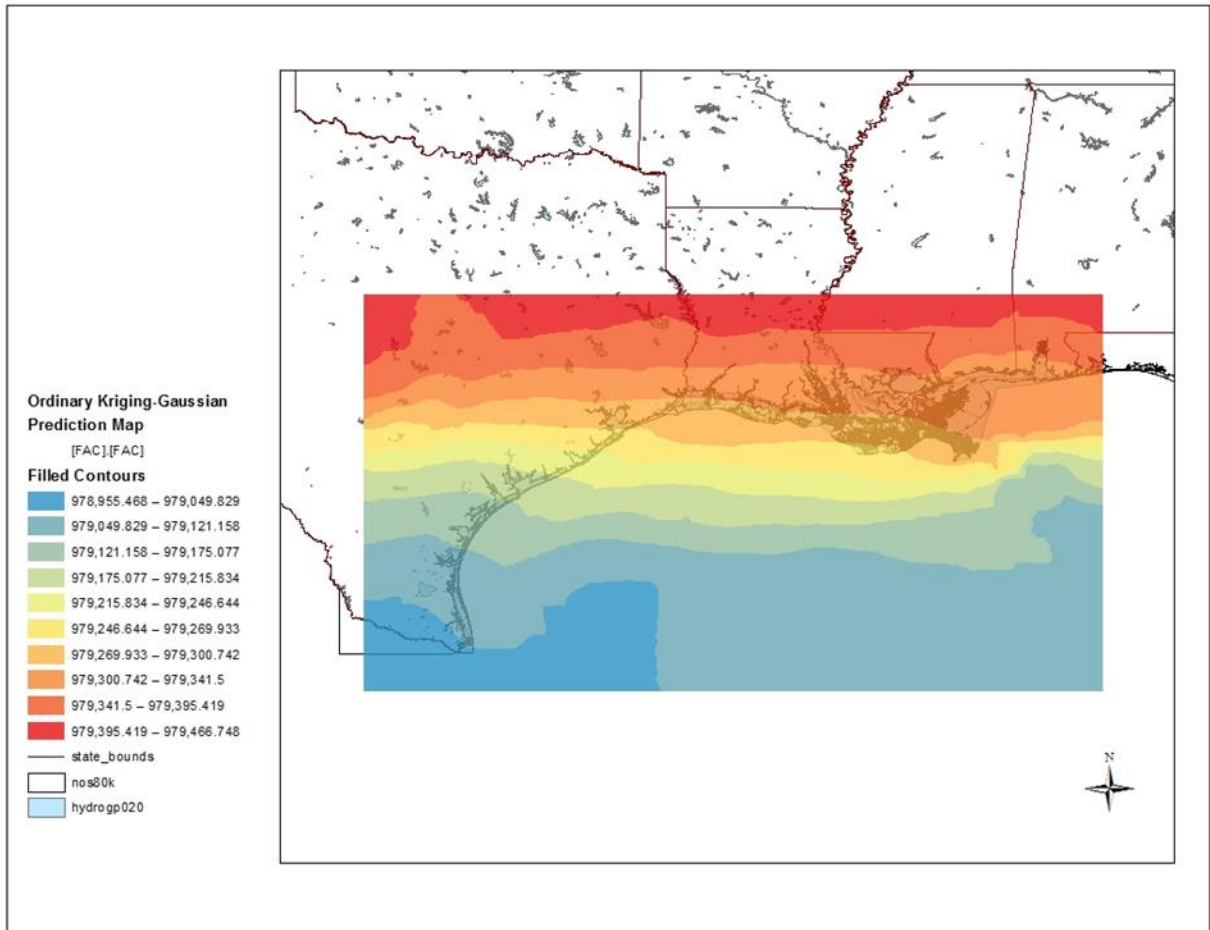


Figure 3.17 The ordinary Gaussian kriging predictions map (unit in mgal).

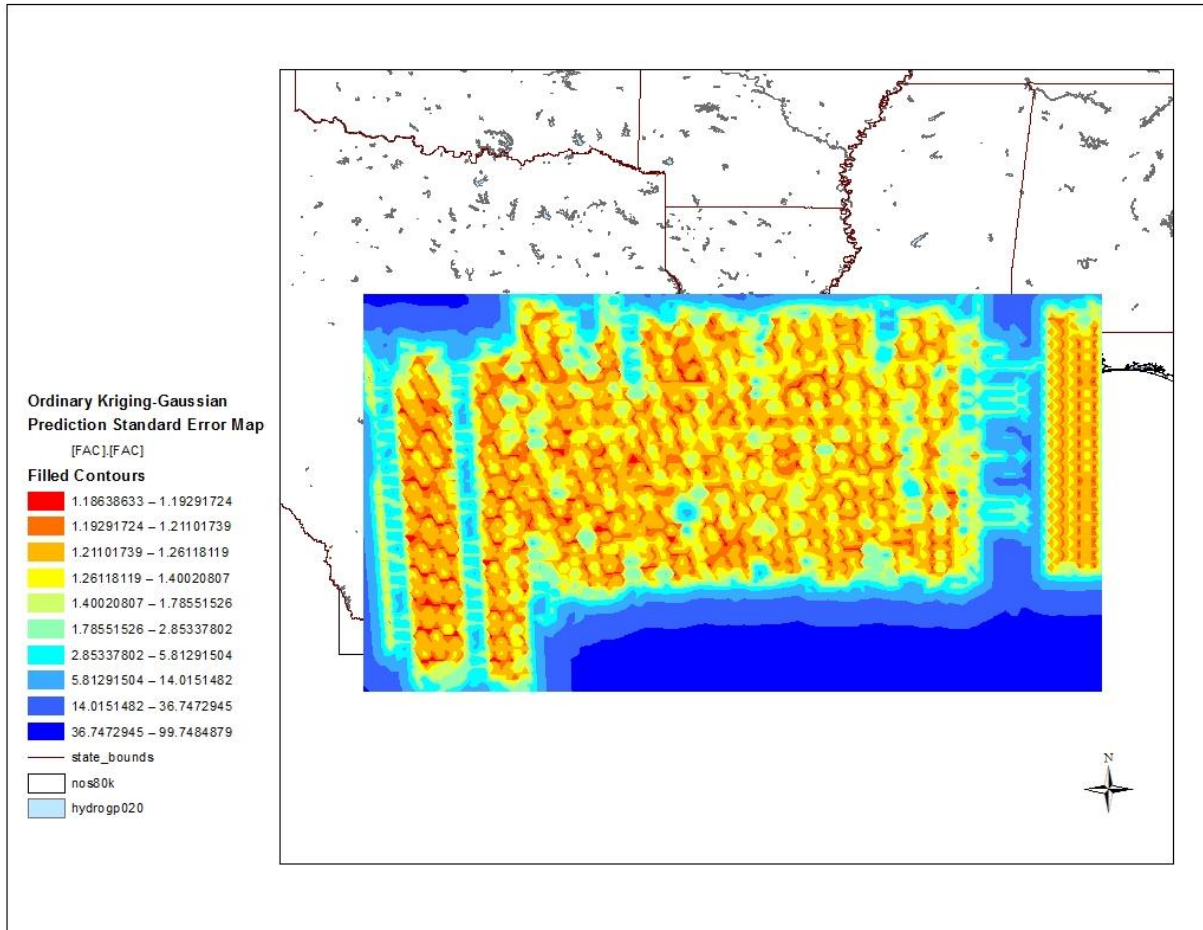


Figure 3.18 The ordinary Gaussian kriging prediction standard error map (unit in mgal).

3.2.2 Universal kriging of gravity on the geoid

Trend analysis was presented in Figure 3.19. There is no trend because the curve through the projected points is flat (as shown by the light blue line in the Figure 3.19). A slight downward curve as shown by the red line in Figure 3.19 is through the projected points on ZY plane, which suggests that it may have a trend exist in gravity on the geoid data. Therefore, de-trend is conducted before the universal kriging process in order to prevent biased the analysis. Because the curve shown on ZY plane is not obvious, the de-trend approach is chosen to remove the trend order as constant. The process was conducted in ArcGIS 10.1 by using Geostatistical

Analyst. Results of the universal kriging with either the stable technique or the Gaussian technique were shown as exact same as results of the ordinary kriging.

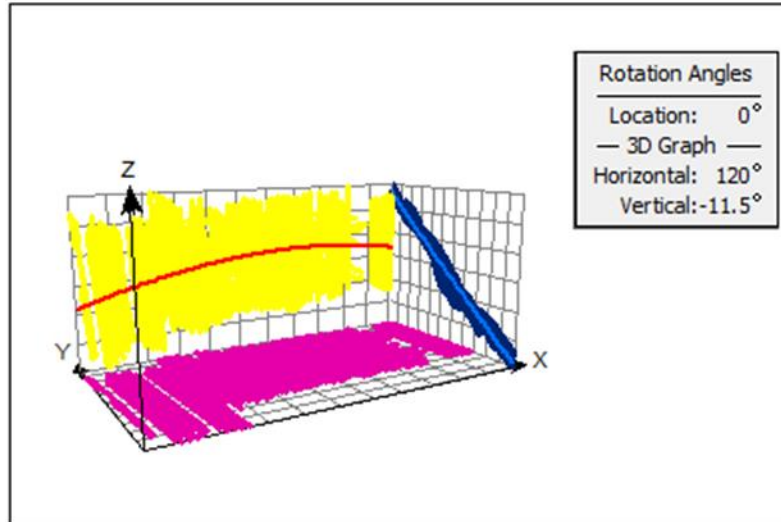


Figure 3.19 Trend analysis of gravity on the geoid.

Legend: Grid (XYZ): Number of Grid Lines 11×11×6; Projected Data: YZ plane (Dark Blue), ZY plane (Yellow), XY plane (Peony Pink); Trend on Projections: YZ plane (Light Blue), XZ plane (Red); Axes (Black).

3.2.3 Results and Evaluation of Error

A better interpolation method should have a smaller RMS. Due to no difference between the ordinary kriging and universal kriging in this case; statistical results were same that listed in Table 3.3. The prediction error mean is 0.0038 mgal. As 1 meter increased in altitude, the gravity is decreased by 0.3086 mgal. With simple conversion, the accuracy of prediction is approximately 0.0123 meters. Namely, it is around 1.23 cm, which was expected.

RMS Standardized	0.1084
Mean Standardized	0.0007
Average Standard Error (ASE)	5.5060
Root Mean Square (RMS)	0.5918
Difference between RMS and ASE	4.9142
Difference in Percentage	89.25%

Table 3.3 Statistics (unit in mgal).

3.3 Kriging of difference between gravity on the ellipsoid and the geoid

The kriging method used in this section is still the ordinary kriging with the stable technique. The nugget in semivariogram (Figures 3.20 to 3.22) is approximately 1.0324 mgal^2 , which is very small. The range is 2.2212 degree, and the partial sill is 355.2671 mgal^2 . Figure 3.23 is an example of a semivariogram map with weight values.

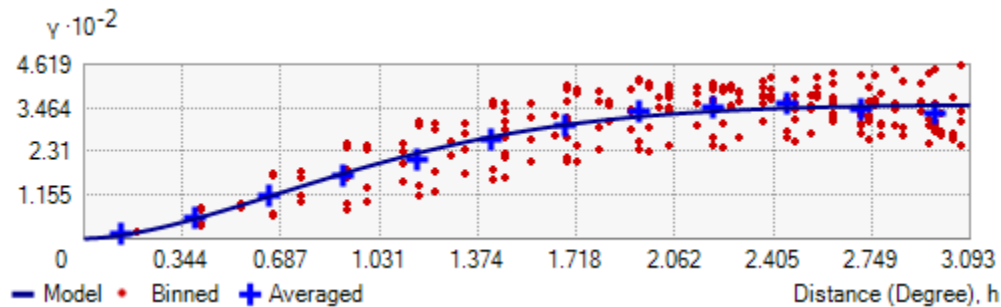


Figure 3.20 Semivariogram model of the ordinary kriging. The averaged semivariogram values on the y-axis (in mgal^2), and distance (or lag) on the x-axis (in degree). Binned values are shown as red dots, which are sorted the relative values between points based on their distances and directions and computed a value by square of the difference between the original values of points; Average values are shown as blue crosses, which are generated by binning semivariogram points; The model is shown as blue curve, which is fitted to average values. Model : $1.0324 \cdot \text{Nugget} + 355.27 \cdot \text{Stable}(2.2212, 1.6818)$.

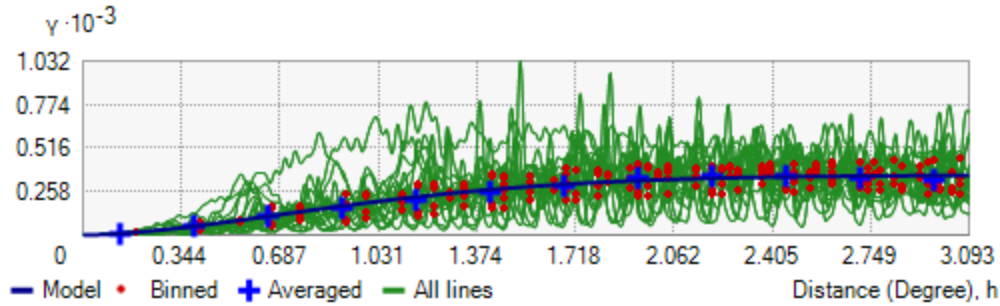


Figure 3.21 Semivariogram with all lines (green lines) which fit binned semivariogram values. The averaged semivariogram values on the y-axis (in mgal^2), and distance (or lag) on the x-axis (in degree).

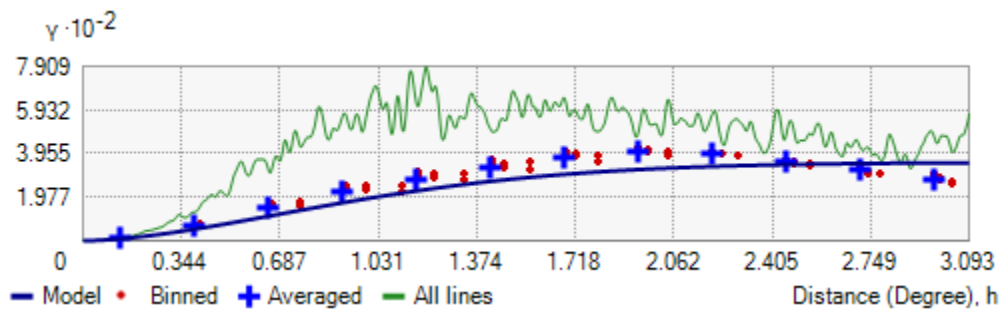


Figure 3.22 Semivariogram with showing search direction. The tolerance is 45 and the bandwidth (lags) is 3. The local polynomial shown as a green line fits the semivariogram surface in this case. The averaged semivariogram values on the y-axis (in mgal^2), and distance (or lag) on the x-axis (in degree).

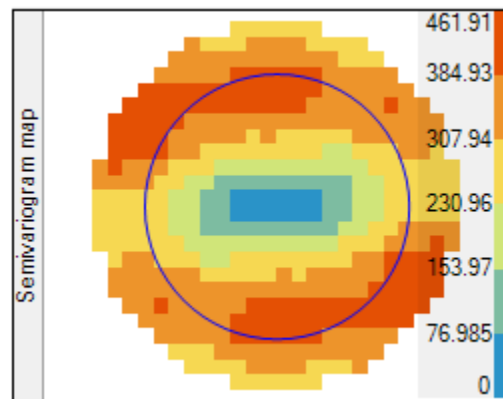
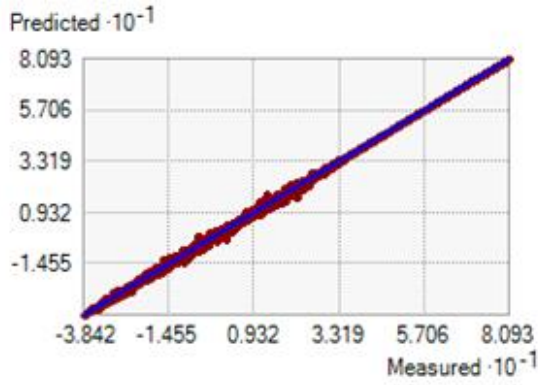
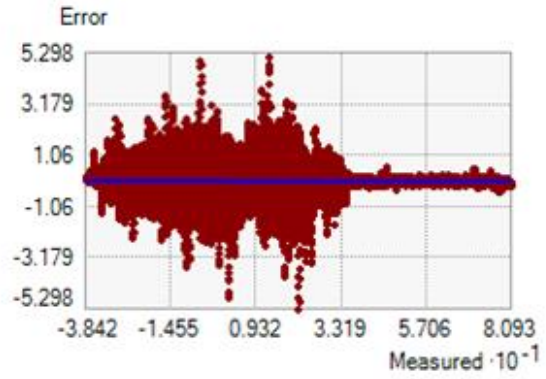


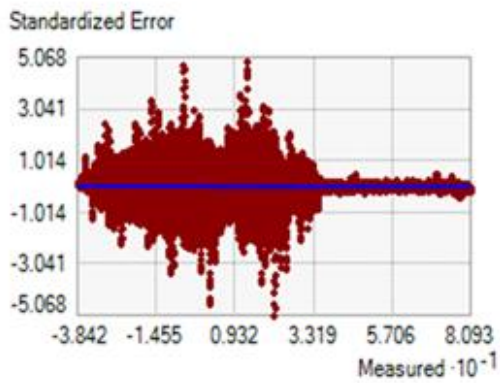
Figure 3.23 A semivariogram map. The color band shows semivariogram values with weights (unit in mgal^2).



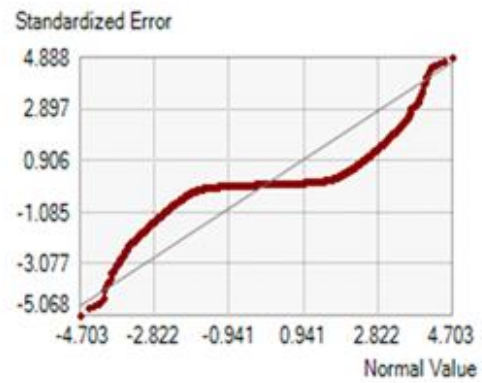
A. $y = 0.9997x + 0.0021$



B. $y = -0.0003x + 0.0021$



C. $y = -0.0002x + 0.0020$



D.

Figure 3.24 Cross validation of the ordinary kriging (unit in mgal).

The Predicted, error, standard error, and normal QQ plot graphs are plotted respectively in Figure 3.24 (A to D). Statistical results of the ordinary kriging of difference between gravity on the ellipsoid and the geoid listed in Table 3.4. The prediction yields very small RMS. The mean of prediction error is approximately 0.00076 mgal. Figure 3.25 is the ordinary kriging prediction map which displaces the shape of the geoid.

RMS Standardized	0.2249
Mean Standardized	0.0007
Average Standard Error (ASE)	1.0672
Root Mean Square (RMS)	0.2369
Difference between RMS and ASE	0.8303
Difference in Percentage	77.80%

Table 3.4 Statistics (unit in mgal).

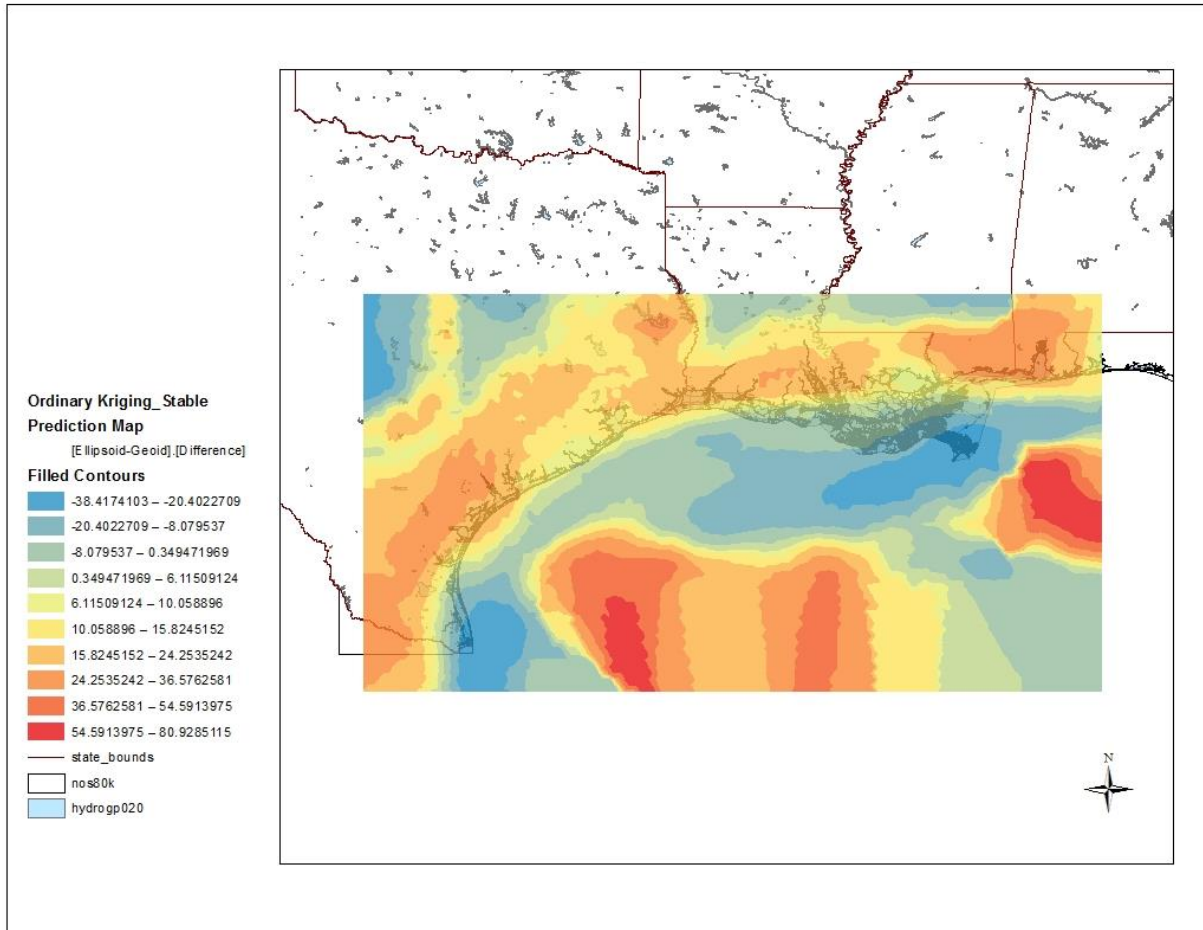


Figure 3.25 The ordinary kriging predictions map (unit in mgal).

3.4 Acknowledgements

Thanks to NGS at NOAA for open access to download GRAV-D airborne gravity data. For more information and project materials, visit NGS on the Web (GRAV-D Homepage: <http://www.ngs.noaa.gov/GRAV-D>). Other file data used in the map (named as nos80k, state_bounds, hydrogp020) was download from USGS.

3.5 References

Drinkwater, M. R., Floberghagen, R., Haagmans, R., Muzi, D., & Popescu, A. (2003). VII:

CLOSING SESSION: GOCE: ESA's First Earth Explorer Core Mission. *Space Science Reviews, 108* (1-2), 419-432.

GRAV-D Science Team (2011). *GRAV-D General Airborne Gravity Data User Manual*. Theresa

M. Diehl, ed., Version 1. Access April 19, 2012. Available from:

http://www.ngs.noaa.gov/GRAVD/data_cs01.shtml.

GRAV-D Science Team (2011). *Gravity for the Redefinition of the American Vertical Datum*

(GRAV-D) Project, Airborne Gravity Data; Block CS01. Access April 19, 2012.

Available from: http://www.ngs.noaa.gov/GRAV-D/data_cs01.shtml.

GRAV-D Science Team (2011). *GRAV-D General Airborne Gravity Data User Manual*. Theresa

Diehl, ed. Version 1. Access April 19, 2012. Available from:

http://www.ngs.noaa.gov/GRAVD/data_CS02.shtml.

GRAV-D Science Team (2012). *Gravity for the Redefinition of the American Vertical Datum*

(GRAV-D) Project, Airborne Gravity Data; Block CS02. Access April 19, 2012.

Available from: http://www.ngs.noaa.gov/GRAV-D/data_CS02.shtml.

GRAV-D Science Team (2012). *GRAV-D General Airborne Gravity Data User Manual*. Theresa

Diehl, ed. Version 1. Access April 19, 2012. Available from:

http://www.ngs.noaa.gov/GRAVD/data_CS03.shtml.

GRAV-D Science Team (2012). *Gravity for the Redefinition of the American Vertical Datum (GRAV-D) Project, Airborne Gravity Data; Block CS03*. Access April 19, 2012.

Available from: http://www.ngs.noaa.gov/GRAV-D/data_CS03.shtml.

GRAV-D Science Team (2011). *GRAV-D General Airborne Gravity Data User Manual*. Theresa Diehl, ed. Version 1. Access April 19, 2012. Available from:

http://www.ngs.noaa.gov/GRAVD/data_CS04.shtml.

GRAV-D Science Team (2011). *Gravity for the Redefinition of the American Vertical Datum (GRAV-D) Project, Airborne Gravity Data; Block CS04*. Access April 19, 2012.

Available from: http://www.ngs.noaa.gov/GRAV-D/data_CS04.shtml.

Hofmann-Wellenhof, B., & Moritz, H. (2006). *Physical geodesy* (2nd ed.). New York: Springer Wien.

HYDROGP020 - U.S. National Atlas Water Feature Areas: bays, glaciers, lakes and swamps.

(2003). *U.S. Geological Survey*. Accessed January 19, 2012. Available from:

<http://coastalmap.marine.usgs.gov/GISdata/basemaps/usa/water/hydrogp020.zip>.

Li, X., & Götze, H. J. (2001). Tutorial ellipsoid, geoid, gravity, geodesy, and geophysics.

Geophysics, 66, 1660-1668.

NOS80K - Medium Resolution Digital Vector U.S. Shoreline shapefile for the contiguous United

States. (1994). *National Oceanic and Atmospheric Administration (NOAA), National*

Ocean Service (NOS), Office of Coast Survey, and the Strategic Environmental

Assessments (SEA) Division of the Office of Ocean Resources Conservation and

Assessment (ORCA). Accessed January 19, 2012. Available from:

<http://coastalmap.marine.usgs.gov/GISdata/basemaps/coastlines/nos80k/nos80k.zip>.

Seeber, G. (2003). *Satellite geodesy* (2nd ed.). Berlin, New York: Walter de Gruyter.

STATE_BOUNDS: internal US state boundaries. *Valerie Paskevich*. Accessed January 19, 2012.

Available from:

[http://coastalmap.marine.usgs.gov/GISdata/basemaps/boundaries/state_bounds/state_bou
nds.zip](http://coastalmap.marine.usgs.gov/GISdata/basemaps/boundaries/state_bounds/state_bou
nds.zip)

Chapter 4: Computation of the Geoid Downward Corrections in Coastal Areas

This chapter was published: Song, H. Z., & Sadoski, A. L. (2011). Evaluation of Downward Corrections of Gravitational Free-air Anomalies to evaluate Geoid in the Coastal Areas.

Proceedings 2011 World Congress on Engineering and Technology. IEEE Press, 676-679.

This chapter deals with computation of the downward correction for the geoid determination in the coastal areas. Evaluation of precise geoid is very complicated in the coastal areas due to closeness of large masses of water and land which have different densities. We used MatLab and Stokes-Helmert integrals to find equipotential surfaces of gravity and then evaluate length of the plump lines and their deviation from geometrical perpendiculars in coastal areas. The difference between the plump line length and the length of geometrical perpendicular to the reference ellipsoid is needed to make right downward correction for determination of the precise geoid.

The importance of the knowledge of the exact geoid (Hofmann-Weeenhof & Moritz, 2006; <http://www.ngs.noaa.gov/GEOID/>) is necessary for the success of different human activities and even to its own survival. To know precise geoid may be the difference between life and death in the situations of tropical storms, floods, tsunamis, and other natural catastrophes. The other usefulness of the geoid is its positive impact on land issues, dredging, constructions, education, and few others. By using satellites scientists discovered long wave (large scale) geoid for the Earth (Seeber, 2003; Drinkwater et al., 2003), but its precision is not sufficient when it comes to the relatively small scale and/or local situations such as created by hurricanes Katherine (2005), Rita (2005), and Ike (2008) in the coastal areas of the Gulf of Mexico. So, it is quite timely to develop new and improve existing methods and models of the geoid determination at

the local level based on local observations of gravity and complimented by observations of gravity from the air and space. In today's satellite age the height can be determined with just a few centimeters of accuracy geometrically by the global positioning system (GPS).

It is well known that the greatest errors in the geoid determination (Smith & Mibert, 1999) happen either in the mountain terrain (due to sharp variations in the relief) or in coastal areas when two large bodies of water and land of quite different nature and density are brought together. We have to determine numerically for the future research the derivations of the plumb line from the geometrical vertical as long as they have visible origin, namely by a topographic surface of the continental relief, by a geological determination of the mass density of its constituents and by a systematic survey of the oceans according to well-established methods. Therefore, this study deals with the modeling of the equipotential surfaces for the ideal coastal areas. Initially we used Stoke-Helmert double integral for the 2D model:

$$U_{(p,q)} = G\rho_w \int_{-10}^0 dx \int_0^1 \frac{1}{\sqrt{(x-p)^2 + (y-q)^2}} dy + G\rho_l \int_0^{10} dx \int_0^1 \frac{1}{\sqrt{(x-p)^2 + (y-q)^2}} dy$$

The result was a very rough evaluation of the slopes of gravity surfaces if we make a vertical cut perpendicular to a shoreline where water and land meet.

To find more precise and better evaluation of equipotential gravitational surfaces we have used triple Stokes-Helmert integral over the rectangle surface with sides 100 km over 20 km and depth of 2 km. Half of this rectangle located over the water and another half located over land. The following integral:

$$U_{(p,q,w)} = G\rho_w \int_{-50}^0 dx \int_0^2 dy \int_{-10}^{10} \frac{1}{\sqrt{(x-p)^2 + (y-q)^2 + (z-w)^2}} dz$$

$$+ G\rho_l \int_0^{50} dx \int_0^2 dy \int_{-10}^{10} \frac{1}{\sqrt{(x-p)^2 + (y-q)^2 + (z-w)^2}} dz$$

Using MatLab software solves this equation. The code for triple integral shown in Figure 4.1.

```

X=-50000:10000:50000;
Y=2100:5000:10000;
w=-10000:5000:10000;
vmin = 0;
vmax = 2000;
wmin =-10;
wmax =10;
Z=zeros(size(X,2)*size(Y,2)*size(w,2),1);
k=1;
for m=1:size(X,2),
for n=1:size(Y,2);
for l=1:size(w,2);
integrnd= @(u,v,s) 1./sqrt((X(1,m)-u).^2+(Y(1,n)-v).^2+(w(1,l)-s).^2);
ulmin = min(X(1,m)-45000,0);
ulmax = min(X(1,m)+450000,0);
u2min=max(0 ,X(1,m)-4550000);
u2max=max(0,X(1,m)+4550000);
wlmin = min(w(1,l)-5000,0);
wlmax = min(w(1,l)+5000,0);
w2min=max(0 ,w(1,l)-50000);
w2max=max(0,w(1,l)+50000);
Z(k)= (6.673*10^(-11))*(1.03.*triplequad
(integrnd,ulmin,ulmax,vmin,vmax,wmin,wmax)+2.67*triplequad
(integrnd,u2min,u2max,vmin,vmax,wmin,wmax));
k=k+1;
end
end
end

Z2=reshape(Z,size(Y,2),size(X,2),size(w,2));
figure(1)
[X,Y,w]=meshgrid(-50000:10000:50000,2100:5000:10000,-10000:5000:10000);
surf(X(:,:,1),Y(:,:,1),Z2(:,:,1))
figure(2)
imagesc([X(1,1),X(1,size(X,2))] , [Y(1,1),Y(size(Y,1),1)] ,Z2); figure
(gcf)
figure(3)
contour(Z2)

```

Figure 4.1 Matlab code for triple integral.

The equipotential surfaces provide us with much needed information about plumb lines, which in turn would be very helpful for the downward continuation as well as for better use of the famous 0.3068 correction factor.

In this study we calculated downward error by using the knowledge of geometry. When angles are getting smaller enough, the values of tangent and sine are approximately equal to each other and an angle itself measured in radians. The change of the curvature of the plumb line is the same as a change of normal gravity, which could be expanded as a polynomial series of altitude; it is enough for practical purposes to use linear extension of the normal gravity. In the case of our model the angle of the tangent line changes from $\frac{4}{9}\pi 10^{-5}$ at point 0 to eventually 0 at distance 30 km from the border of land and water masses.

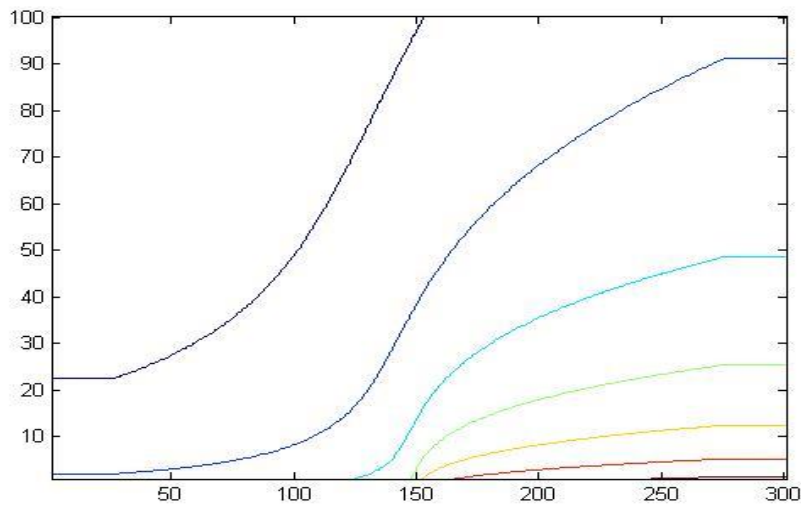


Figure 4.2 Equipotential levels.

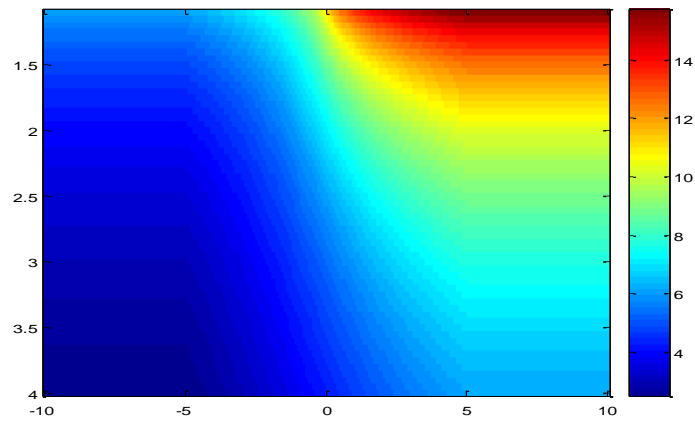


Figure 4.3 Gravitational potential.

Figures 4.2 and 4.3 were obtained by using MatLab, and they show equipotential levels and gravitation in the 2D plane normal to the Earth ellipsoid of reference at the shoreline. The next image on Figure 4.4 is more complicated. It represents levels of equipotential surfaces of gravity in the normal plane cut through the central point $(0, 0, 0)$ of the model. Because of the cut these surfaces are represented by lines from the sea level to altitude 12,000 meters.

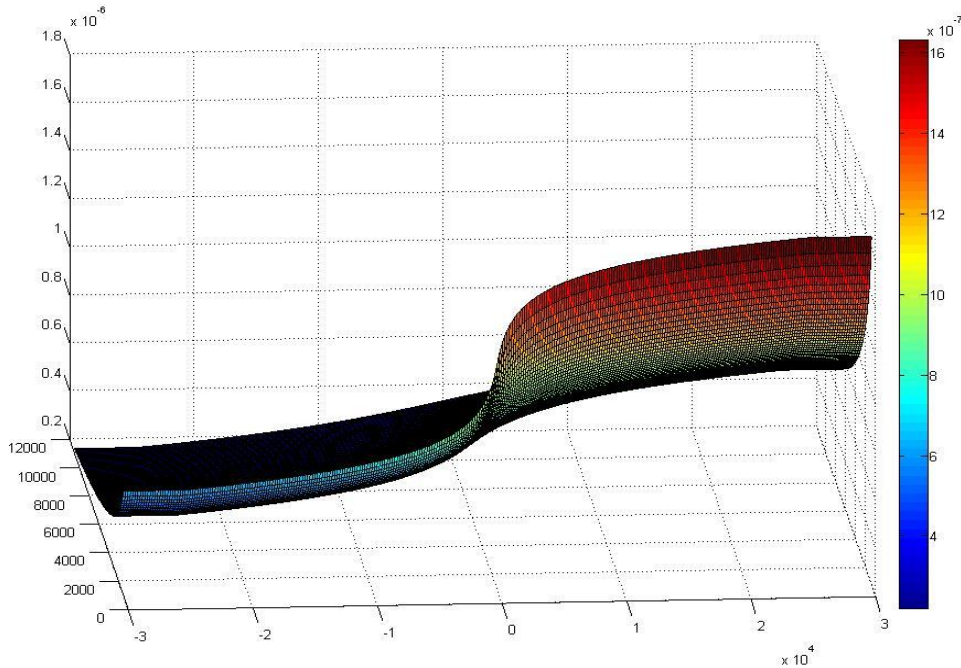


Figure 4.4 3D graph of equipotential surfaces of the vertical cut through the point (0,0,0).

Now we can evaluate deviation of the plumb line from the geometrical perpendicular. By using calculation results from MatLab and 2D and 3D images we can estimate curvature and, what is most important here, tangent lines and value of derivatives. With the purpose of finding deviations of plumb line from orthogonal we change the orientation from vertical to horizontal as shown in Figure 4.5. So it would be quite simple to evaluate the length of the plumb line and compare it with the length of geometrical orthogonal.

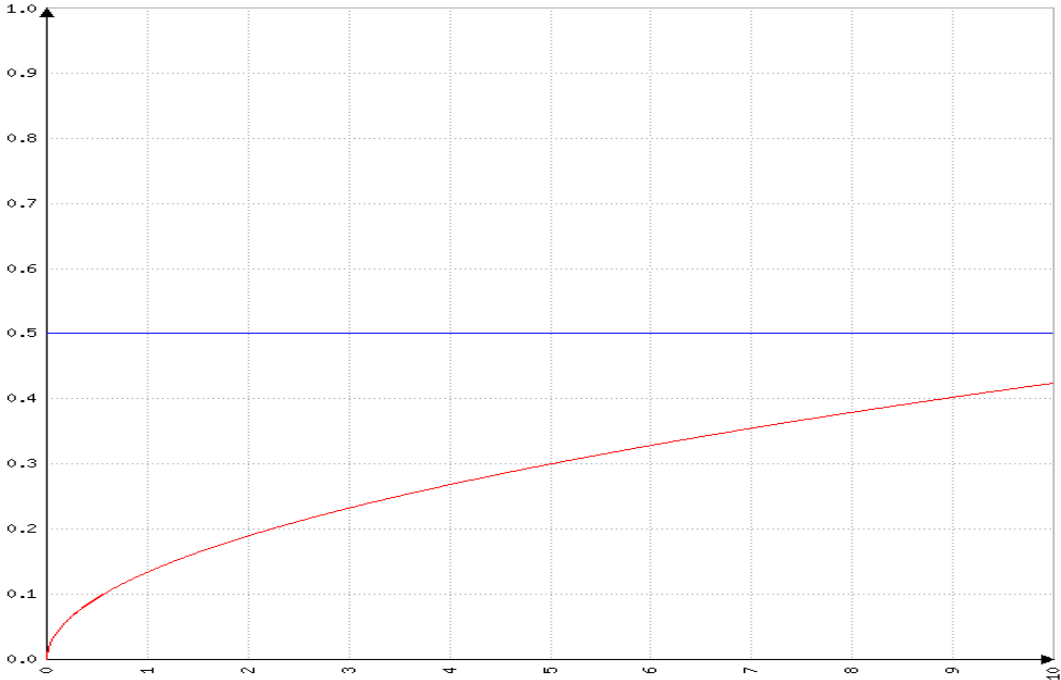


Figure 4.5 Geometrical straight line (blue) and plumb line (red) after rotation.

Knowing that angle of the tangent line changes over 10 kilometers of altitude rising from $\frac{4}{9}\pi 10^{-5}$ at the height 0 to $\frac{1}{12}\pi 10^{-5}$ at the height of 10 km, and assuming that derivative of the plumb line curvature is linear $f'(x) = kx + b$ we can evaluate $b = 5.67 \times 10^{-5}$ and $k = -0.54 \times 10^{-5}$. Then we use well known formula for the length of the curve:

$$L = \int_0^{10} \sqrt{1 + [0.0000567 - 0.0000054x]^2} dx = 10.0001658$$

So this calculation yields length L of such plumb line around 16.5 centimeters longer than geometrical vertical of 10 km. It is easy to see that curvature of the plumb lines diminishes if the move from the shoreline further inland or to the sea. We can expect that after 30 kilometers impact of water-land differences in densities will not have any effect on the curvature. It shows

that downward correction factor varies from maximum value of the order 16 cm at the shoreline to insignificant at the distances over 20 km.

It makes a good sense to improve downward correction close to the shore. For instance, to make a linear increase along a plumb lines between 16 cm at the water-land border ($x = 0$) to 0 at the distances greater or equal to $x = 20$ km inland or ocean ward. The maximum increase in the plumb line is an equivalent of around 0.5 mgal.

Numerical evaluations performed in this chapter show us the uncertainty in the calculation of precise geoid along the shoreline due to the variations in the shape of the shore and in the depths of the ocean close to the shore both of which could significantly affect precision of the geoid evaluation.

References

Drinkwater, M. R., Floberghagen, R., Haagmans, R., Muzi, D., & Popescu, A. (2003). VII:

CLOSING SESSION: GOCE: ESA's First Earth Explorer Core Mission. *Space Science Reviews*, 108 (1-2), 419-432.

Heiskanen, W. A., & Moritz, H. (1967). *Physical geodesy*. San Francisco, London: Freeman.

Hofmann-Wellenhof, B., & Moritz, H. (2006). *Physical geodesy* (2nd ed.). New York: Springer
Wien.

Seeber, G. (2003). *Satellite geodesy* (2nd ed.). Berlin, New York: Walter de Gruyter.

Smith, D. A., & Milbert, D. G. (1999). The GEOID96 high-resolution geoid height model for the United States. *Journal of Geodesy*, 73(5), 219-236.

Smith, J. R. (1997). *Introduction of geodesy: The history and concepts of modern geodesy*. New York, Chichester, Weinheim, Brisbane, Singapore, Toronto: John Wiley & Sons, Inc.

The Official NGS GEOID Page. Available from: www.ngs.noaa.gov/GEOID/.

Chapter 5: Evaluation of Errors of Gravity Potentials under the Conditions of Uncertainty in the Boundary Value Problems

It is well known that gravity potential V outside of the Earth surface could be found by solving Dirichlet boundary value problem of potential theory:

$$\Delta V = 0, \text{ where } \Delta V \equiv \frac{\partial^2 V}{\partial x^2} + \frac{\partial^2 V}{\partial y^2} + \frac{\partial^2 V}{\partial z^2} \text{ is called Laplacian,}$$

and $V(S)$ is a given value of the potential on the surface S . Here, for simplicity, we assume that the surface of the Earth is a sphere. We define solutions of the Laplace Equation $\Delta V = 0$ as harmonic functions. The most important harmonic functions are spherical harmonics. To introduce such functions we need spherical system of coordinates (Figure 5.1): r is a radius distance to a point P , ϑ is a polar distance in radians from the vertical axis, and λ is a geocentric longitude.

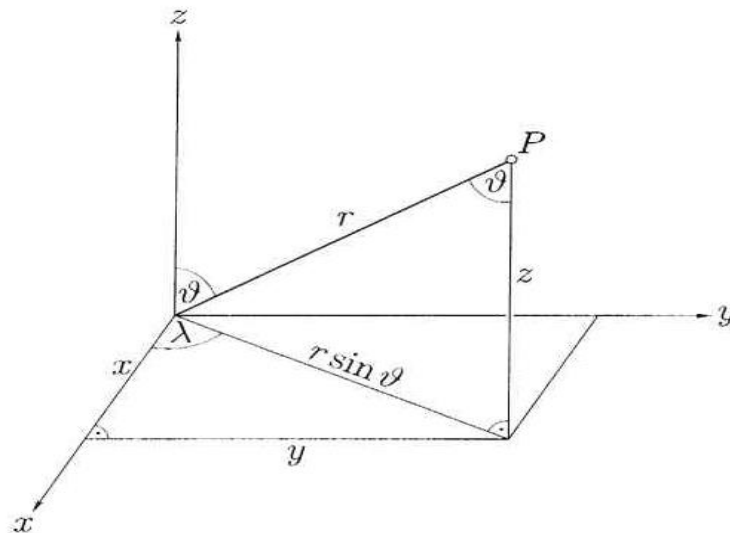


Figure 5.1 Spherical and rectangular coordinates (Hofmann-Wellenhof & Moritz, 2006).

Defining relation between rectangle and spherical coordinates

$$x = r \sin \vartheta \cos \lambda \quad y = r \sin \vartheta \sin \lambda \quad z = r \cos \vartheta \quad r = \sqrt{x^2 + y^2 + z^2},$$

we can now look for harmonic solutions by solving the following Laplace equation in spherical coordinates:

$$\Delta V \equiv \frac{\partial^2 V}{\partial r^2} + \frac{2}{r} \frac{\partial V}{\partial r} + \frac{1}{r^2} \frac{\partial^2 V}{\partial \vartheta^2} + \frac{\cot \vartheta}{r^2} \frac{\partial V}{\partial \vartheta} + \frac{1}{r^2 \sin^2 \vartheta} \frac{\partial^2 V}{\partial \lambda^2} = 0, \text{ or} \quad (5.1)$$

$$r^2 \frac{\partial^2 V}{\partial r^2} + 2r \frac{\partial V}{\partial r} + \frac{\partial^2 V}{\partial \vartheta^2} + \cot \vartheta \frac{\partial V}{\partial \vartheta} + \frac{1}{\sin^2 \vartheta} \frac{\partial^2 V}{\partial \lambda^2} = 0 \quad (5.2)$$

We will solve Laplace equation by using well known technique of separating variables (Folland, 1976). Namely, we will look for the solution V as a product of two functions, one of them depended solely on radius distance r , while another depends on pair of angles ϑ and λ :

$$V(r, \vartheta, \lambda) = f(r)Y(\vartheta, \lambda). \quad (5.3)$$

Performing substitution and differentiation in Equation 5.2, we get the following equation (Equation 5.4).

$$\frac{1}{f} (r^2 f'' + 2r f') = -\frac{1}{Y} \left(\frac{\partial^2 Y}{\partial \vartheta^2} + \cot \vartheta \frac{\partial Y}{\partial \vartheta} + \frac{1}{\sin^2 \vartheta} \frac{\partial^2 Y}{\partial \lambda^2} \right) \quad (5.4)$$

Left-hand side in Equation 5.4 depends only on r at the same time right-hand side depends only on angular values ϑ and λ . Here we will follow Hofmann-Wellenhof & Moritz (2006) notes to separate Equation 5.4 into two equations (Equations 5.5 & 5.6):

$$r^2 f''(r) + 2r f'(r) - n(n+1)f(r) = 0 \quad (5.5)$$

$$\frac{\partial^2 Y}{\partial \vartheta^2} + \cot \vartheta \frac{\partial Y}{\partial \vartheta} + \frac{1}{\sin^2 \vartheta} \frac{\partial^2 Y}{\partial \lambda^2} + n(n+1)Y = 0 \quad (5.6)$$

It will be very helpful in finding desired solutions if we have denoted the constants in the form $n(n + 1)$ in Equations 5.5 & 5.6.

Solutions of the Equation 5.5 in this case are given by formulas

$$f(r) = r^n \text{ and } f(r) = r^{-(n+1)}.$$

Denoting still unknown functions in Equation 5.6 by $Y_n(\vartheta, \lambda)$, we are able to figure out that Laplace Equation 5.1 is solved by functions:

$$V = r^n Y_n(\vartheta, \lambda) \text{ and } V = \frac{Y_n(\vartheta, \lambda)}{r^{n+1}}.$$

These two groups of functions are called *solid spherical harmonics*, while functions $Y_n(\vartheta, \lambda)$ are known as Laplace surface spherical harmonics.

We have to note that n is not just some number, but it must be an integer 0, 1, 2 ... to solve a given problem.

It is well known that sum of the solutions for linear differential equation is also a solution. So we can claim that

$$V = \sum_0^\infty r^n Y_n(\vartheta, \lambda) \text{ and } V = \sum_0^\infty \frac{Y_n(\vartheta, \lambda)}{r^{n+1}} \quad (5.7)$$

are also solutions of Laplace equation.

Now we are going to find spherical harmonics $Y_n(\vartheta, \lambda)$ by the way of using new substitution

$$Y_n(\vartheta, \lambda) = g(\vartheta)h(\lambda),$$

where functions g and h depend on only one variable each.

After substitution in Equation 5.5 and separating g and h , we come up with the following equation (Equation 5.8):

$$\frac{\sin\vartheta}{g} [\sin\vartheta g'' + \cos\vartheta g' + n(n+1)\sin\vartheta g] = -\frac{h''}{h} \quad (5.8)$$

The left-hand side is the function of ϑ only, and the right-hand side is the function of λ only, therefore both sides must be constant. Let us denote this constant m^2 . Then Equation 5.8 splits into two equations (Equations 5.9 & 5.10):

$$\sin\vartheta g''(\vartheta) + \cos\vartheta g'(\vartheta) + [n(n+1)\sin\vartheta - \frac{m^2}{\sin\vartheta}]g(\vartheta) = 0 \quad (5.9)$$

and

$$h''(\lambda) + m^2 h(\lambda) = 0 \quad (5.10)$$

Solutions of Equation 5.10 are functions

$$h(\lambda) = \cos m\lambda \quad \text{and} \quad h(\lambda) = \sin m\lambda,$$

which could be easily verified by substitution. It could be shown that only meaningful values for m are integers 1, 2, 3 ...

Equation 5.9 is Legendre's differential equation, and it may be shown that it has solutions only for integer values of m which are not greater than respective value of n .

In such a way function

$$g(\vartheta) = P_{nm}(\cos\vartheta)$$

and functions

$$Y_n(\vartheta, \lambda) = P_{nm}(\cos\vartheta)\cos m\lambda \quad Y_n(\vartheta, \lambda) = P_{nm}(\cos\vartheta)\sin m\lambda \quad (5.11)$$

are solutions of differential Equation 5.6. These solutions are linear, so any linear combination of functions (Equation 5.11).

$$Y_n(\vartheta, \lambda) = \sum_{m=0}^n [a_{nm}P_{nm}(\cos\vartheta)\cos m\lambda + b_{nm}P_{nm}(\cos\vartheta)\sin m\lambda] \quad (5.12)$$

where a_{nm} and b_{nm} are arbitrary coefficients. Substituting just obtained relations in Equation 5.7, we get solutions of the Laplace equation for interior and exterior of the sphere:

$$V_i(r, \vartheta, \lambda) = \sum_{n=0}^{\infty} r^n \sum_{m=0}^n [a_{nm}P_{nm}(\cos\vartheta)\cos m\lambda + b_{nm}P_{nm}(\cos\vartheta)\sin m\lambda] \quad (5.13)$$

$$V_e(r, \vartheta, \lambda) = \sum_{n=0}^{\infty} \frac{1}{r^{n+1}} \sum_{m=0}^n [a_{nm}P_{nm}(\cos\vartheta)\cos m\lambda + b_{nm}P_{nm}(\cos\vartheta)\sin m\lambda] \quad (5.14)$$

For Legendre's functions P_{nm} , n is called a degree and m is called the order of this function. Here Legendre's function is:

$$P_{nm}(t) = (1+x)^n = \frac{1}{2^n n!} (1-t^2)^{\frac{m}{2}} \frac{d^{n+m}}{dt^{n+m}} (1-t^2)^n$$

Figure 5.2 illustrates an example of Legendre functions.

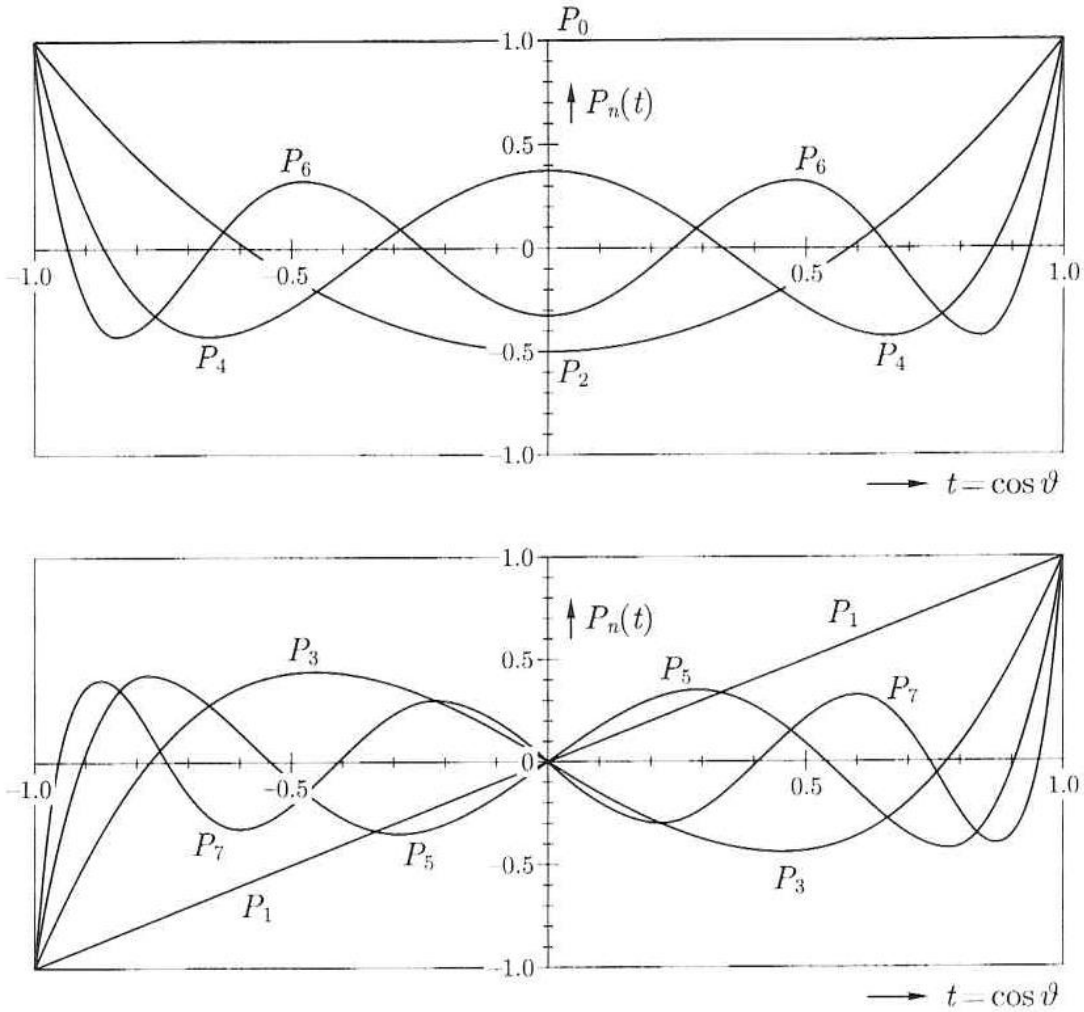


Figure 5.2 Legendre's polynomials as function of $t = \cos\vartheta$. Top: n is even; Bottom: n is odd (Hofmann-Wellenhof & Moritz, 2006).

Now, any arbitrary function on the surface of the sphere can be expanded into series of spherical harmonics

$$f(\vartheta, \lambda) = \sum_{n=0}^{\infty} Y_n(\vartheta, \lambda) = \sum_{n=0}^{\infty} \sum_{m=0}^n [a_{nm} R_{nm}(\vartheta, \lambda) + b_{nm} S_{nm}(\vartheta, \lambda)] \quad (5.15)$$

Here we introduce new abbreviations

$$R_{nm}(\vartheta, \lambda) = P_{nm}(\cos\vartheta) \cos m\lambda$$

$$S_{nm}(\vartheta, \lambda) = P_{nm}(\cos\vartheta)\sin m\lambda$$

It essential that just introduced functions are orthogonal, which means that the integral over the unit sphere of the product of two different functions is equal to zero:

$$\iint_{\sigma} R_{nm}(\vartheta, \lambda)S_{sr}(\vartheta, \lambda)d\sigma = 0,$$

for any combination of m , n , s , and r , as well as

$$\iint_{\sigma} S_{nm}(\vartheta, \lambda)S_{sr}(\vartheta, \lambda)d\sigma = 0 \quad \iint_{\sigma} R_{nm}(\vartheta, \lambda)R_{sr}(\vartheta, \lambda)d\sigma = 0$$

for any $s \neq n$ or $r \neq m$ or both.

This gives us a tool to solve the Dirichlet problem with given boundary function F on the sphere surface. Suppose that this function F is not known precisely, it means that we have an error between what is a known to us function F and what is real unknown function H . Let us denote the maximum error by ε :

$$\max_{\chi} |F(\chi) - H(\chi)| < \varepsilon \quad (5.16)$$

where χ is a point on the surface of the given sphere. Geometrically it means that the distance between functions is measured by maximum distance between them. Let us assume for simplicity that we have a unit sphere, in this case we can present function F on the unit sphere into a form of spherical harmonics

$$V(1, \vartheta, \lambda) = \sum_0^{\infty} Y_n(\vartheta, \lambda)$$

and

$$Y_n(\vartheta, \lambda) = \sum_{m=0}^n [a_{nm}P_{nm}(\cos\vartheta)\cos m\lambda + b_{nm}P_{nm}(\cos\vartheta)\sin m\lambda]$$

Here we can determine coefficients by knowing surface function F and by using the following formulas:

$$a_{n0} = \frac{2n+1}{4\pi} \iint_{\sigma} F(\vartheta, \lambda) P_{n0}(\vartheta, \lambda) d\sigma$$

$$a_{nm} = \frac{2n+1}{2\pi} \frac{(n-m)!}{(n+m)!} \iint_{\sigma} F(\vartheta, \lambda) R_{nm}(\vartheta, \lambda) d\sigma$$

$$b_{nm} = \frac{2n+1}{2\pi} \frac{(n-m)!}{(n+m)!} \iint_{\sigma} F(\vartheta, \lambda) S_{nm}(\vartheta, \lambda) d\sigma$$

We understand that replacing F by $V(1, \vartheta, \lambda)$ in Equation 5.16, then we obtain the following inequality:

$$\max_{\chi} |V(1, \vartheta, \lambda) - H(\chi)| < \varepsilon$$

The exterior solution for the Dirichlet problem when $r > 1$ is

$$V(r, \vartheta, \lambda) = \sum_{n=0}^{\infty} \frac{Y_n(\vartheta, \lambda)}{r^{n+1}}$$

So, for any exterior point with spherical coordinates (r, ϑ, λ) , where $r > 1$, we have, as a worst case scenario, evaluation for the gravity potential error.

$$\max_{\chi} |V(r, \vartheta, \lambda) - V_{real}(r, \vartheta, \lambda)| < \frac{\varepsilon}{r} \quad (5.17)$$

The further from the surface axial location of the point with coordinates (r, ϑ, λ) is, the smaller the error in estimation of the potential.

Now let us suppose that the surface-boundary is not known precisely, it means that there is some possible error not exceeding value $\delta > 0$ in meters along this boundary. It is well known that if object moves along any plumb line distance δ then the value of gravity potential changes by 0.308δ mgal. Our next step is to replace errors in boundary values and errors in boundary itself at any point χ of the surface by only boundary errors at the same point. We can achieve this goal by combining error ε at the boundary and error 0.03086δ to the shift to boundary as the aggregate error in the form $\varepsilon + 0.308\delta$. It is well known that in the maximum metric the total maximum error is not greater than sum of maximum errors. Now we can give the final estimation of the greatest error in the gravity potential determination outside of the surface of the planet:

$$\max_{\sigma} |V(r, \vartheta, \lambda) - V_{real}(r, \vartheta, \lambda)| < \frac{\varepsilon + 0.308\delta}{r}$$

Remarks

The above problem of evaluation of gravity potential errors was set up at U.S. National Geodetic Survey during personal conversation by Dr. Alexey Sadovski.

References

Fabes, E. B., Lewis, J. E., & Riviere, N. M. (1977). Boundary value problems for the Navier-Stokes equations. *American Journal of Mathematics*, 99 (3), 626-668.

Folland, G. B. (1976). Introduction to partial differential equations. Preliminary informal notes of university courses and seminars in mathematics. *Mathematical Notes. Princeton University Press, Princeton, NJ.*

Heck, B. (1997). Formulation and linearization of boundary value problems: from observables to a mathematical model. In *Geodetic Boundary Value Problems in View of the One Centimeter Geoid* (pp. 119-160). Springer Berlin Heidelberg.

Hofmann-Wellenhof, B., & Moritz, H. (2006). *Physical geodesy* (2nd ed.). New York: Springer Wien.

Chapter 6: Sea Level Rise and the Geoid: A Factor Analysis Approach

6.1 Introduction

Most scientists consider climate change to be a serious environmental threat (IPCC, 2007). Climate change, whether from natural or anthropogenic causes, is evidenced by increased rates of sea level rise, increased atmospheric and ocean temperatures, changes to precipitation amounts and patterns, a possible subtropical desert expansion (Lu et al., 2007), thermal expansion of ocean water, and glaciers melting. Other effects of climate change are evidenced by severe weather events including heat waves, droughts (Dai, 2011), and heavy rainfall. Some potential effects of climate change include species extinctions due to shifting temperature regimes, the threat to food security because of extreme weather patterns (Battisti & Naylor, 2009), and habitat losses due to coastal inundation due to higher rates of sea level rise.

Sea level rise demands more attention in coastal areas. One reason is that about 10% of the world's population lives in low-lying coastal areas with elevations less than 10 meters above current mean sea level (FitzGerald et al., 2008). The current global rate of sea level rise is nearly 3.0 mm/year (Rahmstorf, 2007a; Nicholls & Cazenave, 2010). Satellite observations show the rate of sea level rise varies across the globe (<http://sealevel.colorado.edu/content/regional-sea-level-time-series>). Thus, the study of sea level rise is an important component of earth science research.

Cartographers and geodesists, those who study the measurement of the size and shape of the earth, are interested in sea level as an elevation datum. This datum is called the geoid, which is defined as the equipotential gravity surface of the Earth, and theoretically best fits global mean sea level in ocean areas (Hofmann-Wellenhof & Moritz, 2006). Hence, the rate of change in

mean sea level directly affects changes to the geoid and the elevation datum used as the reference for topographic mapping.

Many methods have been used in sea level rise modeling. These methods can be divided into two categories: physical models, based on the conservation of mass (global water mass and ice mass measurements), and semi-empirical models, studying measured rates of change of sea level and measured changes in global temperatures along with the error estimates of measurements to predict future trends (Rahmstorf, 2012). These two approaches are complementary. For example, no one really understands the dynamics of each and every glacier, so it is quite difficult to calculate melting glaciers from physical models, hence the use of semi-empirical methods described in the majority of studies of sea level rise. This paper introduces a different approach by using factor analysis of regional sea level rates of change as a statistical analysis tool. Instead of answering the question of how much and how fast sea levels are changing, this paper computes and discusses which mathematical factor statistically affects sea level rates of change and seeks patterns to explain spatial correlation. The paper also seeks to hypothesize that any insights into the factors influencing sea level change also apply to the changes to the geoid.

6.2 Background

There are two types of sea level rise. One is called global sea level rise. The cause of global sea level rise is basically rising temperatures. According to Roemmich (1992), thermal expansion of seawater and melted glaciers are increasing results from warming. Additionally, a 2009 EPA report (Titus & Anderson, 2009) said that potential changes in polar ice sheet flow may be another factor that causes global sea level rise (Williams et al., 2009). The Intergovernmental Panel on Climate Change (IPCC) reported that sea levels have risen

approximately 4.8~8.8 inches (12~22 cm) around the world during last century (IPCC, 2007). Global sea levels rose at an average rate of 1.8 mm per year between 1961 and 2003 (1.3~2.3 mm), and there was a much faster rate between 1993 and 2003 (Williams et al., 2009). The IPCC (2007) estimated that the global mean sea level will rise by 7.2~23.6 inches (18~59 cm) by 2100 (Figure 6.1). The CU Sea Level Research Group (SLRG) at the University of Colorado defines the global mean sea level as “the area-weighted mean of all of the sea surface height anomalies measured by the altimeter in a single, 10-day satellite track repeat cycle”. The SLRG at CU also argues that the global mean sea level can be thought of as the eustatic sea level, which represents the level if all the water in the ocean is based on a single basin.

Sea Level Rise Projections to 2100

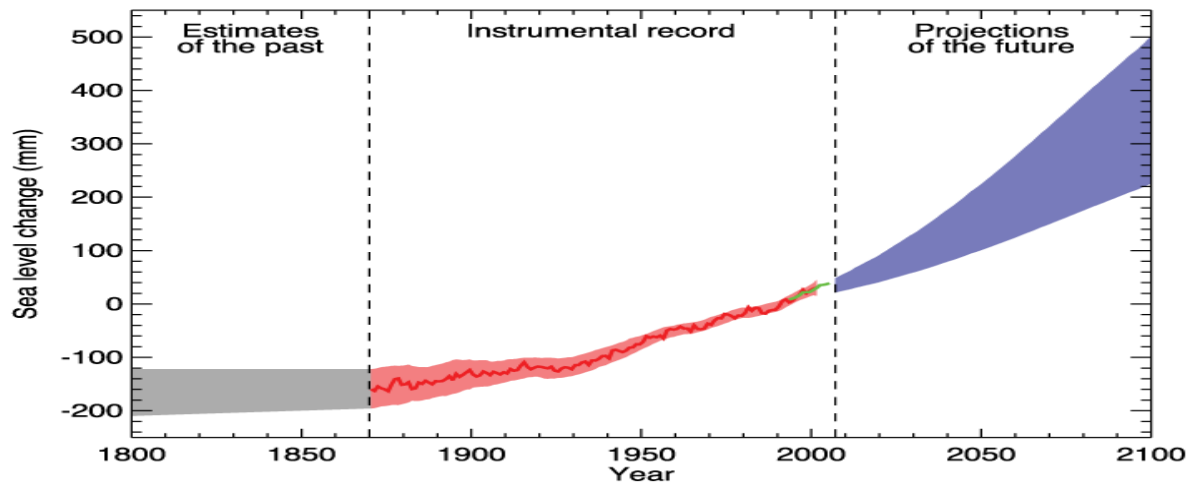


Figure 6.1 Past and projected global average sea level. The gray shaded area shows the estimates of sea level change from 1800 to 1870 when measurements are not available. The red line is a reconstruction of sea level change measured by tide gauges with the surrounding shaded area depicting the uncertainty. The green line shows sea level change as measured by satellite. The purple shaded area represents the range of model projections for a medium growth emissions scenario (IPCC SRES A1B). Source: IPCC (2007).

Another type is local sea level rise, often known as relative sea level rise, which is very important when studying coastal areas. It refers to the change in sea levels relative to the

elevation of the land, and relative sea level rise includes the effect of both global sea level rise and vertical movements of the land (Williams et al., 2009). For instance, relative sea level rise along the coastal areas of the Gulf of Mexico is caused by the global rise in ocean levels and land subsidence resulting from natural and human-induced changes (Montagna et al., 2007). From a natural view, the coastal plain was built by deposited, estuarine, coastal, and sediments. The thickness of mud and sand is compressing under their own weight at a rate of about 0.05 mm/year (Paine, 1993). In addition, land subsidence is a human-induced result from extraction of subsurface fluids (i.e. oil, gas, water). Montagna et al. (2007) suggested that the highest rates of land subsidence are correlated with oil, gas, and groundwater withdrawal in South Texas coasts; however, Dokka (2006) proposed that a significant cause of subsidence is faulting in the Gulf of Mexico.

Figure 6.2 (Montagna et al., 2007) visually shows how a rise of 2, 4, and 6 meters respectively in sea level would result in inundations of the Corpus Christi Bay area. With a rise of less than 4 meters, barrier islands that exist today would be completely gone. With only a 2-meter rise from current sea level, the lower Nueces Delta would be submerged, and the entire delta would be submerged with a 6 meters rise of sea level. This figure does not give us a realistic view or shape for future shorelines because it did not include variable factors (i.e. waves, currents, and human activities) in this case. But just by this view, there would be massive losses of marsh habitats in the bays. This is why studying and understanding what kind of factors lead to sea level rise is imperative.

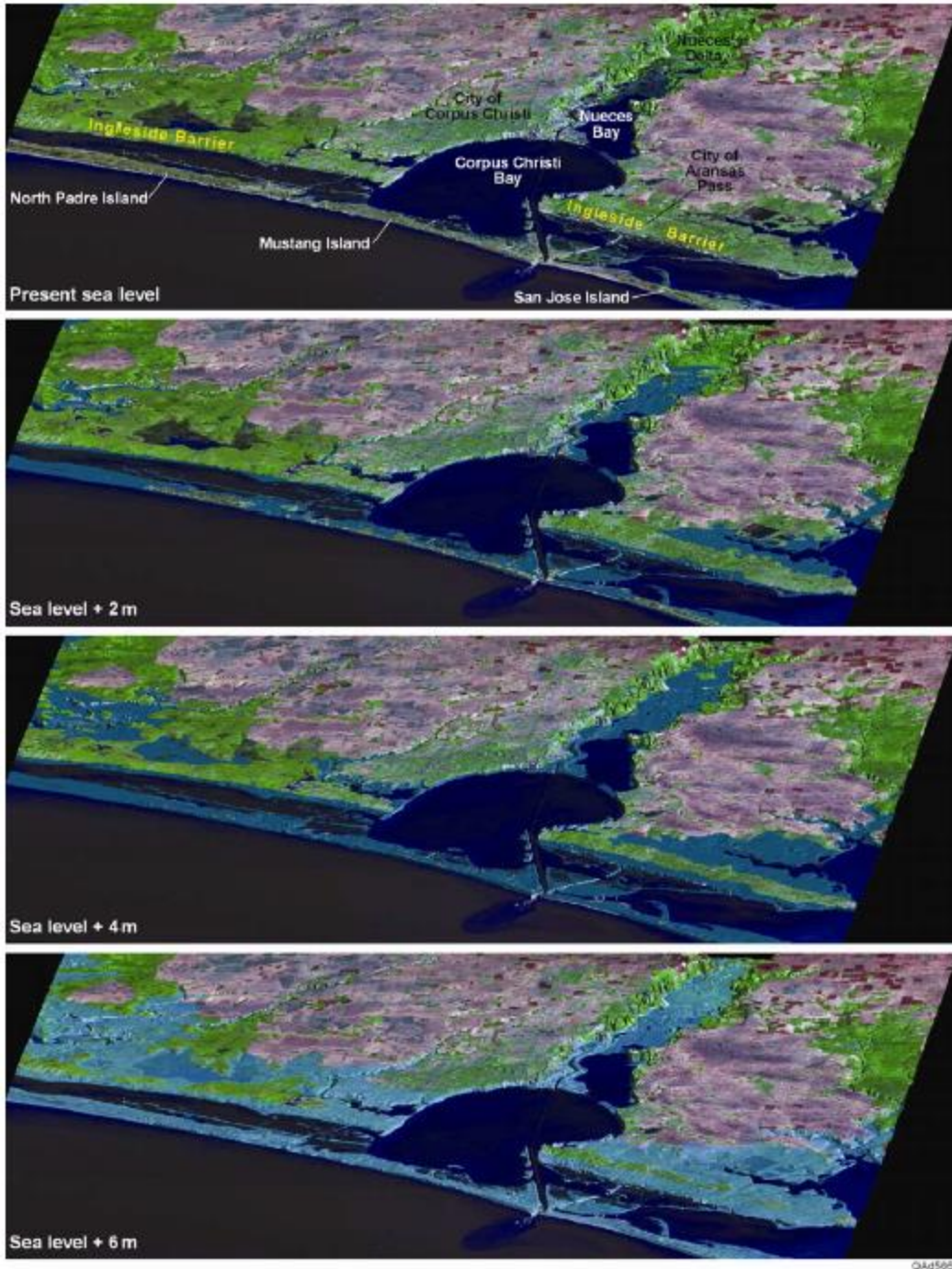


Figure 6.2 Perspective view of inundation of the Corpus Christi Bay area by sea level rise (Montagna et al., 2007).

6.3 Data

Datasets [msl_ib(mm) #version_2012_rel2] were downloaded from the University of Colorado Sea level research Group website (CU Sea Level Research Group, 2013; Figure 6.3). The sea level data was used in this chapter recorded from 1992 to 2011(Figure 6.4). These datasets did not correct GIA, but applied the inverted barometer (IB) approach, which is the traditional static model, and also included seasonal signals.

These downloaded datasets were fixed by using a running average (also known as a moving average) in this study. The cumulative running average (CRA) is typically the unweighted average of the sequence of i mean sea level values x_1, x_2, \dots, x_i up to 2011:

$$CRA_i = \frac{x_1 + x_2 + \dots + x_i}{i}.$$

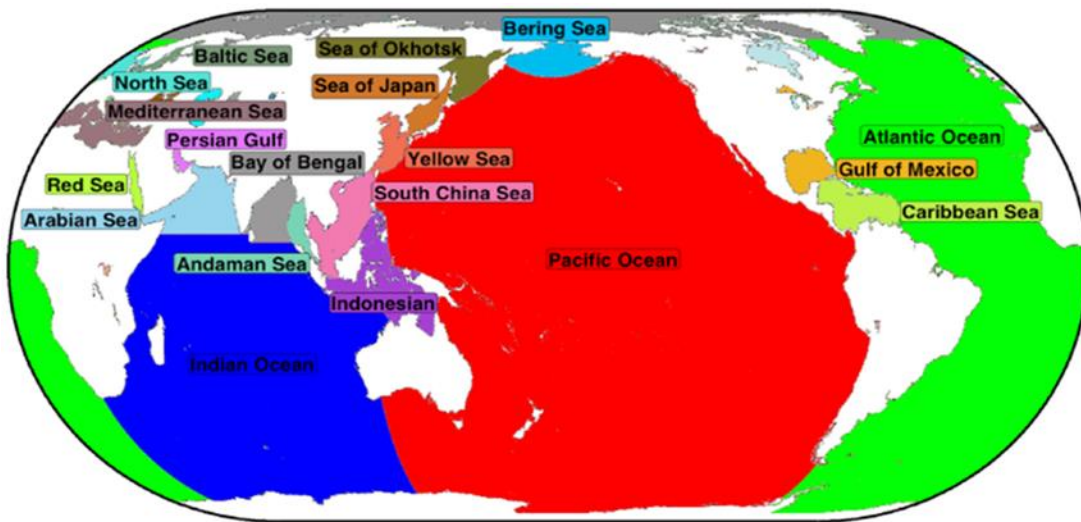


Figure 6.3: Data from each region represented in the world map (http://ibis.grdl.noaa.gov/SAT/SeaLevelRise/LSA_SLR_timeseries_regional.php).

In principle, a prediction lies on the original regression line, and an increase in the strength of correlation (either positive or negative) is expected. If it is a good prediction, the

correlation coefficient after the extra order pair added to the data should be stronger than the original coefficient. Unfortunately, this is not likely to happen due to the mutative trend of coefficient. A running average method uses the i pairs of data to calculate the regression equation and correlation coefficient, and increases i by 1 each step, and repeats the process until reaching the suitable number of predictions. Therefore, there is a higher estimate from the mutative trend, and the prediction will be much smoother (Figures 6.5 and 6.6).

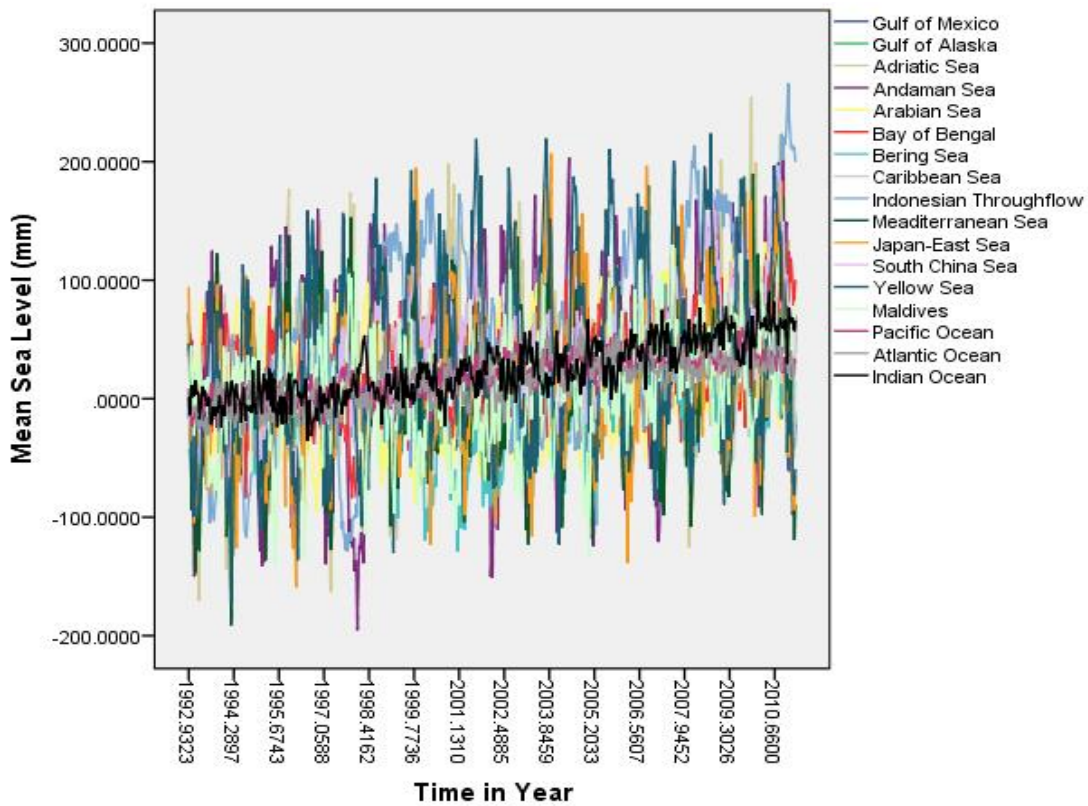


Figure 6.4 Mean sea level dataset from 1992 to 2011.

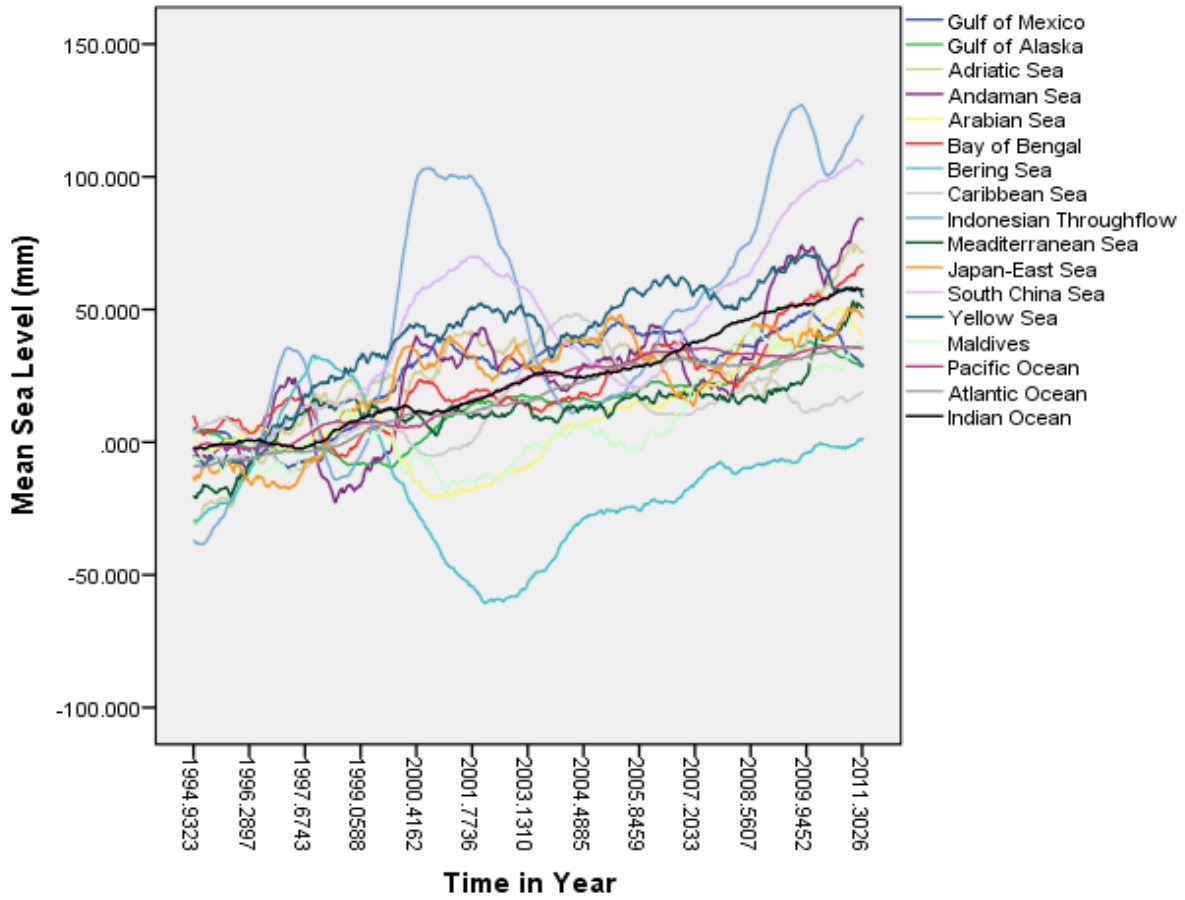


Figure 6.5 Sea level variations: 2 years running averages.

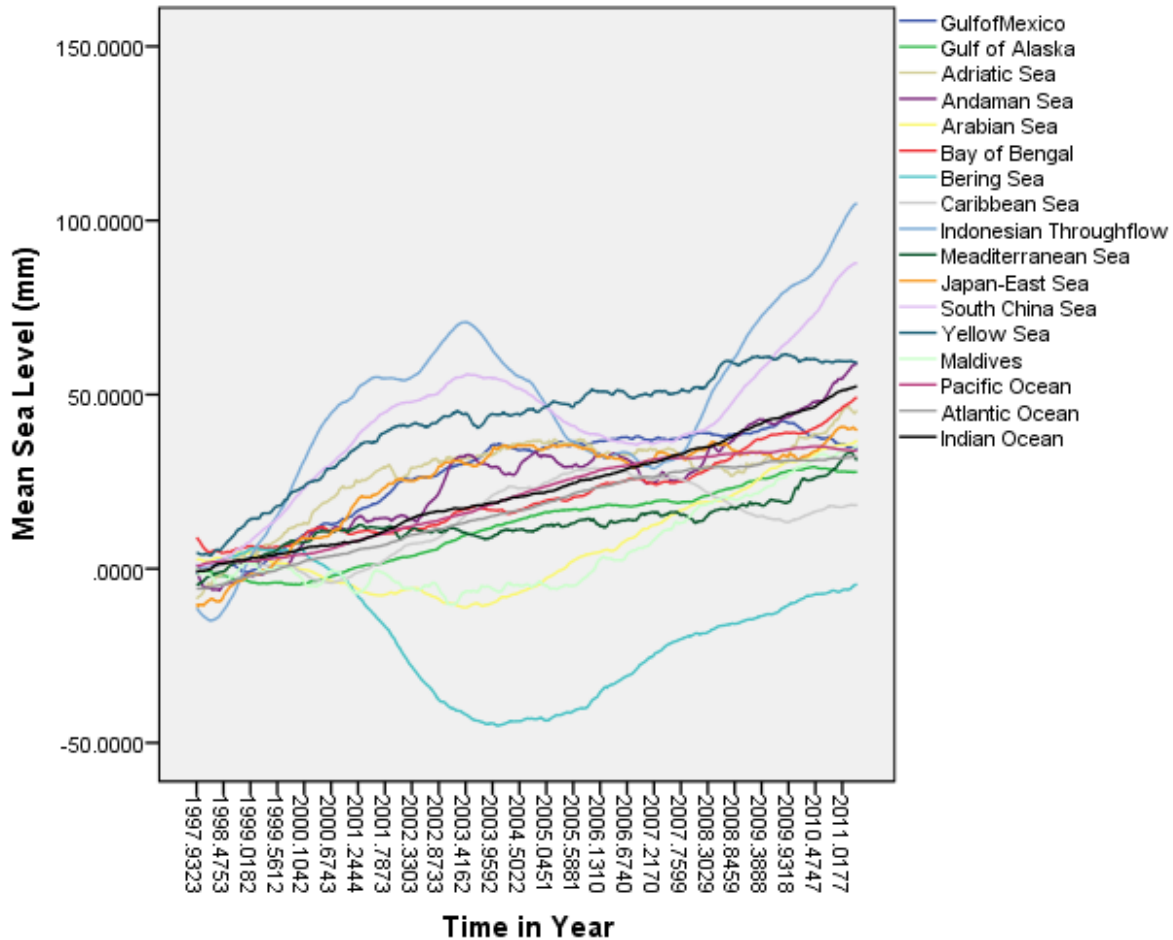


Figure 6.6 Sea level variations: 5 years running averages.

6.4 Method

Using a running average of mean sea level data, the factor analysis approach was applied in this study. Factor analysis is designed to reduce the multi-dimension of space of variables to two or three dimensional space of factors that explain majority of variation of initial data. Firstly, the correlation matrix was obtained by using IBM SPSS Statistics 20. The extraction method used principal component analysis, and the rotation method used varimax with Kaiser Normalization. Then the four criteria-eigenvalue, variance, scree plot and residuals-were tested. Table 6.1 represents the communalities, and it indicates that all variables are $>.9$. Thus, this

analysis is fairly reliable. Finally, the number of factors to be retained was determined by eigenvalues. Since components with eigenvalues greater than 1 should be retained, the first three components satisfied this criterion. The total variance of the first three components is 97.748% (Table 6.2). However, if we take a careful look at the initial analysis, only the first component was strong enough to be retained. In this case, a principal component analysis was conducted to keep three components and utilize the varimax rotation. Inclusion of two components increases the model fit, and three components are fairly strong to be retained. After rotation, the first component accounted for 35.237%, the second for 32.655%, and the third for 29.856%. The screen plot (Figure 6.7) was then evaluated and shows that after component 3, the eigenvalues level off. The process of analysis for determining the appropriate number of components to retain was quite reliable according to the four criteria.

	Initial	Extraction
Gulf of Mexico	1.000	.976
Gulf of Alaska	1.000	.981
Adriatic Sea	1.000	.953
Andaman Sea	1.000	.967
Arabian Sea	1.000	.994
Bay of Bengal	1.000	.985
Bering Sea	1.000	.973
Caribbean Sea	1.000	.970
Indonesian Throughflow	1.000	.986
Mediterranean Sea	1.000	.944
Japan-East Sea	1.000	.981
South China Sea	1.000	.977
Yellow Sea	1.000	.963
Maldives	1.000	.983
Pacific Ocean	1.000	.996
Atlantic Ocean	1.000	.991
Indian Ocean	1.000	.997

Table 6.1 Communalities of mean sea level.

Component	Initial Eigenvalues			Extraction Sums of Squared Loadings			Rotation Sums of Squared Loadings		
	Total	% of Variance	Cumulative %	Total	% of Variance	Cumulative %	Total	% of Variance	Cumulative %
1	12.872	75.717	75.717	12.872	75.717	75.717	5.990	35.237	35.237
2	2.560	15.058	90.775	2.560	15.058	90.775	5.551	32.655	67.892
3	1.185	6.973	97.748	1.185	6.973	97.748	5.076	29.856	97.748
4	.162	.954	98.702						
5	.118	.694	99.396						
6	.038	.224	99.620						
7	.022	.132	99.752						
8	.011	.064	99.816						
9	.009	.052	99.869						
10	.007	.043	99.912						
11	.005	.028	99.940						
12	.004	.024	99.964						
13	.003	.018	99.982						
14	.001	.009	99.991						
15	.001	.007	99.998						
16	.000	.002	100.000						
17	6.747E-005	.000	100.000						

Table 6.2 Table of total variance for three components solution.

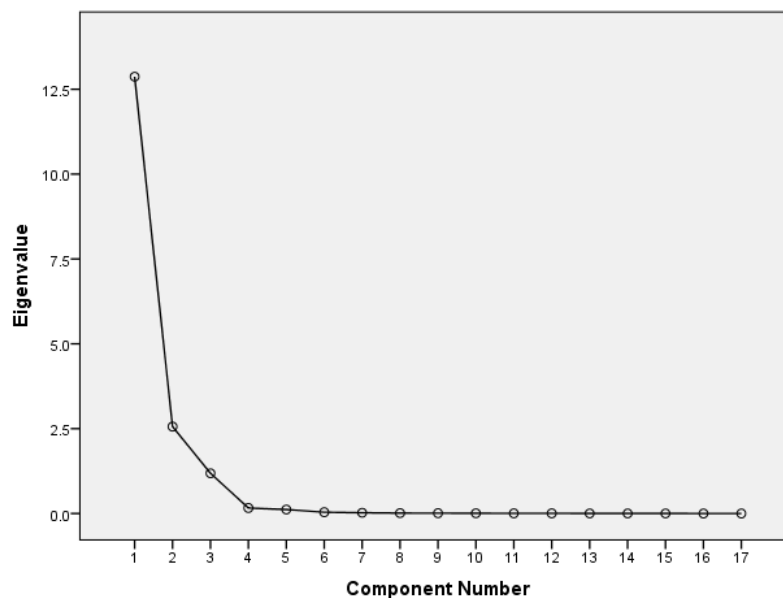


Figure 6.7 Scree plot.

6.5 Results

The last step was to interpret each retained component. Table 6.3 indicates the factor loadings for the rotated components. Only the factor loadings over .7 were concerned in this

study. Component 1 consisted of four of seventeen variables: the Arabian Sea, the Bay of Bengal, the Maldives, and the Indian Ocean. These variables had positive loadings. The Arabian Sea and Bay of Bengal are marginal seas of the Indian Ocean. The Maldives Republic is the lowest country in the world. According to EGM08 (Earth Gravity Model of 2008) map, the geoid of these four variables is much lower than the others. Thus, component 1 addressed the geoid. Component 2 included the Gulf of Mexico, the Caribbean Sea, the East Sea (also known as the Sea of Japan), and the Bering Sea. Among of these four variables, the loading of the Bering Sea was negative. The Bering Sea is marginal sea of the Pacific Ocean, and the circulation of this area is also affected by the Arctic Ocean. The currents of the Gulf of Mexico, the Caribbean Sea and the East Sea are warmer current. This second component represented circulation (especially indicate current). Component 3's interpretation is in question. Indonesian Through-flow has a long-term history of tectonic changes. These changes were not just zone collision (i.e., Asian-Australia collision zone) and mountain building, but also included basins extensions and new ocean basins' formation in eastern Indonesia (Kuhnt, W. et al., 2004). The Adriatic Sea is located in the collision zone between the African and the European plates (Favali, P. et al., 1993). So, component 3 may be influenced by the tectonic changes. Additionally, there is an attention that the areas with the loadings of the two components which were relatively high are mostly the places where oil spills have occurred, but this hypothesis has not been studied in this research.

	Component		
	1	2	3
Gulf of Mexico	.372	.776	.484
Gulf of Alaska	.691	.603	.373
Adriatic Sea	.181	.648	.708
Andaman Sea	.523	.525	.646
Arabian Sea	.988	.020	.127
Bay of Bengal	.802	.354	.465
Bering Sea	.422	-.849	-.272
Caribbean Sea	.265	.947	.068
Indonesian Throughflow	.251	.148	.949
Mediterranean Sea	.645	.249	.683
Japan-East Sea	.235	.732	.624
South China Sea	.309	.310	.886
Yellow Sea	.470	.609	.609
Maldives	.952	-.003	.276
Pacific Ocean	.662	.667	.335
Atlantic Ocean	.654	.635	.399
Indian Ocean	.758	.458	.460

Table 6.3 Factor loadings for rotated component matrix.

6.6 Discussion

The main goal of factor analysis is to simplify several inter-correlated measures orderly (Burt, 1940; Child, 2006). If using one word to describe these mathematical procedures used for factor analysis is “generalization”, which called factor in this chapter. Factors explain common variance among variables. The statistical method of factor analysis is designed to reduce data by grouping variables that show a common pattern. Principal components analysis (PCA) is most commonly chosen to use in extraction procedure. PCA evaluated all sources of variability for each variable during the procedure. However, there are always some things we are not able to determine with certainty. Therefore, it is easy to apply the methodology precisely, but interpretation varies among interdisciplinary branches of science.

Total Variance Explained								
Component	Initial Eigenvalues			Extraction Sums of Squared Loadings			Rotation Sums of Squared Loadings	
	Total	% of Variance	Cumulative%	Total	% of Variance	Cumulative%	Total	% of Variance
1	8.742	79.5	79.5	8.742	79.5	79.5	8.093	73.6
2	1.534	13.9	93.4	1.534	13.9	93.4	2.183	19.8
3	0.334	3.0	96.5					
4	0.145	1.3	97.8					
5	0.116	1.0	98.8					
6	0.076	0.7	99.5					
7	0.029	0.3	99.8					
8	0.012	0.1	99.9					
9	0.005	0.01	99.9					
10	0.003	0.03	99.97					
11	0.003	0.03	100					

Extraction Method: Principal Component Analysis

Table 6.4 Table of total variance explained (Sadovski, A. et al., 2010).

Rotated Component Matrix ^a		
	Component	
	1	2
Packer Channel	0.986	0.094
Bob Hall Pier	0.734	0.64
Rockport	0.971	0.099
Galveston Pleasure Pier	0.993	0.049
Galveston Pier 21	0.97	-0.022
Freeport	0.944	0.091
Rincon del San Jose	0.905	0.391
Port Aransas	0.906	0.335
Sabine Pass	0.881	0.428
Port Isabel	0.158	-0.928
S. Padre Island Coast Guard Sta.	0.615	0.659

Extraction Method: Principal Component Analysis
 Rotation Method: Varimax with Kaiser Normalization.
 a. Rotation converged in 3 iterations.

Table 6.5 Factor loading for rotated component matrix (Sadovski, A. et al., 2010).

According to a poster presentation by Sadovski et al. (2010) (Tables 6.4 and 6.5), many factors of sea level rise are unexplained in the analysis of Texas coast, but more factors are

identifiable in the pattern of regional areas. In studying regional and local areas, different kinds of datasets (i.e. wind data, salinity data, temperature data, etc.) should be added. This will provide a more precise indication of which factors have a great impact in local areas. So far in this poster presentation the first of two main factors was interpreted as a global sea level rise while the second one as a local subsidence of the land in the coastal areas.

The study of the mean sea level should not just focus on global, but regional or local areas, as well. Studying global sea level changes is helpful for finding and learning about changing patterns, but regional and local studies will reveal more specific factors that cause sea level rise. Knowing the patterns and factors which affect sea levels will result in more accurate predictions of changes along the coasts, and, ultimately, better means by which to plan for, or avoid, catastrophes due to inundation.

6.7 Acknowledgements

Thanks to CU Sea level Research Group at University of Colorado for open access to download regional sea level data (Available from: <http://sealevel.colorado.edu/content/regional-sea-level-time-series>). The regional sea level data [msl_ib(mm) #version_2012_rel2] was downloaded on April 24, 2012. Special thanks to Dr. Dallas Masters at Sea Level Research Group for communicating with me about data issues via emails between April 25, 2012 and May 30, 2013.

This chapter is in press in *International Journal on Mathematics: Theory and Applications* 20 (2): 65-80. Co-authors of this paper are Drs. Alexey Sadovski and Gary Jeffress.

6.8 Reference

- Battisti, D., & Naylor, R. (2009). Historical warnings of future food insecurity with unprecedented seasonal heat. *Science*, 323, 240-244.
- Burt, C. (1940). *The factors of the mind*. London: University of London Press.
- Child, D. (2006). *The essentials of factor analysis* (3rd ed.). London, New York: Continuum.
- CU Sea Level Research Group (2013). Altimeter-Derived Regional Sea Level Trends, 1993-2013. University of Colorado. Available from: <http://sealevel.colorado.edu>.
- Dai, A. (2011). Drought under global warming: A review. *Wiley Interdisciplinary Reviews: Climate Change*, 2 (1), 45-65.
- Dokka, R. (2006). Modern-day tectonic subsidence in coastal Louisiana. *Geology*, 34 (4), 281-284.
- Favali, P., Funiciello, R., Mattiotti, G., Mele, G., & Salvini, F. (1993). An active margin across the Adriatic sea (central Mediterranean sea). *Tectonophysics* 219 (1), 109-117.
- FitzGerald, D., Fenster, M., Argow, B., & Buynevich, I. (2008). Coastal impacts due to sea-level rise. *Annual Review of Earth and Planetary Science* 36, 601-647.
- Hofmann-Wellenhof, B., & Moritz, H. (2006). *Physical geodesy* (2nd ed.). New York: Springer Wien.
- IPCC (2007) "Climate change 2007: The physical science basis", in S. Solomon, D. Qin, M. Manning, Z. Chen, M. Marquis, K.B. Averyt, M. Tignor and H.L. Miller (Eds.) *Contribution of Working Group I to the Fourth Assessment Report of the*

Intergovernmental Panel on Climate Change. Cambridge, New York: Cambridge University Press.

- Kuhnt, W., Holbourn, A., Hall, R., Zuvela, M., & Käse, R. (2004). Neogene history of the Indonesian throughflow. In: P. Clift, P. Wang, W. Kuhnt and D. Hayes (Eds.) *Continent-Ocean Interactions within East Asian Marginal Seas, Geophysical Monograph Series, 149*, 299-320.
- Lu, J., Vecchi, G., & Reichler, T. (2007). Expansion of the Hadley cell under global warming. *Geophysical Research Letters*, 34 (6). L06805, doi:10.1029/2006GL028443.
- Montagna, P. A., Gibeaut, J. C., & Tunnell Jr, J. W. (2007). South Texas climate 2100: Coastal impacts. In: J. Norwine & K. John (Eds.) *South Texas Climate 2100: Problems and Prospects, Impacts and Implications*, 57-77.
- Nicholls, R., & Cazenave, A. (2010). Sea-level rise and its impact on coastal zones. *Science*, 328, 1517-1520.
- Paine, J. (1993). Subsidence of the Texas coast: Inferences from historical and the Pleistocene sea levels. *Tectonophysics*, 222, 445-458.
- Rahmstorf, S. (2007). A semi-empirical approach to projecting future sea-level rise. *Science*, 315, 368-370.
- Rahmstorf, S. (2012). Modeling sea level rise. *Nature Education Knowledge*, 3 (3), 4.
- Roemmich, D. (1992). Ocean warming and sea level rise along the southwest U.S. coast. *Science*, 257, 373-375.

- Sadovski, A., Jeffress, G., Tissort, P., Duff, S., & Ussery, S. (2010). Mean sea level-What are the recent changes along the Texas Gulf Coast? (poster). *Sea Level Rise Conference*, Corpus Christi, Texas, U.S.A.
- Smith, J. B., & Tirpak, D. A. (1989). *The potential effects of global climate change on the United States: Report to Congress*. U.S. Environmental Protection Agency, Office of Policy, Planning, and Evaluation, Office of Research and Development.
- Titus, J. G., & Anderson, K. E. (2009). *Coastal sensitivity to sea-level rise: A focus on the mid-Atlantic region* (Vol.4). Government Printing Office.
- Williams, S., Gutierrez, B., Titus, J., Gill, S., Cahoon, D., Thieler, E., & Anderson, K. (2009). Sea-level rise and its effects on the coast. In: Titus *et al.* *Coastal Sensitivity to Sea-Level Rise: A Focus on the Mid-Atlantic Region*, Synthesis and Assessment Product 4.1 Report by the U.S. Climate Change Science Program and the Subcommittee on Global Change Research: 11-23.

Chapter 7 The Geoid and Wetland Modeling: The Impact of the Geoid Precision on Wetlands Modeling

Another application of determination and evaluation of the geoid is that the geoid can be used as a basis for wetland migration modeling in response to sea level rise. The key parameters for modeling wetland migration are illustrated in Figure 7.1, among of which, the elevation is one of the important factors for sea level modeling and its impact on coastal wetlands systems (Marshes on the Move, 2011).

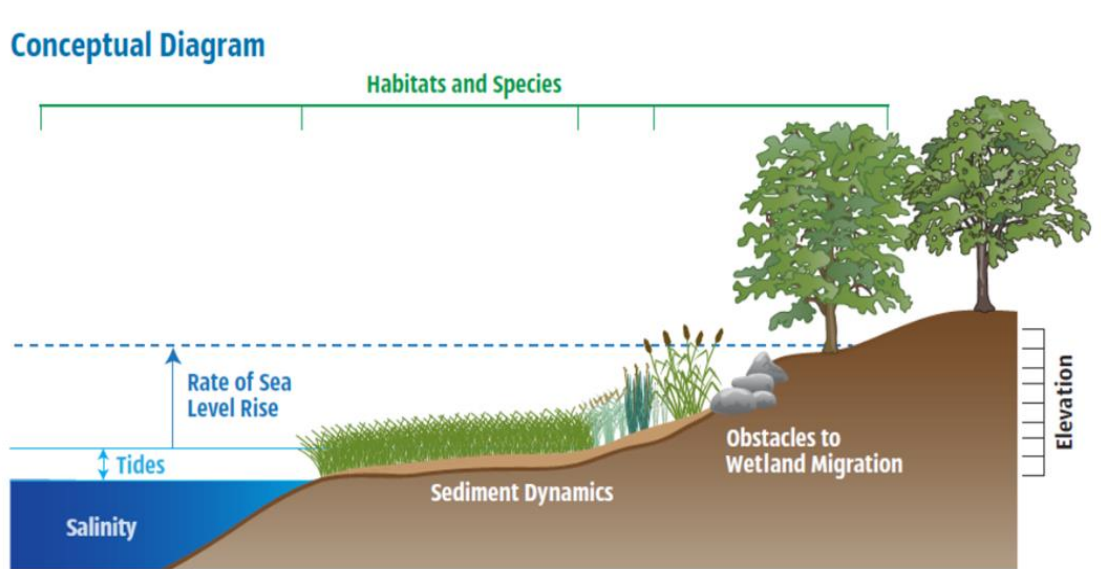


Figure 7.1 Illustration of Key Parameters for Wetland Migration Modeling (Marshes on the Move, 2011).

7.1 Background

According to *A to Z GIS: An illustrated dictionary of geographic information systems*, the elevation defines as “the vertical distance of a point or object above or below a reference surface or datum (generally mean sea level)”. However, elevations are measured either by leveling or by GPS receiver. GPS heights are referenced to the ellipsoid reference surface, and they are not

even linked to mean sea level. The geoid is defined as the equipotential gravity surface of the Earth, and theoretically best fits global mean sea level (Hofmann-Wellenhof & Moritz, 2006). Hence, elevations can be determined by using the geoid. Namely, using precise geoid can help to have more precise elevation values.

The coastal areas of the Gulf of Mexico have more than half of the coastal wetlands and seven major estuarine systems in the State of Texas alone. Barrier islands are parallel to the land along the coast. Between the land and barrier islands are lagoons, which open to a large primary bay. Coastal areas are important for many species. Coasts are also as the protection of human life and properties from shores. But there is a very high rate (25 square miles per year) of losing coastal lands in the Gulf of Mexico over the last 50 years (NOAA's Oil Spill Response, 2010). Also, the Gulf of Mexico as the highest amount of total proportion loss, the main caused factors are storms, erosion, subsidence, and global sea level rise (Coastal Wetland Reviews: Highlights).

Wetlands as part of coastal areas have great important functions. Mitsch and Gosselink (2007) mentioned two terms to describe wetlands, which are "the kidneys of the landscape" and "ecological supermarkets". "The kidneys of the landscape" means that wetlands have a function that is just like the function of organ kidneys. It can receive the water and waste of both natural and human sources from upstream. It also can store water and filter waste. Kidneys are very important to our human bodies, so are wetlands to environment. "Ecological supermarkets" gives a direct view of wetlands, which have a huge variety of flora and fauna. Wetlands are important habitats in both ecological and economical aspects.

There are some facts listed below (NOAA's state of the coast, 2011; Stedman & Dahl, 2008) which show how and how much wetland along the Gulf coasts we lost:

- “272 square miles of wetlands were converted to open water, bare land, agriculture, and developed area between 1996 and 2006 in the Gulf of Mexico coastal watershed area”.
- The area of wetlands is 31% of the total coastal watershed area of the Gulf of Mexico.
- “108 square miles of wetlands lost to development between 1996 and 2006 in the Gulf coastal watershed area”.
- In 2009, approximately 355 million pounds of shellfish harvest in coastal wetlands of Gulf of Mexico. Annual commercial value of these shellfish was 474 million dollars.
- After Hurricanes Rita and Katrina (2008), only in Louisiana coast, 198 square miles of marsh was lost to open water (Barras et al., 2003; Barras et al., 2008).
- “1/3 the amount of Louisiana’s coastal wetlands that will be lost by the year 2050 at current rates of loss”.

It is certain that coastal wetlands have been already experiencing submerging by rising in the sea level and associated with a high rate of loss. And it will be continued to lose areas in response to the future rates of sea-level rise and other factors (i.e. human activities). Many federal and state agencies are regulating with monitoring the environment along the Gulf of Mexico coastal areas. For example, Texas General Land Office (TGLO) is in charge of all Texas coastal submerged lands and Texas Water Development Board (TWDB) conducts research on freshwater inflow and impacts to Texas estuaries. It will be helpful if could provide information/data they needed (1) for mean sea level rise and a local geoid; (2) for determining mean water level changes in coastal wetlands; and, (3) for coastal areas management.

7.2 Data

Nueces Delta Elevation Control (NDEC) survey data was provided by The University of Texas Marine Science Institute. This NDEC data was updated on June 13, 2005. There are nine sites (Figure 7.2). Each site contains observation points as shown in Figure 7.3 for Site 1 which highlighted in Tourmaline Green in Figure 7.2. The observation points at each site are in matrix

form structure. For example, the upper three points shown in Figure 7.3 from right to left are (Transect 0, Point 1), (Transect 0, Point 3), and (Transect 0, Point 5).

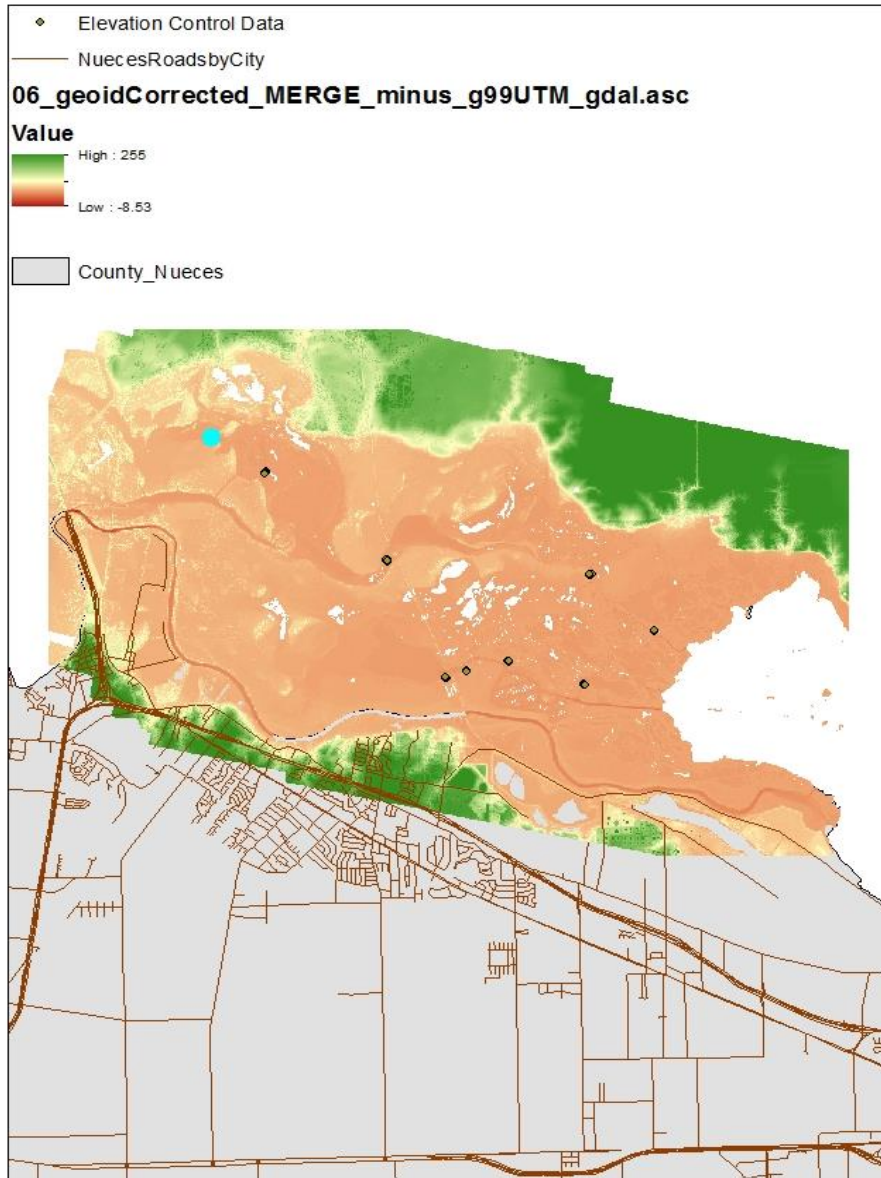


Figure 7.2 Nueces Delta Elevation Control data displaced as each site.

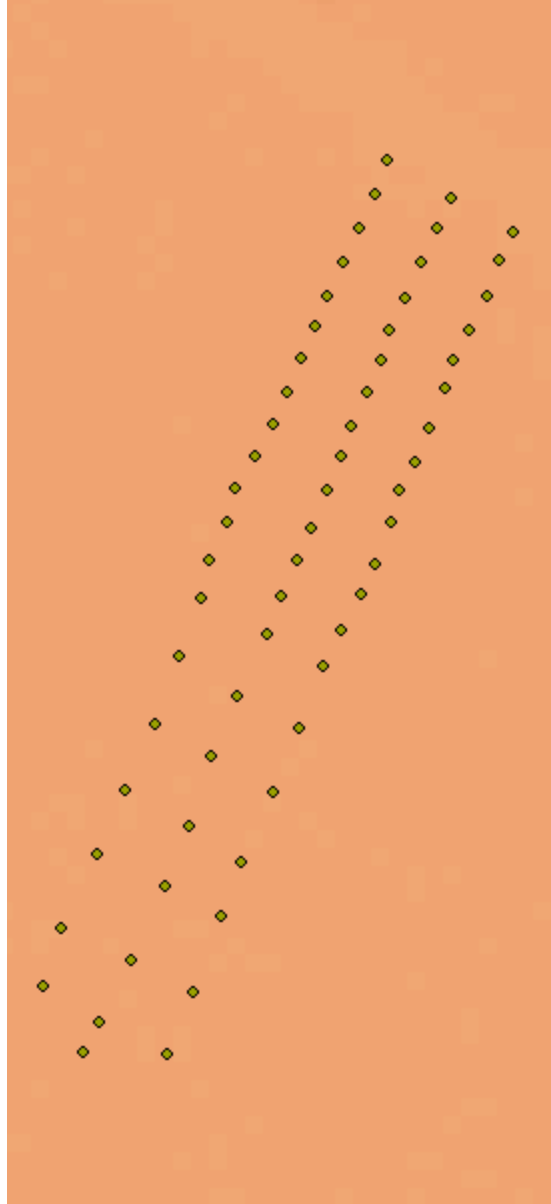


Figure 7.3 Nueces Delta Elevation Control locations in Site 1.

7.3 Method

The work did so far was to provide a predicted elevation surface by using the ordinary kriging method. The detail of the kriging method can be found in chapters 2 and 3 of this dissertation. The nugget of semivariogram in Figure 7.4 is 0.007 m^2 . Namely, the independent

error is small. The partial sill of semivariogram is approximately 0.009 m^2 , and the range is 4141.534 m . The semivariogram map is displayed in Figure 7.5.

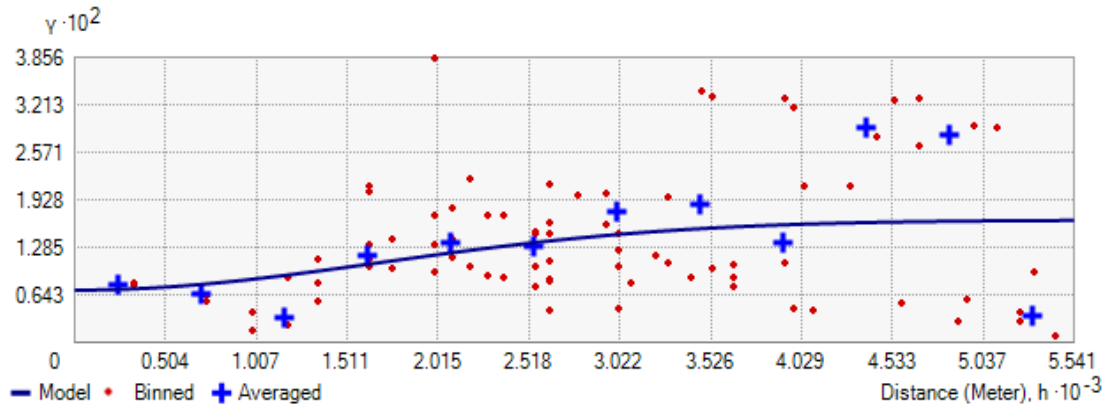


Figure 7.4 Semivariogram Model of the Ordinary Kriging. The averaged semivariogram values on the y-axis (in meter^2), and distance (or lag) on the x-axis (in meter). Binned values are shown as red dots, which are sorted the relative values between points based on their distances and directions and computed a value by square of the difference between the original values of points; Average values are shown as blue crosses, which are generated by binning semivariogram points; The model is shown as blue curve, which is fitted to average values. Model : $0.0070822 \cdot \text{Nugget} + 0.0094674 \cdot \text{Stable}(4141.5, 2)$.

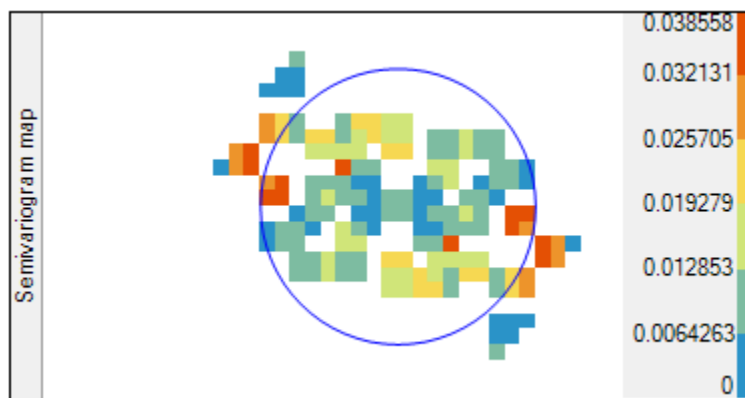


Figure 7.5 A semivariogram map. The color band shows semivariogram values with weights (unit in meter^2).

7.4 Result of the ordinary kriging method

The sample size of NDEC data is 407. The prediction errors mean is approximately 9.87×10^{-5} . The mean standardized is approximately -0.00077 , which is really close to zero. The RMS is around 0.85 and the standardized RMS is approximately 0.97. Average Standard Error is 0.09. The statistical result showed that the predicted of elevation surface is quite well. The predicted graph shown in Figure 7.6 revealed how well the known sample value was predicted compared to its actual value. The regression function in figure 7.6 is $f(X) = 0.475x + 0.262$. By visually analyzed the graph, the prediction of elevation surface is acceptable, but not as good as expected. The closer the regression function aligns with the reference line, the better the model will be.

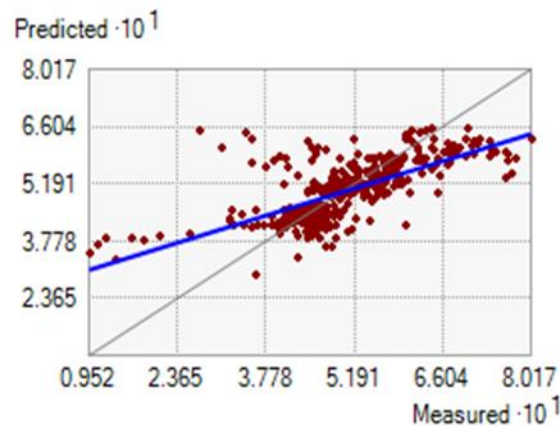


Figure 7.6 The predicted graph. The blue line represents the regression function, and the black line represents the reference line (unit in meter).

The error graph displayed in Figure 7.7 showed the difference between known elevation values and the predictions for these values. The error equation in Figure 7.7 is $y = -0.525x + 0.262$. Thus, the error of prediction is quite small. The standardized error graph (Figure 7.8) showed the error divided by the estimated kriging errors. The equation of the standardized error

is $y = -5.995x + 2.985$. The normal QQ plot of the standardized error (Figure 7.9) showed how closely the error aligns with the normal standard distribution. Overall, the prediction of elevation surface (Figure 7.10) is fairly good to be used in our future research.

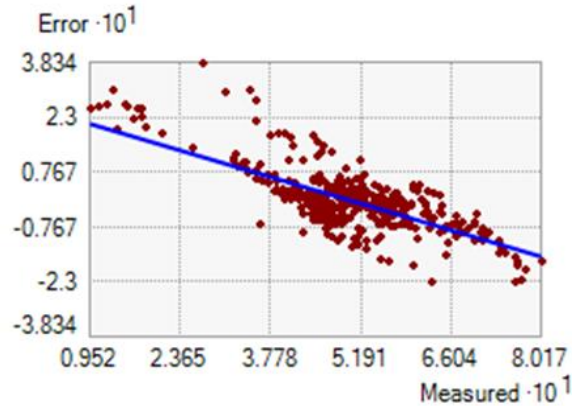


Figure 7.7 The error graph. The blue line represents the error equation (unit in meter).

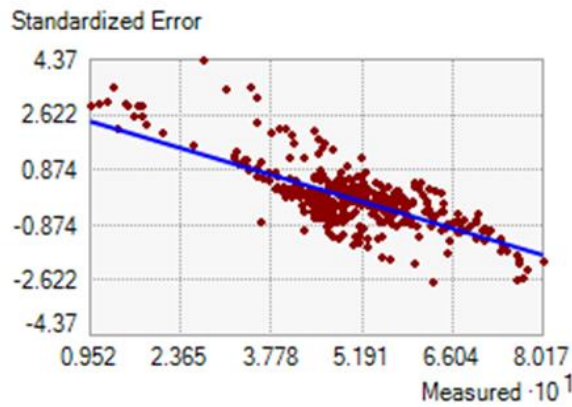


Figure 7.8 The standardized error graph. The blue line represents the standardized error equation (unit in meter).

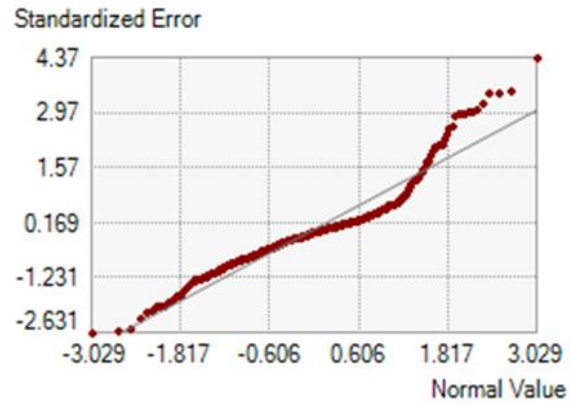
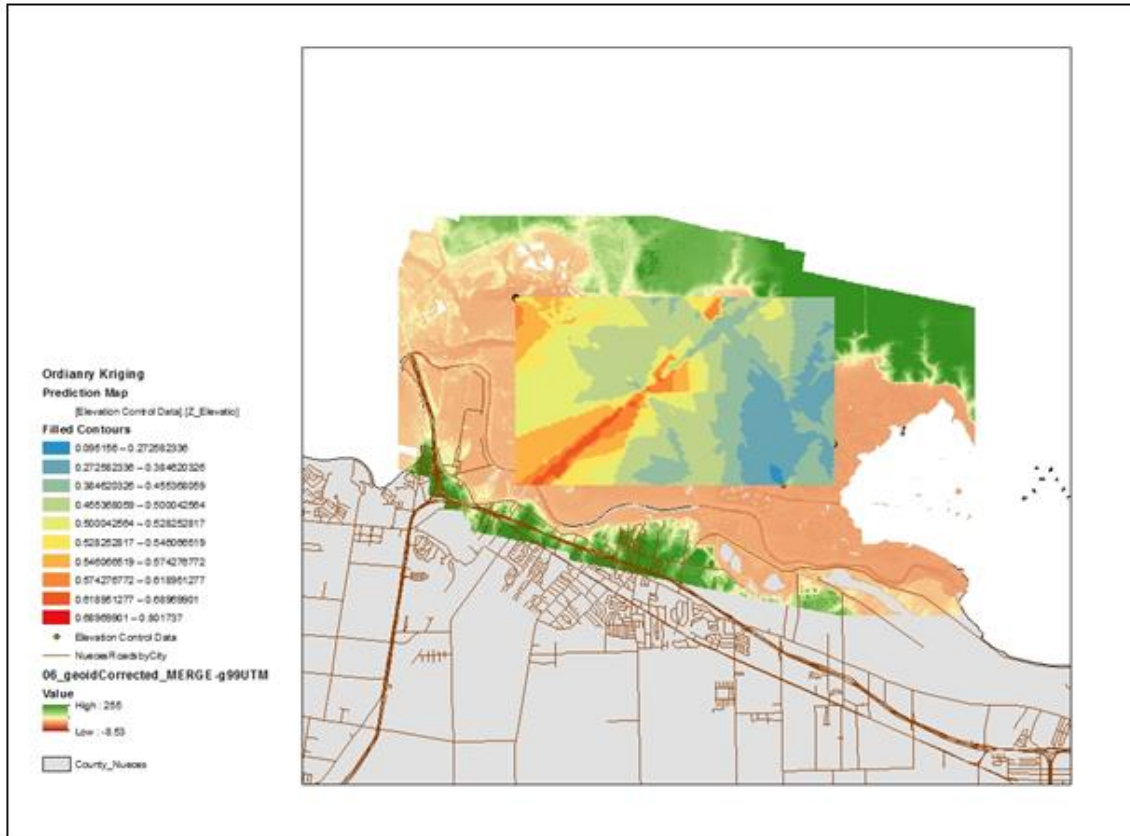


Figure 7.9 The normal QQ plot of the standardized error. The reference line is represented by the black line (unit in meter).



Symbol	Range
Blue	0.095156 - 0.272582336
Light Blue	0.272582336 - 0.384620326
Light Green	0.384620326 - 0.455368059
Green	0.455368059 - 0.500042564
Yellow-Green	0.500042564 - 0.528252817
Yellow	0.528252817 - 0.546066519
Orange	0.546066519 - 0.574276772
Dark Orange	0.574276772 - 0.618951277
Red-Orange	0.618951277 - 0.68969901
Red	0.68969901 - 0.801737

Figure 7.10 The ordinary kriging prediction elevation map with color symbol ranged within elevation values (unit in meter).

7.5 Discussion

The higher range of elevation values in predicted elevation surface (Figure 7.10) most happened close to or in water body of Nueces delta (Figure 7.11), which showed that the

prediction by using the ordinary kriging method is fairly reliable. Elevations are very important in restoration of marshes. Rasser's Ph.D. dissertation (2009) described vegetation distribution patterns for *Borrchia frutescens* and *Salicornia virginica* in lower Nueces delta. To give more precise configuration of marsh, especially the range of boundary values (i.e., the range of boundary values of tidal creek in Figure 7.12), there is a need to have precise elevation values; hence, there is a need to have precise local geoid. This will be one of the future research directions.

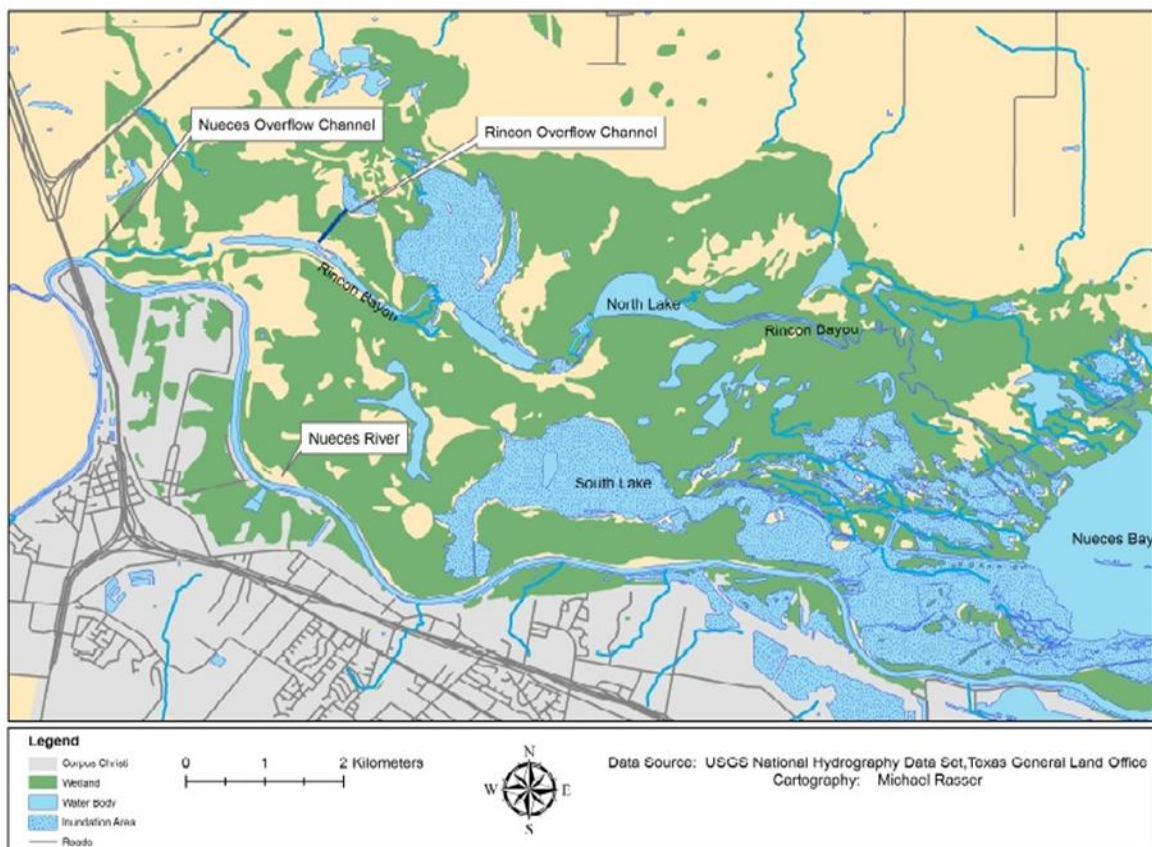


Figure 7.11 Map of Nueces Marsh (Rasser, 2009).

Another future research direction could be to determine mean water level over marshes. The mathematical model of part of marsh's restoration plan was developed by research group led

by Drs. Montagna and Sadovski, which need precise local geoid as well. For example, in the mathematical system of equations developed by Dr. Sadovski for the system of N different plant species (Equation 7.1), the maximum possible density $L_i(x, y)$ (carrying capacity of the i -th species at point (x, y)) depends on salinity at a point, and salinity depends on the mean water levels. Therefore, it is important to have precise local geoid because of a need of exact depths (water levels) in the vegetation models. In future research, water levels data will be provided by Texas Coastal Ocean Observation Network (TCOON) of the Conrad Blucher Institute for Surveying and Science (CBI) at Texas A&M University—Corpus Christi (TAMUCC).

$$\frac{\partial u_i(x,y,t)}{\partial t} = r_i u_i \left(1 - \sum_{k=1}^N \frac{u_k}{L_k(x,y)}\right) + \varepsilon_i \nabla^2 \frac{u_i}{L_i(x,y)} \quad (7.1)$$

where $u_i(x, y, t)$ is the density of the i -th species at (x,y) at time t ; r_i is the rate of reproduction; $L_i(x, y)$ is the maximum possible density (carrying capacity of the i -th species at the point (x, y)); ε_i is the diffusion (or dispersion) coefficient of i -th species; N is the maximum number of different plant species.

Improve quality of modeling marsh restoration to make multi-species spatial-temporal models more exact. To satisfy this need requires using precise geoid as a basis. In future research, the goal is to determine mean water levels over marshes associated with precise local geoid.

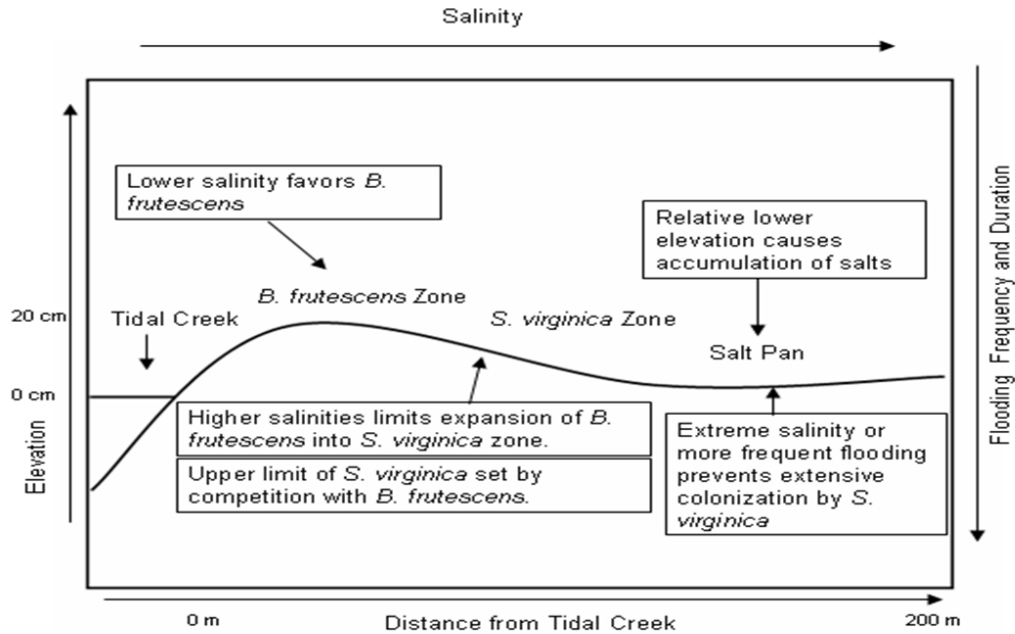


Figure 7.12 A conceptual model. Vegetation pattern for *Borrichia frutescens* and *Salicornia virginica* in the Nueces delta (Rasser, 2009).

7.6 Acknowledgements

Nueces Delta Elevation Control (NDEC) data was forwarded email by Dr. Paul Montagna and Dr. Alexey Sadovski on October 16, 2012. The Nueces river delta digital elevation model (DEM) (06_geoid Corrected_MERGE_minus_g99UTM_gdal) file was shared by Dr. Scott King. This DEM file was original published by Bureau of Economic Geology, University of Texas at Austin on February 29, 2008. The Nueces river delta DEM metadata was provided by Dr. James C. Gibeaut on March 22, 2013. Nyambura G. Njagi shared the Nueces County data.

7.7 References

Barras, J. A. , Beville, S., Britsch, D., Hartley, S., Hawes, S., Johnston, J., Kemp, P., Kinler, Q., Martucci, A., Porthouse, J., Reed, D., Roy, K., Sapkota, S., & Suhayda, J. (2003).

Historical and projected coastal Louisiana land changes: 1978–2050: U.S. Geological Survey Open-File Report 2003-334.

Barras, J. A., Bernier, J. C., & Morton, R. A. (2008). *Land area changes in coastal Louisiana—A multi decadal perspective (from 1956 to 2006)*. US Department of the Interior, US Geological Survey.

EPA. *Coastal wetland reviews: Highlights*. Available from:

http://water.epa.gov/type/wetlands/upload/CWR_Highlights-updated.pdf.

Hofmann-Wellenhof, B., & Moritz, H. (2006). *Physical geodesy* (2nd ed.). New York: Springer Wien.

Mitsch, W. J., & Gosselink, J. G. (2007). *Wetlands* (4th ed.). Hoboken, NJ: John Wiley & Sons, Inc.

National Oceanic and Atmospheric Administration and U. S. Department of Commerce. (2010). *NOAA's oil spill response. Shorelines and coastal habitats in the Gulf of Mexico*. Available from: <http://response.restoration.noaa.gov/deepwaterhorizon>.

NOAA Coastal Services Center and The Nature Conservancy. (2011). *Marshes on the move: A manager's guide to understanding and using model results depicting potential impacts of sea level rise on coastal wetlands*.

NOAA's state of the coast. (2011). *The Gulf of Mexico at a glance: a second glance*. Explore coastal communities, economy, and ecosystems.

Rasser, M.K. (2009). *The role of biotic and abiotic processes in the zonation of salt marsh plants in the Nueces River Delta, Texas*. Ph.D. dissertation, University of Texas.

Stedman, S. M., & Dahl, T. E. (2008). *Status and trends of wetlands in the coastal watersheds of the eastern United States, 1998 to 2004*. National Oceanic and Atmospheric Administration, National Marine Fisheries Service.

United States Environmental Protection Agency (EPA). *Coastal Wetlands website*. Available from: <http://water.epa.gov/type/wetlands/cwt.cfm>.

Wade, T., & Sommer, S. (Eds.) (2006). *A to Z GIS: An illustrated dictionary of geographic information systems* (2nd ed.). Redlands, California: ESRI Press.

Chapter 8: Conclusions

The Gulf of Mexico as 9th largest water body in the world is important for many reasons as introduced in Chapter 1. Dynamic environmental and physical changes including coastal erosion, tropic storm surges, coastal subsidence, and global sea level rise, etc. impact on the coastal areas, and should be evident in changes to the geoid along the coast. The geoid is the equipotential gravity surface of the earth, which the best fits the global mean sea level. The geoid is not only been seen as the most natural shape of the Earth, but also it serves as the reference surface for most of the height system. The shape of the geoid has a significant effect on interdisciplinary research and applications in Earth related science.

Today, GPS can be used to determine very accurate position quickly and easily. GNSS can be used to determine the ellipsoid height within just a few centimeters of accuracy. However, surveyors and engineers require orthometric heights more than the ellipsoid heights. Therefore, there is a need for an accurate geoid model.

This dissertation work was aimed to evaluate the accuracy of the local coastal geoid. Chapter 1 is an introduction to this work. Chapters 2 and 3 are similar in methodology but results are based on different kinds of data. Research in Chapters 2 shows that more precise evaluations of errors in gravity anomalies can be achieved by using different models of kriging. Results from Chapters 2 and 3 show that ordinary kriging with the stable semivariogram model provide better predictions. Research results from Chapter 3 provide estimation of maximum possible errors in the calculation of the geoid undulation. Research has provided a theoretical model in Chapter 4 to estimate very small changes in gravimetric potential relative to the coast. Maximum possible error in the solution of Dirichlet problem is determined in Chapter 5. Maximum possible error

depends on the errors of boundary values and the precision of the boundary itself. Results of factor analysis from Chapter 6 show that the elevation of sea level relates to the geoid and ocean circulation. Research in Chapter 7 shows that the predicted continuous elevation map obtained through the ordinary stable kriging was sufficiently precise and fairly reliable. Chapter 7 is an exploratory chapter, and the ideas of this chapter will help the future research.

Appendix 1 Historical Review

There are a several publications that support the discussion in introduces the materials of this section. For instance, Ewing & Mitchell (1970) and Smith (1997)'s work is regarded as describing the history of geodesy. There are also a lot of good internet resources available online (i.e. http://www.ferris.edu/faculty/burtchr/sure452/notes/history_of_geodesy.pdf).

Several thousand years ago, scientists were already interested in the size and shape of the earth, the exact problem scientists of geometrical geodesy grapple with today. No records indicate the beginning of geodesy, but we know that any theories were based solely on experiential data. The early ideas of the shape of the Earth were, of course, quite limited. Ancients thought the Earth must be flat, otherwise everything would fall off. The theories that the Earth is cylindrical and spherical were raised later. Ancient philosophers observed the changeable length of shadows projected on the ground, and the way ships travelled across the sea in trying to determine the shape of the Earth. Aristotle (4th Century B.C.) posed that the earth must be sphere based on gravity. A more interesting and important principle was posed by Greek philosopher Eratosthenes (276-195 B.C), who is considered to be the "Father of Geodesy". Eratosthenes was the first person to measure the size of the Earth. His principle was that if we assume the Earth is a sphere, then its size can be found if two quantities are known. The first quantity is the distance s between two points (Alexandria on the north and Syene/Aswan on the south); the second one is the angle α between two points at the center of the earth. Thus, the circumference C is obtained by calculating:

$$C = 360^\circ \frac{s}{\alpha} \quad (\text{A1.1})$$

In Eratosthenes's work, he measured the length of shadow from a gnomon at noon in Alexandria at the summer solstice. He assumed that Syene is on the same meridian as Alexandria and lies exactly under the Tropic of Cancer. The sun's rays reached the bottom of a well (Figure A1.1). Eratosthenes used a camel in order to measure the distance between the two locations. He traveled 100 stadia per day, and this trip took about 50 days. The arithmetic is easy. The distance was 5,000 stadia, so the circumference of the earth is 250,000 stadia. There were three errors in Eratosthenes's work. The first was difficulty in converting distance units. Secondly, the sun could not be directly overhead at the time of measurement. Finally, Alexandria and Syene were not on the same meridian. Therefore, the estimated circumference was too large by about 16%.

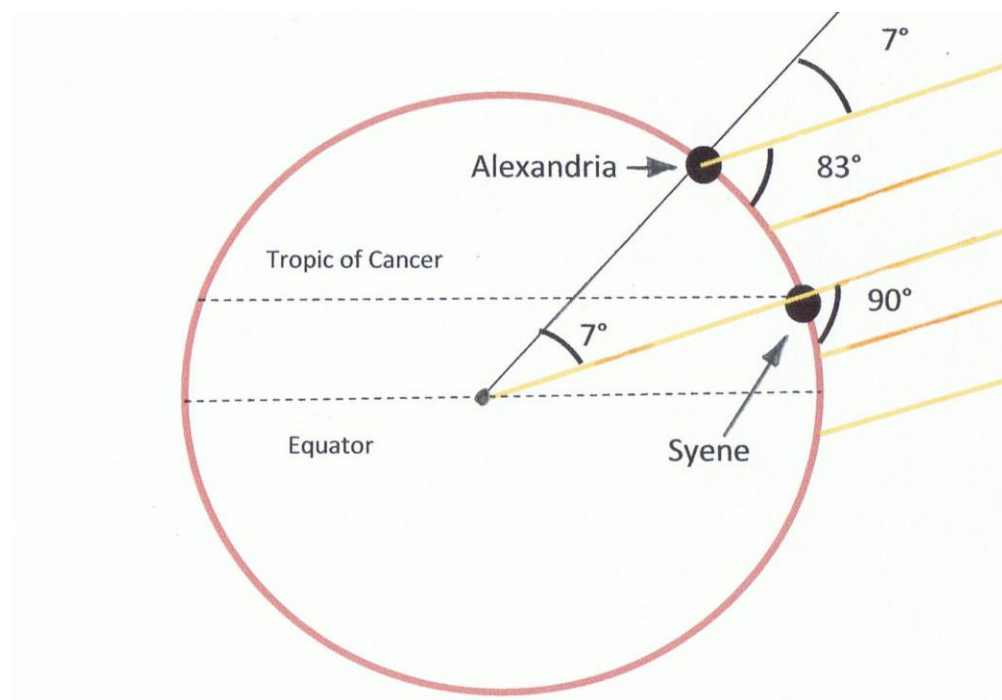


Figure A1.1 Eratosthenes' Experiment
(http://www.juliantrubin.com/bigten/images/eratosthenes_experiment.jpg).

The next similar geometry geodesy work was done by Poseidonius (135-50 B.C.), who used a different technique. Poseidonius measured the distance between Rhodes and Alexandria

by sailing. He used the star Canopus to determine the size of the earth. He found that Canopus was on the horizon at Rhodes, but elevated $\frac{1}{4}$ of zodiacal sign over Alexandria ($\frac{1}{48}$ of the circle). This measurement estimated the circumference of the earth was 240,000 stadia. This calculation resulted in a circumference that was 11% too large.

The caliph Abdullah al Mamun (A.D. 786-833) also did similar work, but used wooden rods to measure several distances around Baghdad and Al Raqqah. From a central starting point, al Mamun traveled both north and south until the vertical angle to the polar star changed by 1° . In this work, the conversion was still uncertain. The final circumference was approximately 39,986 km, which was 3.6% too large.

These three experiments used arc measurements to determine the size of the earth. Later, Gemma Frisius proposed the principle of triangulation in 1533. Willibrord Snellius (1580-1626), who was one of the first to use triangulation, measured 33 triangles along a practically north-south arc between Alkmaar and Bergen-op-Zoom in the Netherlands with $1'$ angular. This experiment's result was about 0.1% different from the current average.

In 1669, L'Abbé Jean Picard measured the meridional arc from Malvoisin, near Paris, to Sourdon, near Amiens, using the principle of triangulation. The work was continued north to Dunkerque and south to Collioure by Philippe de Lahire, and Dominique and Jaques Cassinis between 1683 and 1716. These experiments found out that there was a 1° meridional arc that decreased northward; the Earth was pointed at the poles (egg-shaped), which is called a prolate spheroid ($s_2 > s_1$). This was the first evidence that showed the Earth is not sphere. Isaac Newton's suggestions that the Earth was an oblate spheroid ($s_1 > s_2$) caused controversy. Newton suggested the earth should be flattened at the poles from his study of gravity. Newton showed

that liquid in rotation about an axis would flatten. Newton's work was purely theoretical, but Jean Richer's experience with a pendulum clock provided practical evidence. Richer experienced trouble adjusting his pendulum clock on his excursions to Cayenne, Guiana and to South America. The clock lost $2\frac{1}{2}$ minutes per day, and the pendulum had to be shortened. The period of clock depends on length of the pendulum and gravity's value (the farther from the center of gravity, the slower the clock is). There were also two scientific expeditions to determine the size of the Earth. One was in Peru led by Charles Marie de la Condamine in 1735; the other was led by Pierre L. M. de Maupertuis in Lapland in 1736. When comparing the results of both expeditions with a 1° meridional arc, the arc in Lapland was longer than the arc in Peru. This result proved that Newton's concept was correct—the shape of the earth is an oblate spheroid. This is referred to as the beginning of the Ellipsoid Era in geodesy.

Newton's theory classified the geodesy. The concept related to gravity, later this became known as physical geodesy. The geodetic work started more reasonable. In this era, not knowing precise longitude caused numerous shipwrecks, resulting in numerous deaths and loss of ships and goods. Shipwrecks were common because sailors did not know exactly where they were. Therefore, there was a need at that time to determine longitude. Galileo Galilei played a major role in determining longitude through his discovery of a "celestial timekeeper". By Galilei's observation using his telescope, he discovered that Jupiter had four satellites, and their passages in front and behind a plane could be predicted. Longitude could be obtained by calculating the time of these passages. But this work was still not possible at sea. John Harrison's work filled this gap. He developed a clock which could accurately keep time during ocean voyages and help determine the longitude. The first clock was completed in 1735. The fourth clock Harrison designed was smaller, and had an error rate of less than two minutes over a five -month voyage.

In the history of geodesy, Johann Carl Friedrich Gauss (1777-1855) played a pivotal role in the revolution of geodesy. As a mathematician, physicist and geodesist, Gauss developed the theory of least squares, theories in statistical estimations, and potential theory. He also was the first one to use least square theory to adjust a triangulation network. Fischer (1975) wrote down that Gauss (1828) wrote,

The arc measurement in Hannover adds new confirmation to the now unquestionable truth that the surface of the Earth does not have a quite regular shape.... While the astronomic observations give the latitude of Altona 51:52 smaller (than the geodetic, computed on the best fitting ellipsoid available), the observations made on the Brocken give its latitude 10-11" larger, a difference of which certainly only a fraction could be due to instruments and the declinations used in the computation. The comparison of the latitude difference between Altona and the Brocken with the curvature of the spheroid which best fits the Earth as a whole, would thus give a discrepancy of 16".

In our opinion it is incorrect to talk in such cases only of local deviations of the plumb line, thus considering them as isolated exceptions. What we call the surface of the Earth in a mathematical sense, is nothing else but that surface, which everywhere intersects the direction of gravity at right angles, and of which the surface of the oceans is a part. The direction of gravity at every point is determined by the shape of the rigid part of the Earth and its uneven density. On the upper surface of the Earth's crust, the only part of which we know anything at all, this shape and density appears as being very irregular; the irregularity of the density may easily extend quite far downward, and escapes our computations for which almost all data are lacking. The mathematical surface is produced by the total effect of these irregularly distributed elements. Instead of thinking it strange to find clear evidence of the irregularity, one should rather marvel that its effect is not even larger....

This does not prevent us, however, from considering the Earth as a whole as a spheroid of revolution, from which the real (mathematical) surface deviates everywhere in larger or smaller, shorter or longer undulations. Were it possible to quasi spin one trigonometric net all around the whole Earth and to compute thereby the relative position of all points, then the ideal spheroid of revolution would be the one where the computed directions of the normals best agreed with the astronomic observations [in today's language, where the deflections of the vertical are minimized]. Although this is an unattainable ideal, there is no doubt that future centuries will considerably advance the mathematical knowledge of the figure of the Earth.... Maybe the idea is not chimerical that some day all observatories of Europe will be trigonometrically connected

F. W. Bessel (1837) gave more details on difference between mathematical and physical surface of the Earth based on Gauss's explanation. Bessel wrote,

The visible irregularities of the physical surface of the Earth definitely do not belong to the mathematical surface, but, since they too are irregularities of the mass distribution, they do affect it indirectly by producing attractions which otherwise would not be there. Likewise, irregularities of the mass distribution in the Earth's interior produce irregularities of the mathematical surface. All attractions together, combined with the centrifugal force produce that surface, to which the geodetic work refers.... This is a surface which intersects at right angles the directions of the forces which consist of all attractions produced by the individual elements of the Earth, combined with the centrifugal force corresponding to its rotational velocity. This condition, however, only determines any of the surfaces which could be covered by a fluid in equilibrium; one must still decide which of these surfaces should be the mathematical surface of the Earth. The choice would, if not restricted by an extraneous condition, actually be arbitrary if the Earth were only a rigid body without an ocean. Since this, however, exists, it is appropriate to adopt that one as the surface of the Earth, of which the ocean surface is a part. Imagine the Earth covered by a net of channels connected with the ocean and filled by it, then the surface of the calm water in them would coincide with the mathematical surface of the Earth....

One must consider them (the irregularities) as distributed randomly over the Earth's surface, as small elevations above or small depressions below the surface of the - on the whole - best fitting ellipsoid of revolution. The extent of these undulations will not be known, unless made the specific purpose of a measurement.... I don't believe that it is of much interest to find that extent in a specific case, since this does not permit a general conclusion; yet I would follow with interest an investigation which ... (using already existing promising data)..., explores the behavior of these irregularities. Although one cannot expect to discover a pattern in the irregularities of the Earth's surface..., every new geodetic work connected with astronomic determinations will again point to their existence....

The reasonable shape of the Earth was clearly brought forward by Listing in 1872. He suggested that the shape of the Earth should be considered to be irregular, and must be thought of in relation to the ocean. Later, Listing's suggestion was taken by Helmert in 1884. He wrote,

That we gained some knowledge of the figure of the Earth in general although its surface is not everywhere accessible, was made possible through the existence of a - in the first approximation - very simple rule of formation for the shape of the Earth as a whole; a rule, whose factors are the gravitation of the mass elements and the centrifugal force produced through the rotation about an axis.

Especially important among the level surfaces is the surface of the oceans, which one must consider here as subject only to the gravity of the Earth and therefore calm, so that any movement due to the tides, winds, and other causes of ocean currents is disregarded. This ideal ocean surface forms the visible part of a level surface. One calls it the mathematical surface of the Earth or (with Listing, 1872) the geoid, in contrast to the real, the physical surface of the Earth. Through a system of channels leading from the ocean shore into the interior of the continents, one could visualize the geoid also there. The calm surface of ponds and lakes, however, are usually parts of other level surfaces.

The task of determining the shape of level surfaces is made easier by the fact that they have, in great approximation, the shape of an ellipsoid of revolution, slightly flattened at the poles. This made it possible to gain an approximate knowledge from measurements at a limited number of places....

Helmert coined the term Geoid, and defined the geoid as the shape of the Earth. He also raised the theory that related the geoid to potential—equipotential surface. Helmert suggested that the Earth’s surface should be thought of as the average corresponding to the mean sea level without winds, currents, tides, etc. However, Ferdinand Hassler is the first one actually started doing the geodetic survey on the coast in 1816. Bessel was wrong in the judgment of small geoidal undulations result from the distribution of irregularities, as the following development of geodesy.

Geodetic science entered into a great era when the first satellite (*Sputnik*) was launched on October 4th, 1957 and the United States launched the satellite (*Vanguard*) in 1958. This era is called the satellite geodesy era. Although Gauss proposed to minimize deflections of the vertical to find the best fitting world as the spheroid, as “an unattainable ideal” in geometric world net, attained later in satellite-derived world net.

References

Bessel, F.W. (1837). Über den einfluss der unregelmaessigkeiten der figure der erdw auf geodätische arbeiten und ihre vergleichung mit den astronomischen bestimmungen.

Astronomische Nachrichten, 14, 329-331.

Burtch, R. History of geodesy. Access on July 28, 2011. Available from:

http://www.ferris.edu/faculty/burtchr/sure452/notes/history_of_geodesy.pdf.

- Ewing, C. E., & Mitchell, M. M. (1970). *Introduction to geodesy*. New York: American Elsevier Publishing Company, Inc.
- Fischer, I. (1975). The figure of the Earth—changes in concepts. *Geophysical surveys*, 2(1), 3-54.
- Fischer, I., Another Look at Eratosthenes' and Posidonius' Determinations of the Earth's Circumference, Q.J1. R. Astr. Soc., 16, 152-167, 1975b.
- Gauss, C.F. (1828). Bestimmung des breitenunterschiedes zwischen den sternwarten von goettingen und altona durch beobachtungen am ramsdenschen zenithsector, Vanderschoeck und Ruprecht, Goettingen, 48-50.
- Heiskanen, W. A., & Moritz, H. (1967). *Physical geodesy*. San Francisco, London: Freeman. History of Geodesy. Access on July 28' 2011. Available from: <http://globalcogo.com/ge002.pdf>.
- Listing J. B. (1873). Über unsere jetzige Kenntniss der Gestalt und Grösse der Erde. Nachrichten von der Köning. Göttingen VLG der Dietrichschen Buchhandlung.
- Smith, J. R. (1997). *Introduction of geodesy: The history and concepts of modern geodesy*. New York, Chichester, Weinheim, Brisbane, Singapore, Toronto: John Wiley & Sons, Inc.
- Vaniček P., & Christou N. T. (Eds.) (1993). *Geoid and its geophysical interpretations*. Boca Raton, Ann Arbor, London, Tokyo: CRC Press.

Appendix 2 Theoretical Review

The geoid has been accepted as the “mathematical figure of the Earth” (Hofmann-Wellenhof and Moritz, 2006); as it ought to be, the ellipsoid then serves as the reference surface of the Earth. To study the geoid, it requires the description of the observed gravity field in terms of difference in gravity anomalies which indicate the intensity of gravity, deflections of the vertical (direction of gravity, which is the slope of the geoid), geoidal heights (also called geoidal undulation or geoidal separation) which reflect shape, and disturbing potential which is also called the anomalous potential (geopotential). All of these four parameters are interrelated (see Figure A2.1 and Figure A2.2).

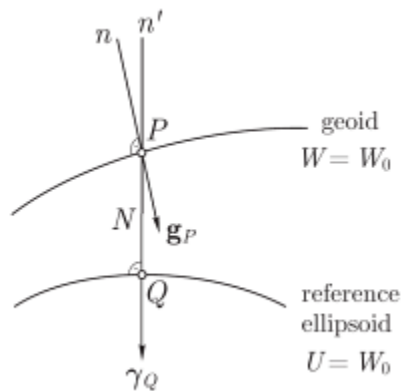


Figure A2.1 The Geoid and Reference Ellipsoid (Hofmann-Wellenhof and Moritz, 2006).

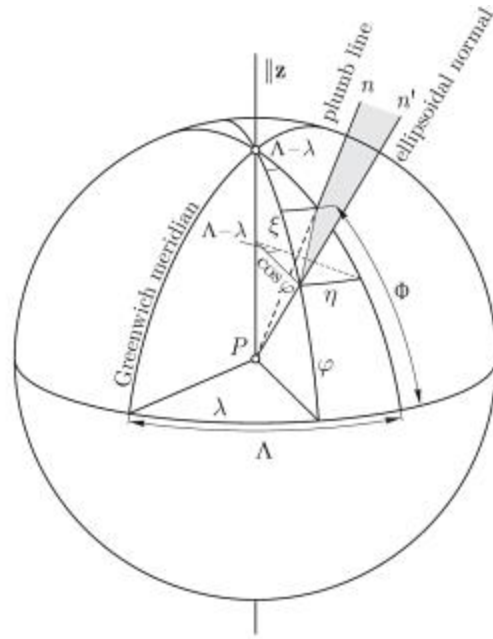


Figure A2.2 The Deflection of the Vertical (Hofmann-Wellenhof and Moritz, 2006).

The disturbing potential T is the small difference between the actual gravity potential W based on the geoid and the normal gravity potential U based on the reference ellipsoid surface:

$$T = W - U \quad (\text{A2.1})$$

The geoidal undulation N is the distance PQ (Figure A2.1) between the geoid and ellipsoid (see Equation A2.2).

$$N = h - H \quad (\text{A2.2})$$

In Equation A2.2, h is the ellipsoidal height that above the ellipsoid, and H is the orthometric height that above the geoid.

As illustrated in Figure A2.1, the gravity g at point P of the geoid and the normal gravity γ at point Q of the ellipsoid. The gravity anomaly (difference in magnitude) is computed:

$$\Delta g = g - \gamma \quad (\text{A2.3})$$

The deflection of the vertical is the difference in direction (also see Figure A2.2; a north-south component of the deflection of the vertical ζ and an east-west component η).

There is also a possibility that compare g and γ at the same point P of the geoid. Then the gravity disturbance is obtained by

$$\delta g = g - \gamma_p \quad (\text{A2.4})$$

The determination of the geoid produced a long line of theoretical studies. In 1849, a theorem by G.G. Stokes, well-known as Stokes Theorem, provided a way to compute the geoidal undulation at point P of the geoid from gravity anomalies. Equation A2.5 is called Stokes' formula or Stokes' integral (Figure A2.3).

$$N = C \iint_S F \Delta g dS \quad (\text{A2.5})$$

where S represents the geoid;

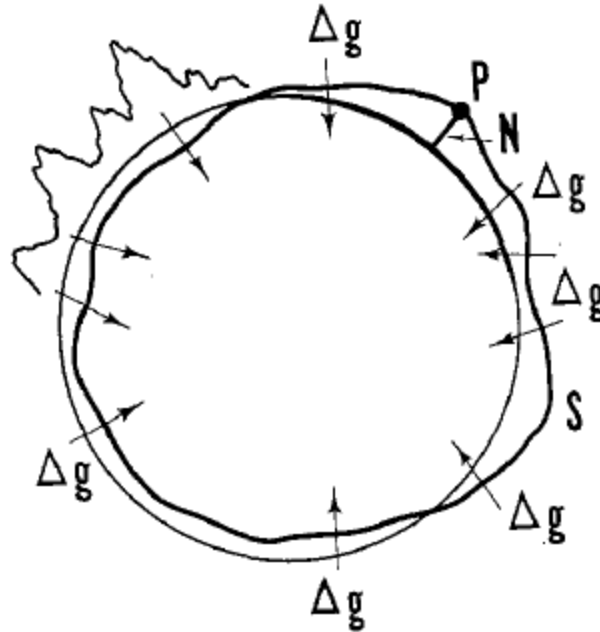


Figure A2.3 The Stokes Theorem (Fischer, 1975).

Using Stokes' formula to compute a global geoid from gravity anomalies were first made by R. A. Hirvonen in 1934; later in 1948 by L. Tanni, and then updated by Heiskanen in 1957 (Fischer, 1975). The reference ellipsoid used in these computations has a flattening of 1/297. In 1928, F. A. Vening Meinesz gave a derivative formula which computes deflections of the vertical, the geoid's slope, from the gravity anomalies as well.

The reduction of observed gravity from the physical surface of the observation is needed to refer to the geoid. Several techniques have been developed based on the different topographic masses above the sea level. Free-air reduction by a theoretical vertical gradient of gravity $\frac{\partial g}{\partial H}$, we have,

$$g_0 = g + F, \tag{A2.6}$$

where

$$F = -\frac{\partial g}{\partial H}H \quad (\text{A2.7})$$

F is the free-air reduction to the geoid; g is observed gravity; g_0 is the observed gravity refer to the geoid; H is the height between the physical surface of the observation and the corresponding location on the geoid. The assumption of this technique is no masses above the geoid. The Bouguer reduction is using a mean standard density value of the physical surface. In other words, it assumes that the masses outside the geoid should be completely removed in the Bouguer reduction. Terrain correction is simple, and this technique is for the effect of topographic variations in the close neighborhood.

When the compensation in masses was questioned, the reduction for such compensation was developed by J. H. Pratt in 1854. Isostatic reduction started with Pratt's calculations of the effect of the Himalayas on the plumb line at different stations (Hofmann-Wellenhof and Moritz, 2006). The topographic deflection of the vertical that affected by the attraction of the masses was much larger than the observed discrepancy between the geodetic and astronomic positions. The Pratt-Hayford theory of isostatic supposes that lighter compensating materials underneath the Himalayas. This theory balances the excess masses with the underground deficient masses in mathematical way, which was also followed by other theories, such as G. B. Airy theory, Airy-Heiskanen theory, Vening Meinesz theory, M. P. Rudzki, etc. (Fischer, 1975; Hofmann-Wellenhof and Moritz, 2006). They were applied to the deflection of the vertical as well as to gravity anomalies.

Physical geodesy has also developed along Helmert's theories. Unlike Stokes' theorem need various hypotheses (details can be founded in Heiskanen & Vening Meinesz, 1958), this direction required a minimum of hypotheses. With avoiding the assumption of mass transfers

when reduction is required to fit the condition of Stokes' theorem, a theorem by M. S. Molodensky in 1945 can directly work from observations on the topographic surface instead of the geoid. The surface by Molodensky's theorem is quasigeoid, which is plotted the height anomalies above the ellipsoid. According to Hofmann-Wellenhof and Moritz (2006), quasigeoid does not have a physical meaning and is not a level surface.

References

- Fischer, I. (1975). The figure of the Earth—changes in concepts. *Geophysical surveys*, 2(1), 3-54.
- Heiskanen, W. A., & Meinesz, F. V. (1958). *The earth and its gravity field*. New York: McGraw-Hill.
- Hofmann-Wellenhof, B., & Moritz, H. (2006). *Physical geodesy* (2nd ed.). New York: Springer Wien.

Appendix 3 Notes of Universal Kriging with Constant Trend Removed

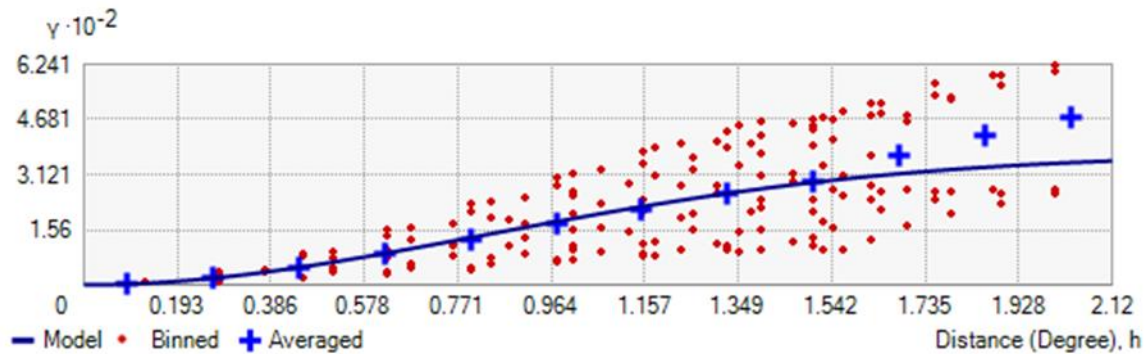


Figure A3.1 Semivariogram of the universal stable kriging with removal of constant trend. The averaged semivariogram values on the y-axis (in mgal^2), and distance (or lag) on the x-axis (in degree). Binned values are shown as red dots, which are sorted the relative values between points based on their distances and directions and computed a value by square of the difference between the original values of points; Average values are shown as blue crosses, which are generated by binning semivariogram points; The model is shown as blue curve, which is fitted to average values. Model: $0.24582 \times \text{Nugget} + 369.12 \times \text{Stable}(2.1204, 1.9385)$.

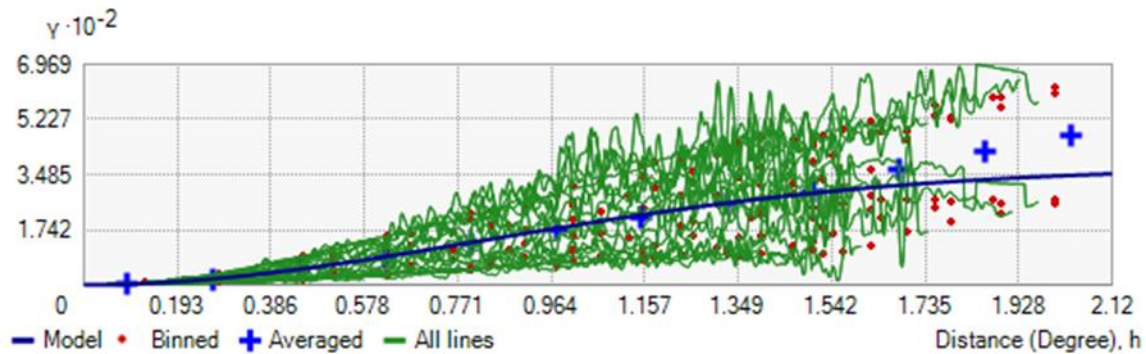


Figure A3.2 Semivariogram with all lines (green lines) which fit binned semivariogram values. The averaged semivariogram values on the y-axis (in mgal^2), and distance (or lag) on the x-axis (in degree).

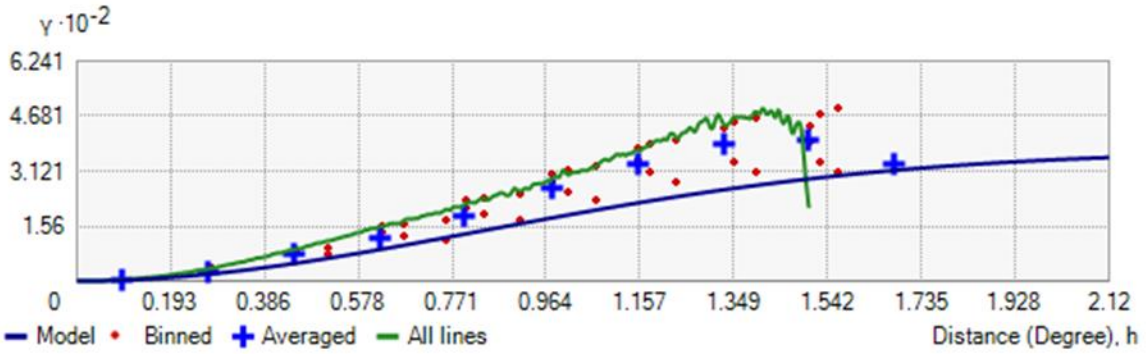


Figure A3.3 Semivariogram with showing search direction. The tolerance is 45 and the bandwidth (lags) is 3. The local polynomial shown as a green line fits the semivariogram surface in this case. The averaged semivariogram values on the y-axis (in mgal^2), and distance (or lag) on the x-axis (in degree).

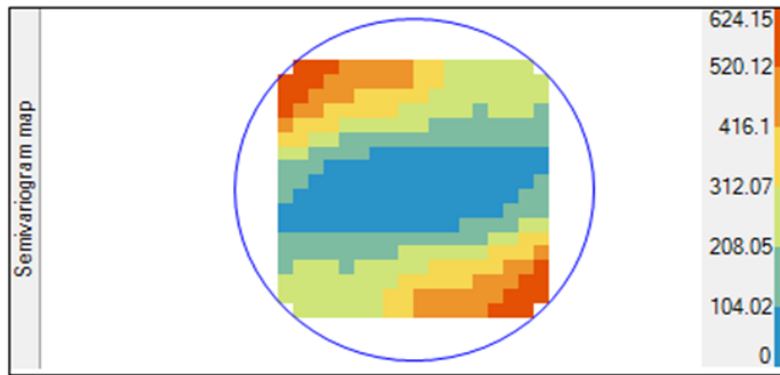


Figure A3.4 A semivariogram map. The color band shows semivariogram values with weights (unit in mgal^2).

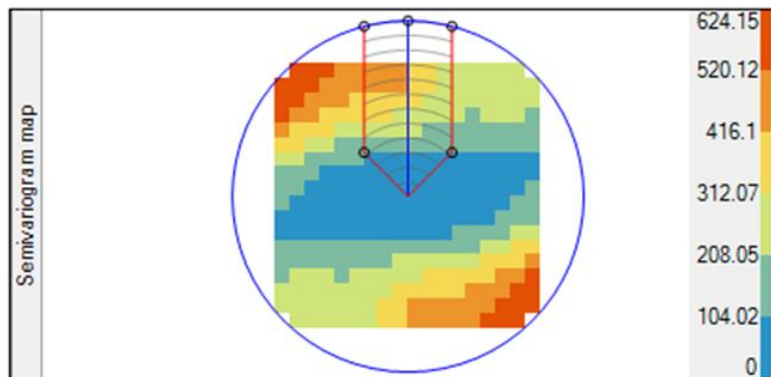


Figure A3.5 A semivariogram map with an example search direction transect (unit in mgal^2).

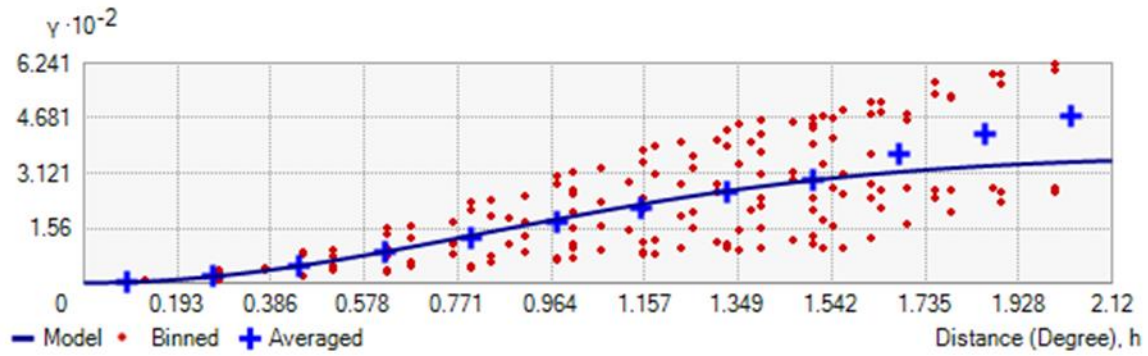


Figure A3.6 Semivariogram of the universal Gaussian kriging with removal of constant trend. The averaged semivariogram values on the y-axis (in mgal^2), and distance (or lag) on the x-axis (in degree). Binned values are shown as red dots, which are sorted the relative values between points based on their distances and directions and computed a value by square of the difference between the original values of points; Average values are shown as blue crosses, which are generated by binning semivariogram points; The model is shown as blue curve, which is fitted to average values. Model: $0.75508 \cdot \text{Nugget} + 360.22 \cdot \text{Gaussian}(2.0244)$.

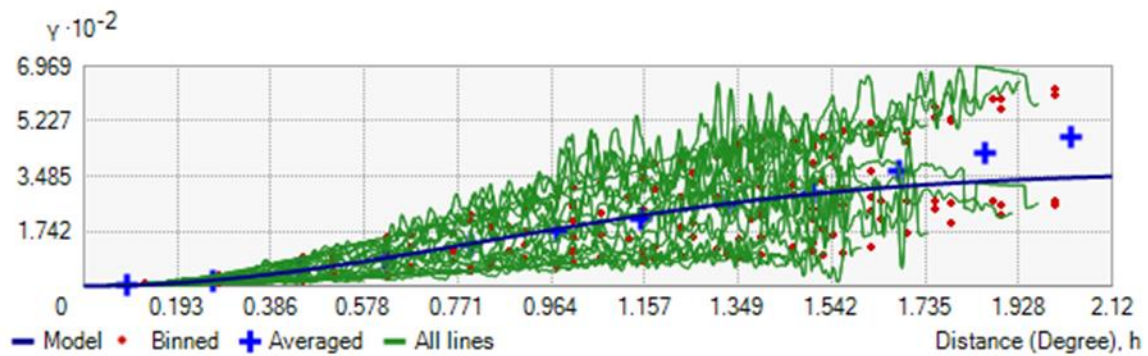


Figure A3.7 Semivariogram with all lines (green lines) which fit binned semivariogram values. The averaged semivariogram values on the y-axis (in mgal^2), and distance (or lag) on the x-axis (in degree).

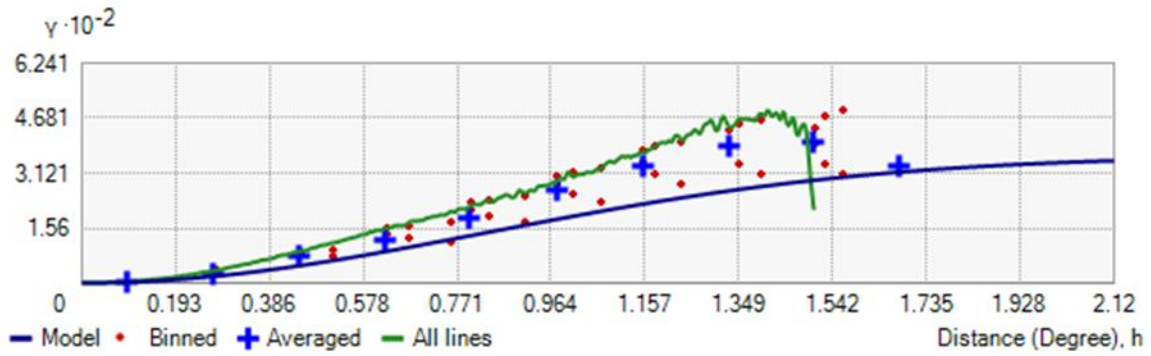


Figure A3.8 Semivariogram with showing search direction. The tolerance is 45 and the bandwidth (lags) is 3. The local polynomial shown as a green line fits the semivariogram surface in this case. The averaged semivariogram values on the y-axis (in mgal^2), and distance (or lag) on the x-axis (in degree).

Cross-validation statistics	Prediction Model 1	Prediction Model 2	Prediction Model 3	Prediction Model 4	Prediction Model 5	Prediction Model 6
	O.K.-Stable	O.K.-Gaussian	U.K.-Stable	U.K.-Gaussian	U.K. 1st-Stable	U.K. 1st-Gaussian
RMS Standardized	0.2556	0.3275	0.2556	0.3275	0.2058	0.2214
Mean Standardized	-0.0006	-0.0067	-0.0006	-0.0067	-0.0025	-0.0061
Average Standard Error (ASE)	0.5187	0.9003	0.5187	0.9003	0.5070	0.6426
Root Mean Square (RMS)	0.1309	0.2935	0.1309	0.2935	0.1028	0.1412
Difference between RMS and ASE	0.3878	0.6068	0.3878	0.6068	0.4042	0.5014
Difference in Percentage	74.76%	67.40%	74.76%	67.40%	79.72%	78.03%

Table A3.1 Cross validation statistics compared between the stable and the Gaussian techniques.

Appendix 4 How to Read Semivariogram in ArcGIS 10 and 10.1

The exact values on y-axis of the semivariogram shown in Chapter 2, for example,

Figure 2.7 are vague to read. The way to read this value is using the formula:

$$y = Y(10^{-2}).$$

However, the scientific notation often writes as $Y = y(10^2)$. Therefore, the partial sill of the semivariogram in Figure 2.7 is 3.691191×10^2 (369.1191).

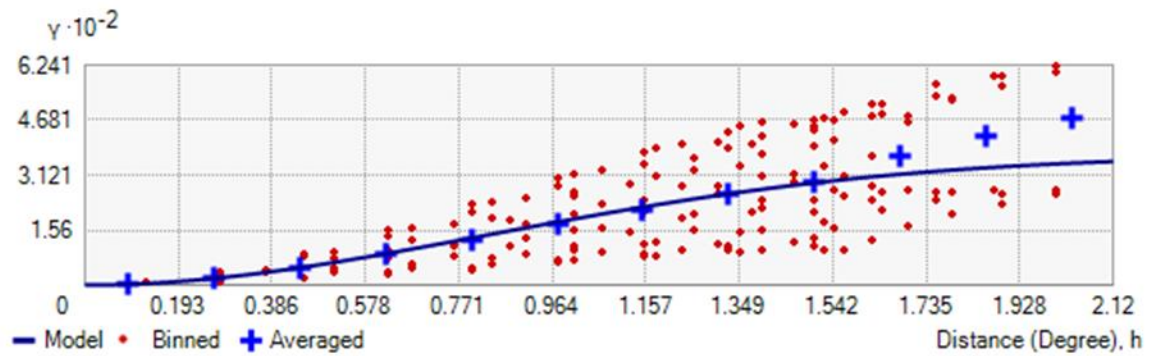


Figure 2.7 in Chapter 2.